



THÈSE / UNIVERSITÉ DE RENNES 1

sous le sceau de l'Université Bretagne Loire

pour le grade de

DOCTEUR DE L'UNIVERSITÉ DE RENNES 1

Mention : Sciences de Matériaux

Ecole doctorale Science de la Matière

présentée par

Yimin Wu

Préparée dans l'équipe Verres & Céramiques
UMR CNRS 6226 Institut de Sciences Chimiques de Rennes
UFR Sciences et Propriétés de la Matière

**Céramiques
semiconductrices à
base de séléniures
pour des applications
photovoltaïque et
thermoélectrique**

Thèse soutenue

le 16 Décembre 2016

devant le jury composé de :

Sylvie Hebert

Directrice de recherche CNRS, Université de Caen /
rapporteur

Marcel PASQUINELLI

Professeur, Université d'Aix-Marseille / *rapporteur*

Jean Luc Adam

Directeur de recherche CNRS, Université de Rennes
1/*examineur*

Xianghua ZHANG

Directeur de Recherche CNRS, Université de
Rennes 1 / *directeur de thèse*

XianPing Fan

Professeur, Zhejiang University / *co-directeur de
thèse*

Michel Cathelinaud

Ingénieur de recherche CNRS, Université de
Rennes 1/*examineur*

Acknowledgement

Acknowledgement

The research works presented here are accomplished in the Laboratoire de Verres et Céramiques of Université de Rennes 1.

Firstly, I would like to express my gratitude to my PhD supervisor Mr. Xianghua Zhang for his patience and knowledgeability that directed me in the field of glass ceramics through the research experience. The sincere thanks are also given to my co-supervisor, Mr. Xianping Fan, for directing me in the field of nanocrystals synthesizing and recommending me to Université de Rennes 1.

I would like to thank the members of jury for agreeing to judge the thesis. I wish to express my sincere thanks to Ms. Sylvie Hebert of Université de Caen and Mr. Marcel Pasquinelli of Université de Aix-Marseille for their acceptance to be the reporters of my thesis. Meanwhile, I want to thank Mr. Jean Luc Adam of Université de Rennes 1, Mr. Michel Cathelinaud of Université de Rennes 1 and Mr. Xianping Fan of Zhejiang University for participating in my PhD defense as an invite member.

I would like to give my sincere thanks to Mr. Ilia Korolkov for his kindness and for the valuable discussion and cooperation in preparation and properties characterization of ceramics. My thanks are addressed particularly to Mr. Zhang and Mr. Xianping Fan, for their wise advices, their imagination, as well as their encouragement throughout this work. I wish to thank all the people who helped me in completion of the project. Thanks will give to Ms. Adele Renaud for explaining a foundational principle for photoelectric properties of my research. I thank Mr. Vincent Dorcet for his help in HRTEM. I would give my thanks to Mr. Xusheng Qiao for his valuable advices in my work. My gratitude also goes to Ms. Hongli Ma for her helps both for my work and life.

I wish to thank all my colleagues in the laboratory. As a foreigner in the lab, they are so friendly to me and they help me to be familiar with glass preparation and other lab equipments in no time. Gratitude is also given to Didier, Thierry J. and Thierry P. for their help of the experimental equipments.

My Chinese fellows, Shuo Cui, Minjia Wang, Yanghai Xu, Yiming Wu and Guangxing Liang, also gave me a lot of help and made my life in France colorful.

Acknowledgement

*I would like to thank especially my fiancée Ziqian Chai, for her company and encouragement.
My final thanks are addressed to my family, who never doubted me and always supported me.*

Table of contents

Résumé détaillé en français	i
General introduction.....	1
Chapter I: Solar energy conversion.....	5
1.1 Introduction	- 6 -
1.2 Solar energy.....	- 10 -
1.2.1 Solar energy conversion	- 11 -
1.2.1.1 Photothermal conversion.....	- 11 -
1.2.1.1.1 Tracking Systems	- 14 -
1.2.1.1.2 Thermal Energy Storage (TES).....	- 15 -
1.2.2 Photochemical conversion.....	- 15 -
1.2.2.1 Electrochemical water splitting	- 17 -
1.2.2.2 Environmental remediation	- 20 -
1.2.3 Photovoltaic conversion	- 21 -
1.2.3.1 P-N junction: working principle of semiconductor based solar cell	- 23 -
1.2.3.2 Efficiency limits	- 25 -
1.2.3.3 Classification and development of solar cells	- 27 -
1.3 Thermoelectric (TE) conversion	- 30 -
1.3.1 Basic thermoelectric principle.....	- 32 -
1.3.1.1 Thermoelectric effect	- 32 -
1.3.1.1.1 Seebeck effect	- 32 -
1.3.1.1.2 Peltier effect	- 33 -
1.3.1.1.3 Thomson effect.....	- 35 -
1.3.1.1.4 Kelvin relations	- 35 -
1.3.2 Thermoelectric converters.....	- 36 -
1.3.3 Material selection criteria.....	- 38 -
1.3.3.1 Power factor	- 38 -
1.3.3.2 Figure of merit.....	- 39 -

Table of contents

1.4 Conclusions	- 40 -
1.5 References	- 41 -
Chapter II: Structure and photoelectric properties of $\text{Cu}_2\text{GeSe}_3\text{-Sb}_2\text{Se}_3$ ceramics	50
2.1 Introduction	- 51 -
2.2 Experimental procedure	- 52 -
2.2.1 Preparation of $\text{Cu}_2\text{GeSe}_3\text{-Sb}_2\text{Se}_3$ ceramics.....	- 52 -
2.2.2 Presentation of characterization techniques	- 54 -
2.2.2.2 X-ray diffraction (XRD) analysis.....	- 54 -
2.2.2.3 Scanning electron microscope (SEM) images and Energy Dispersive Spectrometer (EDS) elemental mappings	- 54 -
2.2.2.4 Photo-electro-chemical (PEC) measurement	- 56 -
2.2.2.5 Electrical conductivity measurement	- 62 -
2.2.2.6 The conductivity type measurement.....	- 63 -
2.3 Results and discussion.....	- 64 -
2.3.1 Structure and photoelectric properties of the $x\text{Cu}_2\text{GeSe}_3\text{-(100-x)}\text{Sb}_2\text{Se}_3$ ($x=10,20\dots,70$) ceramics.....	- 64 -
2.3.2 Structure and photoelectric properties of $50(x\text{Cu}+(1-x)\text{CuI})_2\text{GeSe}_3\text{-50Sb}_2\text{Se}_3$ ceramics.....	- 70 -
2.4 Conclusions	- 74 -
2.5 References	- 75 -
Chapter III: Study of semiconducting ceramics in the $\text{Cu}_3\text{SbSe}_4\text{-Sb}_2\text{Se}_3$ system.....	79
3.1 Introduction	- 79 -
3.2 Experimental Procedure	- 80 -
3.2.1 Preparation of $\text{Cu}_3\text{SbSe}_4\text{-Sb}_2\text{Se}_3$ ceramics	- 80 -
3.2.2 Presentation of characterization techniques	- 80 -
3.3 Results and discussion.....	- 81 -
3.3.1 Structure and photoelectric properties of $x(0.9\text{Cu}+0.1\text{CuI})_3\text{SbSe}_4\text{-(100-x)}\text{Sb}_2\text{Se}_3$ ceramics ($x=30, 40\dots, 70$)	- 81 -

Table of contents

3.3.2 Structure and photoelectric properties of the 40Cu ₃ SbSe ₄ -60Sb ₂ Se ₃ ceramics . -	88 -
3.3.3 Preparation and properties of 40[(Cu, CuI) ₃ (Sb, Sn)Se ₄]-60Sb ₂ Se ₃ ceramics ... -	92 -
3.4 Conclusions	94 -
3.5 References	95 -
Chapter IV: Synthesis of CuSe nanoparticles and single-crystalline two-dimensional nanoplatelets	99
4.1 Introduction	99 -
4.2 Experimental procedure	100 -
4.2.1 Synthesis of the Cu _x Se nanocrystals	100 -
4.2.2 Presentation of the characterization techniques	104 -
4.3 Results and discussion.....	105 -
4.3.1 Influence of reaction temperature on Cu _x Se nanocrystals	105 -
4.3.2 Copper selenides nanocrystals synthesized with the presence of Al(NO ₃) ₃ 9H ₂ O	106 -
4.3.3 Growth mechanism of CuSe single-crystalline two-dimensional nanoplatelets -	113 -
4.3.4 Other binary selenides synthesized by hot-injection.....	114 -
4.4 Conclusions	116 -
4.5 References	117 -
Chapter V: Monodisperse Cu₃SbSe₄ nanoparticles and related ceramics for thermoelectric applications	123
5.1 Introduction	123 -
5.2 Experimental procedure	124 -
5.2.1 Sample preparation.....	124 -
5.2.2 Presentation of characterization techniques	125 -
5.3 Results and discussion.....	126 -
5.4 Conclusions	138 -

Table of contents

5.5 References	- 138 -
Chapter VI: General conclusions and perspectives	143
Abstract	- 147 -
RESUME.....	- 148 -

Résumé détaillé en français

Introduction

L'accélération du développement économique mondiale et l'amélioration du niveau de vie de la population accroissent considérablement et constamment la demande énergétique. Cette demande est aujourd'hui satisfaite en grande partie par des énergies fossiles non renouvelables qui sont principalement du pétrole, du charbon et du gaz naturel. L'épuisement de ces ressources naturelles est certain à plus ou moins longue échéance. L'un des grands défis en face de l'humanité pour un développement durable est de trouver des sources d'énergie renouvelables.

Parmi les ressources renouvelables, l'énergie solaire présente, de loin, le plus grand potentiel par rapport à d'autres sources (hydraulique, vent, marée...). En effet, l'énergie solaire qui inonde la Terre chaque année correspond approximativement à 10.000 ans de consommation mondiale au rythme actuel.

L'énergie solaire est déjà largement exploitée directement ou indirectement par l'humanité avec plus ou moins d'efficacité. Sa conversion en énergie électrique a reçu une attention particulière ces dernières années dans le monde entier avec une grande capacité d'installation et toujours en forte croissance. Ceci est lié à l'utilité universelle de l'électricité et à la facilité de transport de cette énergie. Les nombreux systèmes photovoltaïques déjà installés produisent de l'électricité qui n'est pas encore économiquement compétitive par rapport à celle produite avec des combustibles fossiles. En plus, certains systèmes utilisent des éléments rares ou des éléments toxiques.

La recherche sur des matériaux efficaces pour la conversion de l'énergie solaire est toujours l'un des sujets les plus porteurs de la communauté scientifique. L'avancée la plus spectaculaire dans ce domaine pendant ces dernières années, est sans aucun doute les cellules solaires à base de Pérovskite qui atteignent déjà un rendement supérieur à 20% avec une technologie de fabrication potentiellement très faible. La durabilité chimique et la teneur en plomb sont parmi les problèmes à résoudre avant une commercialisation réelle.

La conversion de l'énergie thermique en électricité, par effet thermoélectrique, est étudiée depuis de nombreuses années. Les applications réelles restent encore marginales malgré

l'intérêt de cette technologie. La clé est de développer des matériaux avec un grand facteur de mérite.

Dans ce travail de thèse, nous proposons d'étudier des céramiques semiconductrices avec une microstructure unique contenant des hétérojonctions auto organisées qui facilite grandement la séparation des charges photo générées. Ce type de matériaux sont très intéressants comme matériaux photovoltaïques ou thermoélectriques.

Synthèse, structure et propriétés photoélectriques des céramiques dans le système $\text{Cu}_2\text{GeSe}_3\text{-Sb}_2\text{Se}_3$

Notre laboratoire est spécialisé dans la recherche et le développement de verres pour la transmission infrarouge. Des halogénures d'alcalin ont été introduits dans les verres afin d'induire une cristallisation contrôlable pour obtenir des vitrocéramiques transparentes avec des propriétés mécaniques nettement améliorées par rapport aux verres. L'étude antérieure réalisée au laboratoire a démontré qu'un verre dans le système $\text{GeSe}_2\text{-Sb}_2\text{Se}_3\text{-CuI}$ permet de créer une microstructure à hétérojonctions formées par Sb_2Se_3 et Cu_2GeSe_3 en contrôlant la cristallisation du verre de chalcogénure. Cette structure unique est à l'origine des propriétés photoélectriques prometteuses, avec une forte absorption du spectre solaire, une génération et une séparation efficaces des porteurs de charge.

Dans les vitrocéramiques décrites ci-dessus, les phases actives sont Sb_2Se_3 (dopé par l'iode) et Cu_2GeSe_3 avec une phase résiduelle vitreuse sans fonction identifiée, mais contenant une grande partie du germanium qui est l'élément le plus coûteux. Ainsi, nous avons décidé d'étudier directement le système Sb_2Se_3 et Cu_2GeSe_3 avec différentes teneurs en iode. Les céramiques ont été synthétisées en utilisant du Ge, Sb, Se, Cu ou/et CuI comme produits de départ avec la technique de tube de silice scellé sous vide.

En absence d'iode, des céramiques contenant les phases Sb_2Se_3 et Cu_2GeSe_3 ont été synthétisées. La proportion de chaque phase dépend directement de la composition de départ. L'étude de la microstructure en relation avec les propriétés photoélectriques a conduit aux remarques/conclusions suivantes :

- La phase conductrice Cu_2GeSe_3 est interconnectée, formant ainsi un réseau conducteur.

- Les mesures photo-électro-chimiques montrent que la céramique se comporte comme un semi-conducteur du type P, comme Cu_2GeSe_3 , avec cependant un photocourant nettement supérieur à celui généré avec une phase pure de Cu_2GeSe_3 . La phase Sb_2Se_3 , un semi-conducteur de type n avec une mauvaise conductivité électrique ne participe pas à la conduction de porteurs de charge. Il est vraisemblable que les hétérojonctions formées par ces deux phases facilitent sensiblement la séparation de charges photo-générées, donnant ainsi un photo-courant important.

L'addition de l'iode dans le système $\text{GeSe}_2\text{-Sb}_2\text{Se}_3$ change de façon très importante la microstructure et les propriétés photo-électro-chimiques des céramiques semi-conductrices. Les résultats sont résumés dans la Figure 1.

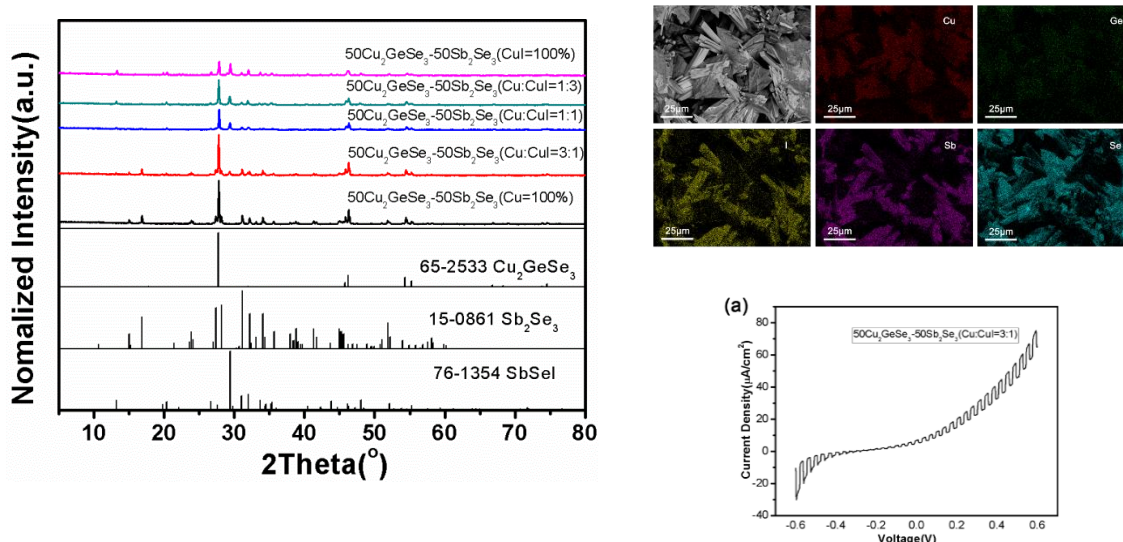


Figure 1. Phases cristallisées, les propriétés photo-électro-chimiques et la microstructure des céramiques dans le système $\text{GeSe}_2\text{-Sb}_2\text{Se}_3$ avec le Cu progressivement substitué par le CuI.

Contrairement à ce qui est produit dans les vitrocéramiques du système Ge-Sb-Se-CuI , l'iode n'est pas inséré ici dans les cristaux de Sb_2Se_3 , puisqu'aucun déplacement de pics de diffraction attribués à Sb_2Se_3 n'est observé. L'introduction de l'iode provoque immédiatement la cristallisation d'une nouvelle phase, le SbSeI , beaucoup plus conductrice que le Sb_2Se_3 . L'observation de la microstructure avec l'analyse de la composition montrent que la phase conductrice Cu_2GeSe_3 est maintenant interrompue par le Sb_2Se_3 ou/et le SbSeI . Le chemin conducteur passe donc obligatoirement par les deux phases, Cu_2GeSe_3 du type p et SbSeI du

type n, le Sb_2Se_3 pur n'ayant pas suffisamment de conductivité. L'ensemble de la céramique se comporte donc simultanément comme un semi-conducteur p et n, comme le montrent les mesures photo-électro-chimiques (Figure 1). Les études précédentes ont montré que ce type de structure est très favorable à la séparation et au transport de charges photo-générées, pouvant conduire à une durée de vie exceptionnellement longues pour les charges minoritaires.

Etude du système $\text{Cu}_3\text{SbSe}_4\text{-Sb}_2\text{Se}_3$

Pour l'application photovoltaïque, l'application visée pour les matériaux étudiés ci-dessus, il est important que ces matériaux ne contiennent pas d'élément rare, ce qui est un peu le cas du germanium contenu dans le système $\text{GeSe}_2\text{-Sb}_2\text{Se}_3$, même si le meilleur matériau n'en contient que 9% molaire. C'est un argument supplémentaire si cet élément peut être supprimé. Par conséquent et par analogie, des céramiques dans le système $\text{Cu}_3\text{SbSe}_4\text{-Sb}_2\text{Se}_3$ ont été étudiées. Le Cu_3SbSe_4 a été beaucoup étudié pour des applications thermoélectriques et il a une conductivité électrique similaire et légèrement plus élevée que le Cu_2GeSe_3 .

Les résultats les plus significatifs obtenus avec ce système sont les suivants :

- Des jonctions formées par le Sb_2Se_3 et le Cu_2GeSe_3 ont été observées par le microscope électronique en transmission (Figure 2).
- L'introduction de l'iode dans ce système ne donne pas de phase supplémentaire, comme c'était le cas du système $\text{Cu}_2\text{GeSe}_3\text{-Sb}_2\text{Se}_3$ avec la formation d'une nouvelle phase SbSeI beaucoup plus conductrice électriquement que le Sb_2Se_3 .
- Des mesures photo-électro-chimiques avec ces céramiques montrent un comportement de semi-conducteur de type p et n simultanément, comme avec le système contenant du germanium. Cependant, le photocourant avec un bias positif est nettement plus faible qu'avec un bias négatif, indiquant que ce sont des semi-conducteurs très

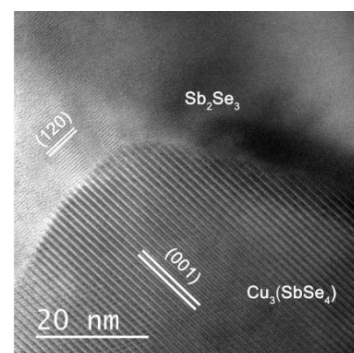


Figure 2. Microstructure des céramiques $\text{Cu}_3\text{SbSe}_4\text{-Sb}_2\text{Se}_3$ contenant de l'iode

faiblement n. Ceci est probablement lié à l'absence de la phase semi-conductrice du type n qui est le SbSeI.

Synthèse de monocristaux bidimensionnels de CuSe

Un système photovoltaïque idéal nécessite des matériaux semi-conducteurs avec un band gap et un niveau de fermi compatible et si possible ajustable. Le CuSe est un séléniure longtemps considéré pour des applications photovoltaïques avec une structure électronique proches de celle des séléniures étudiés précédemment. Nous avons donc développé une procédure rapide permettant d'obtenir des monocristaux bidimensionnels de CuSe de haute qualité

Les nanocristaux de Cu_xSe ont été produits avec une approche par injection rapide en faisant réagir $\text{CuCl}_2 \cdot 2\text{H}_2\text{O}$ et $\text{Al}(\text{NO}_3)_3 \cdot 9\text{H}_2\text{O}$ avec un excès de sélénium en présence d'hexadécylamine (HDA)

La morphologie des nanoparticules ou des microplaques, obtenus avec différents temps de réaction à 180°C est illustrée sur la Figure 3. On peut remarquer, sur ces images de la microscopie électronique en transmission, la grande uniformité des nanoparticules. Une prolongation du temps de réaction conduit à une croissance homogène et régulière de cristaux jusqu'à l'obtention de plaques monocristallins. Il semble que ces nanocristaux s'orientent spontanément pour assurer une croissance monocristalline. Les défauts dans les cristaux devraient donc être minimisés, ce qui est évidemment favorable pour obtenir de bonnes propriétés photoélectriques.

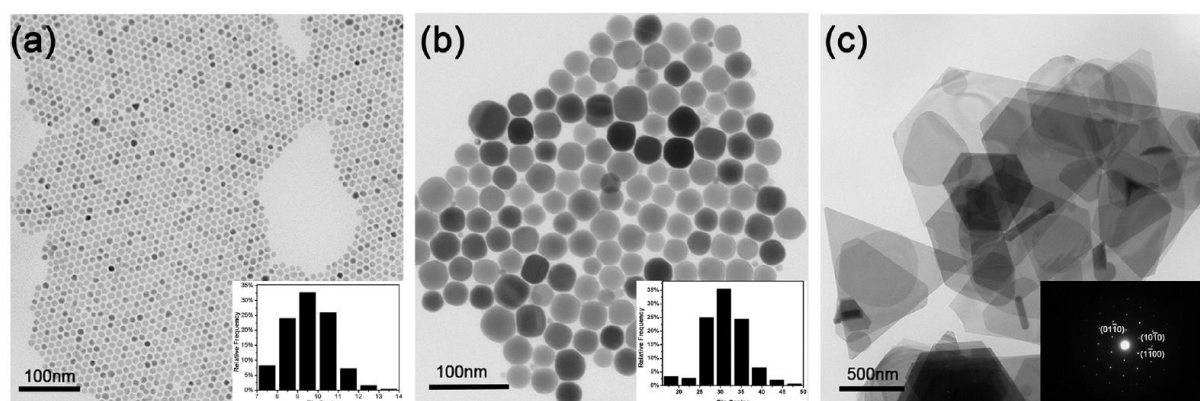


Figure 3. Morphologie des CuSe obtenue en fonction du temps de réaction à 180°C : 0 min, 10 min et 60 min.

L'absorption de ces nanoparticules ou plaques est mesurée en mesurant la réflexion diffuse. Le Cu_xSe est un semi-conducteur de type p avec un band gap direct. Les nanoparticules synthétisées avec un temps de réaction de 0 et 10 minutes présentent un band gap assez comparable situé vers 1.25 eV (Figure 4). Avec une prolongation de temps de réaction en présence d'un excès de sélénium, un déficit en Cu ou un excès en sélénium est probable, entraînant un abaissement du niveau de la bande de valence, donnant ainsi un band gap plus large, situé à environ 1,5 eV. Ces résultats ouvrent donc la possibilité d'ajuster la largeur du band gap du Cu_xSe en modifiant simplement le temps de réaction.

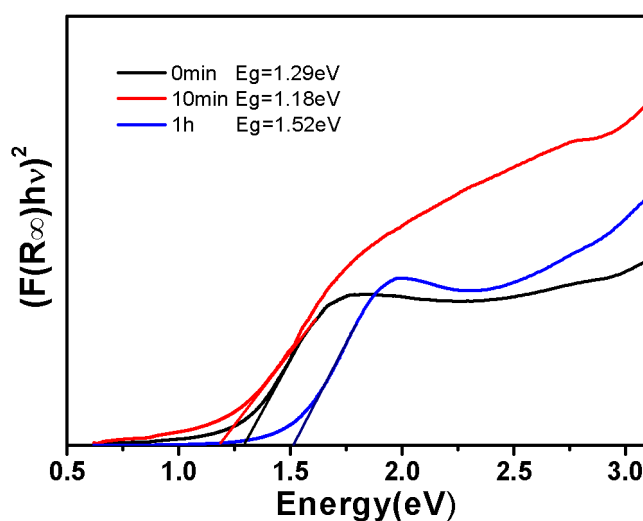


Figure 4. Absorption des Cu_xSe en fonction du temps de réaction à 180 °C

Propriétés thermoélectriques des matériaux à base de Cu_3SbSe_4

Le Cu_3SbSe_4 étudié précédemment pour des applications photovoltaïques est également un matériau très intéressant pour des applications thermoélectriques. Un bon matériau thermoélectrique doit avoir une bonne conductivité électrique, une faible conductivité thermique et un grand coefficient de Seebeck, ce qui n'est pas tout à fait le cas de Cu_3SbSe_4 . Afin d'améliorer ces propriétés, une substitution partielle de Sb par Sn a été étudiée.

Pour obtenir des matériaux massifs denses, des nanoparticules avec une forme quasi sphérique et une taille mono-disperse ont été préparées avec un procédé d'injection rapide. La taille de nanoparticules est contrôlable de façon reproductible avec le temps de réaction. Ces nanoparticules ont été ensuite mises en forme par pressage à chaud.

Les bonnes propriétés nécessaires pour obtenir un matériau thermoélectrique efficace sont parfois contradictoires et les meilleurs compromis ont été obtenus avec le $\text{Cu}_3\text{Sb}_{0.98}\text{Sn}_{0.02}\text{Se}_4$ en substituant 2% de Sb par Sn. Les propriétés les plus importantes ont été comparées pour ces deux composés comme le montre la Figure 5.

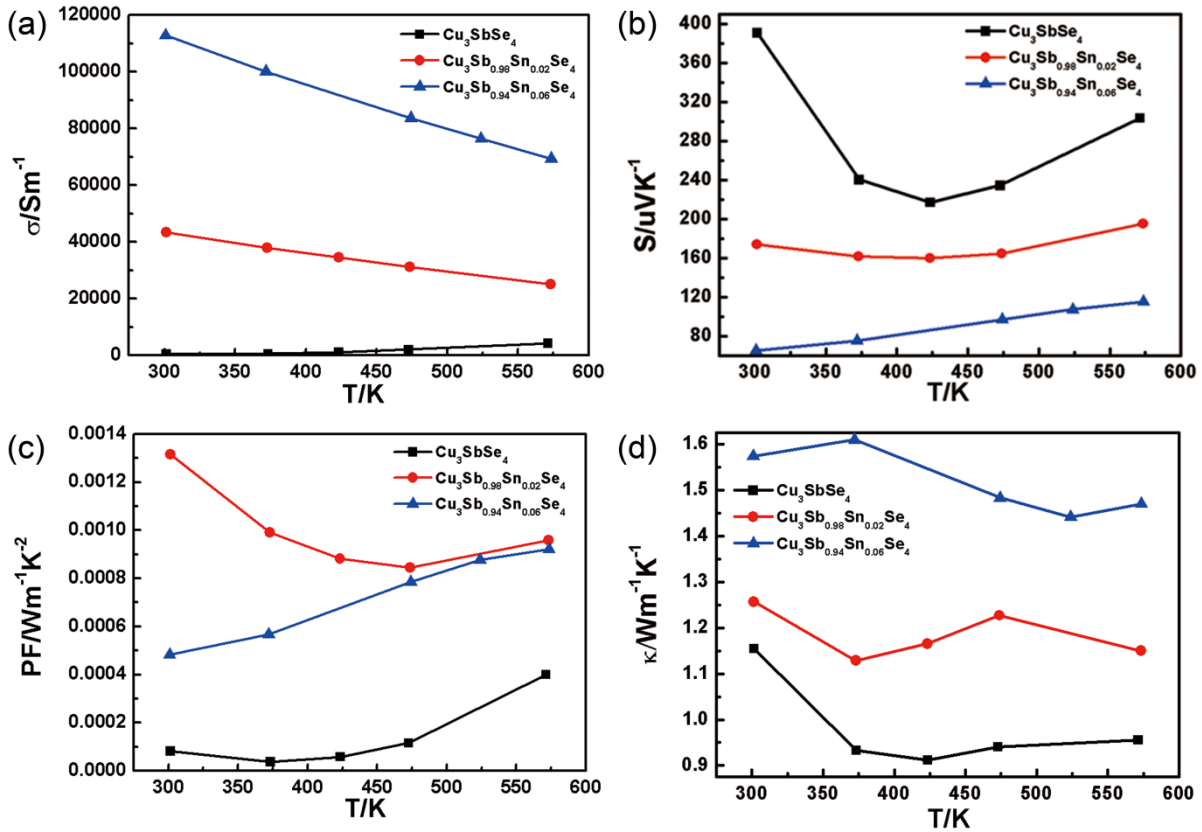


Figure 5. Effet de la substitution de Sb par Sn dans le Cu_3SbSe_4 sur différentes propriétés importantes pour un matériau thermoélectrique

Il est intéressant de constater que la substitution de 2% de Sb par Sn entraîne une augmentation phénoménale, de plusieurs ordres de grandeur, de la conductivité électrique (σ) avec un plus un changement du type de conduction (Figure 5 a). En effet, l'évolution de la conductivité électrique en fonction de la température pour ces deux matériaux montre que Cu_3SbSe_4 est un semi-conducteur. L'introduction de Sn donne un matériau à conduction métallique. Même si l'addition de Sn entraîne une diminution de coefficient de Seebeck (S) (Figure 5 b) et une augmentation légère de la conductivité thermique (κ) (Figure 5 d), le matériau dopé au Sn présente un facteur de puissance ($S^2\sigma$) (Figure 5 c) nettement supérieur.

Par conséquent, le facteur de mérite ($ZT = S^2 \sigma T / k$) est également nettement amélioré grâce au dopage de Sn et il atteint une valeur très intéressante de 0,5 à 575K (Figure 6).

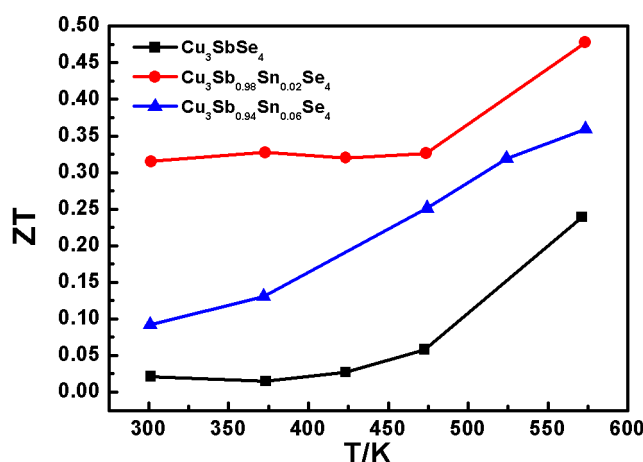


Figure 6. Facteur de mérite du Cu_3SbSe_4 pur et dopé au Sn

Conclusions

Ce travail de thèse porte sur l'étude des céramiques semiconductrices à base de séléniures pour la conversion de l'énergie solaire ou thermique en électricité. C'est un travail exploratoire visant tout d'abord à développer des semi-conducteurs inorganiques contenant des hétérojonctions pour faciliter la séparation de porteurs de charge photogénérés. Ces premiers résultats présentés ici sont très encourageants en démontrant la faisabilité d'un nouveau type de matériaux pouvant être très efficaces pour un nouveau concept de cellules solaires photovoltaïques. Beaucoup d'efforts sont encore nécessaires afin de comprendre le mécanisme d'absorption optique, de génération et de transport de porteurs de charge dans ces matériaux composites.

D'autres céramiques à base de séléniures ont été également étudiées en insistant sur le développement de procédé de fabrication pour obtenir des nanoparticules de très grande qualité. C'est une étape indispensable pour faciliter la densification de céramiques. Une substitution partielle d'antimoine par l'étain dans le Cu_3SbSe_4 a permis d'obtenir un matériau avec un facteur de mérite très encourageant pour l'application thermoélectrique.

Ce travail présente un intérêt fondamental inédit qui mérite d'être poursuivi. Il présente également un potentiel d'applications important. Cette étude a été réalisée avec le souci permanent de privilégier des éléments non toxiques et abondants dans la nature.

General introduction

The acceleration of global economic development and improvement of living standards of the population increase dramatically energy demand, which is now satisfied mainly by non-renewable fossil fuels that are oil, coal and natural gas. The depletion of these natural resources is certain to more or less long term. One of the great challenges facing humanity for sustainable development is to find renewable energy sources.

Among the possible renewable resources, solar energy has by far the greatest potential compared to other sources (hydro, wind, tide ...). Indeed, solar energy arriving on the Earth each year corresponds to approximately 10,000 years of global consumption at current rate. Solar energy is already widely directly or indirectly exploited by mankind with more or less efficiency. Its conversion into electrical energy has received special attention in recent years around the world and a large capacity has already been installed. This is essentially due to the use convenience and ease of transportation of this energy. Most of the already installed photovoltaic systems generate electricity which is still economically not competitive compared to that produced from fossil fuels. In addition, some photovoltaics systems still use rare or toxic elements. Research on efficient materials for the conversion of solar energy is still one of the most promising scientific subjects. .

Solar energy conversion mainly includes photothermal conversion, photovoltaic conversion and photochemical conversion. Among them, photovoltaic solar cells are the most favored technique to convert solar energy into electricity, which can be classified into three main groups: silicon solar cells (single crystalline, polycrystalline, amorphous), organic solar cells (e.g. polymer solar cells, dye-sensitized solar cells) and compound solar cells (e.g. CdTe, GaAs and CIGS). Silicon solar cells are the oldest and also the most matured technology in solar cell market. Single p-n junction crystalline silicon devices are now approaching the theoretical limiting power efficiency of 33.7%, noted as the Shockley–Queisser limit. Therefore, multi-junction structure, which is able to absorb a wider range of the solar spectrum, has been proposed for further increasing the conversion efficiency. The GaInP/GaAs/GaInNAs three-junction system has achieved the highest conversion efficiency of 43.5%. Another important research direction of solar cells is thin film solar cells due to its promising advantages compared to crystalline silicon solar cells, such as flexibility, lightweight, lower production cost. Thin-film technology has always been cheaper but less efficient than conventional c-Si technology. However, its efficiency has been significantly

improved over the years. The lab cell efficiency for CdTe and CIGS is now beyond 21%, outperforming multicrystalline silicon, the dominant material currently used in most solar PV systems. Cadmium telluride is the only thin film material so far to rival crystalline silicon in terms of cost/watt. However cadmium is toxic and tellurium supplies are limited. To date, most of the explorations of new photovoltaic materials are based on thin film solar cells. The two relatively new thin film solar cells, dye-sensitized solar cells and organic photovoltaic cells, are making rapid progress in laboratory efficiencies.

The most dramatic advance in this area in recent years is undoubtedly solar cells based perovskite which already reach an efficiency of 20% with a potentially low-cost manufacturing technology. Chemical durability and lead content are among the issues to be resolved before a real marketing.

In recent years, looking for new low-cost, environment-friendly and efficient alternative materials has become an important research topic for solar cell research. It is more and more meaningful to find a single material to achieve high performance and to simplify production process in photovoltaic applications. Therefore, the development of composite structure has become particularly interesting in order to address separately different issues (strong absorption of solar spectrum, efficient charge generation and separation...) with different components/structures and achieve superior performance ultimately.

The objective of the first part of this work is to explore a totally new photoelectric ceramic with self-organized microstructure, which is mainly determined by the material composition. Consequently emphasis will be put on the establishment of the relationship between the composition, the microstructure (crystalline phases and composite structure) and the properties (photoelectric and resistivity) of the ceramics. The objective is to understand the mechanism of charge generation, separation and transport in order to design appropriate structures for efficient photon-electron/hole conversion. This work is inspired by previous works of our laboratory on the $\text{GeSe}_2\text{-Sb}_2\text{Se}_3\text{-CuI}$ glass ceramics which can contain a heterojunction network formed by p-type semiconductor Cu_2GeSe_3 and n-type Sb_2Se_3 . This network is the origin of some unusual and very interesting photoelectric properties. In this work, pure ceramics without amorphous phase have been firstly prepared and studied in the $\text{Cu}_2\text{GeSe}_3\text{-Sb}_2\text{Se}_3$ system. And then $\text{Cu}_3\text{SbSe}_4\text{-Sb}_2\text{Se}_3$ ceramics have been also studied with the objective to eliminate the germanium which is a relatively rare element.

The development of high efficiency thermoelectric materials is another possibility, less considered, for solar energy harvesting. This technique allows to use all temperature differences for power generation and refrigeration. However, the thermoelectric conversion efficiency is still relatively low and mainly limited by the performance of thermoelectric materials, which should have high electric conductivity, low thermal conductivity and high seebeck coefficient. Some of the research efforts are on minimizing the lattice thermal conductivity, while other efforts are focused on materials that exhibit large power factors. Most of the earlier investigations mentioned so far are based on binary intermetallic semiconductor systems. Recent approaches to develop high-performance bulk TE materials use ternary and quaternary chalcogenides containing heavy atoms with low dimensional or isotropic complex structures to take advantage of the large carrier's effective mass and low lattice thermal conductivity associated with such systems. As an example, the figure of merit ZT of $\text{Yb}_{14}\text{MnSb}_{11}$ sharply increases with temperature and reaches a maximum of ~ 1.0 at 1223 K. With the low thermal conductivity, the ZT of $\beta\text{-Cu}_2\text{Se}$ reached a value of ~ 1.5 at 1000 K. I-V-VI₂ semiconductors, BiCuSeO oxyselenides and SnSe single crystals are also promising thermoelectric materials.

Nano-structuration is also an effective approach to reduce the lattice thermal conductivity but can also cause a stronger charge carrier scattering. Therefore, the performance of the thermoelectric materials is largely dependent on the preparation method which can greatly change their microstructure. In this part of work, $\text{Cu}_3\text{Sb}_{1-x}\text{Sn}_x\text{Se}_4$ nanoparticles with a narrow size distribution were synthesized through a hot-injection route. The $\text{Cu}_3\text{Sb}_{1-x}\text{Sn}_x\text{Se}_4$ nanoparticles-based bulk materials were then prepared by hot-pressing of the nanoparticles and their thermoelectric performances were systematically studied.

As both photoelectric and thermoelectric material, copper selenide nanoparticles and two-dimensional single crystal nanoplates were also synthesized. The structure of the nanocrystals has been studied and the formation mechanism of the nanoplates has been proposed.

All the studied materials are based on selenides and are narrow gap semiconductors. This will offer the possibility of selecting appropriate compounds with aligned Fermi levels for designing high performance photovoltaic system.

Chapter I: Solar energy conversion.

1.1 Introduction

Energy crisis and related environmental issues are the two biggest challenges of humanity in the 21st century. Energy plays a crucial role in the development of the economies and for the life quality of the people. The rate of worldwide energy consumption reached 15 TW in 2008 and is expected to nearly double by 2050 due to the growing global production and population [1]. While in the present scenario, conventional energy sources based on oil, coal, and natural gas are playing lead role to meet the energy demand and have proven to be highly effective drivers of economic progress. About 85% of our energy comes from fossil fuels, a finite resource unevenly distributed beneath the Earth's surface. Reserves of fossil fuels are progressively decreasing, and furthermore, their continued combustion produces a series of harmful effects such as air and water contamination that threatens human health and greenhouse gases associated with global warming. Prompt global action to solve the energy crisis is therefore needed. To pursue such an action, we are urged to save energy and to use energy in more efficient ways, but we are also forced to find alternative renewable energy sources.

The energy systems considered as the whole of the energy supply sector, which converts the primary energy to energy carriers. And the end-use technologies needed to convert these energy carriers to deliver the demanded energy services, have developed significantly over time. Two main transitions can be distinguished in the history of the energy system [2-4]. The first was the transition from wood to coal in the industrialising countries, initiated by the steam engine in the late 18th century. By the turn of the 20th century, nearly all primary energy in industrialised countries was supplied by coal. The second transition was related to the proliferation of electricity, which was the first energy carrier that could easily be converted to light, heat or work at the point of end use. Furthermore, the introduction of the internal combustion engine increased mobility, as cars, buses and aircraft were built, and stimulated the use of oil for transportation. These innovations together lead to a shift in the mix of commercial energy sources from mainly coal towards domination of coal, oil and later natural gas and increased the global commercial primary energy use from 1850 to 1990 by a factor of about 40% [2]. At present, consumption of fossil fuels is dramatically increasing along with improvements in the quality of life, industrialization of developing nations, and increase of the world population. Currently, the world's growing thirst for oil amounts to

almost 1000 barrels a second, which corresponds to about 2 liters per day per person living on Earth[5]. The global energy consumption is equivalent to 15 trillion watts (15 TW) of power demand, which is expected to increase by 50% by 2030[6].

It has long been recognized that this excessive fossil fuel consumption not only leads to an increase in the rate of diminishing fossil fuel reserves, but it also has a significant adverse impact on the environment. Human health, regional and local air pollution and ecosystems are threatened due to energy-related emissions like suspended fine particles and precursors of acid deposition. The potentially most important environmental problem relating to energy is global climate change (global warming or the greenhouse effect). The increasing concentration of greenhouse gases such as CO_2 , CH_4 , CFCs, halons, N_2O , ozone, and peroxyacetylnitrate in the atmosphere is acting to trap heat radiated from Earth's surface and is raising the surface temperature of Earth [7]. A schematic representation of this global climate change problem is illustrated in Fig. 1.1. Many scientific studies reveal that overall CO_2 levels have increased 31% in the past 200 years, 20 Gt of Carbon added to environment since 1800 only due to deforestation and the concentration of methane gas which is responsible for ozone layer depletion has more than doubled since then. The global mean surface temperature has increased by $0.4\text{--}0.8^\circ\text{C}$ in the last century above the baseline of 14°C . Increasing global temperature ultimately increases global mean sea levels at an average annual rate of 1-2mm over the last century. Arctic sea ice thinned by 40% and decreased in extent by 10–15% in summer since the 1950s[8].

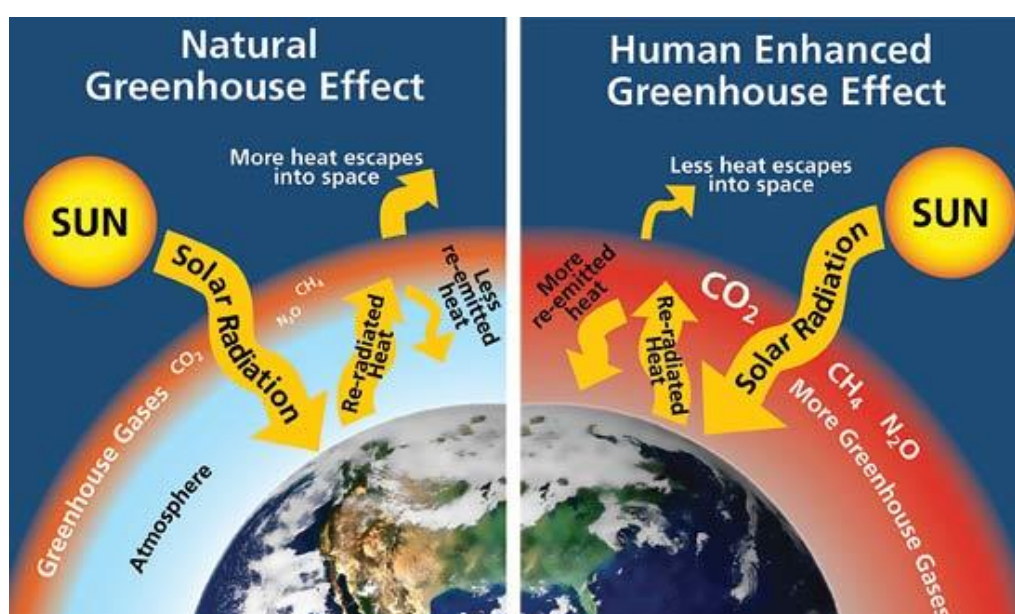


Fig. 1.1 Schematic illustration of greenhouse effect

Changes towards environmental improvements are becoming more politically acceptable globally, especially in developed countries. Society is slowly moving towards seeking more sustainable production methods, waste minimization, reduced air pollution from vehicles, distributed energy generation, conservation of native forests, and reduction of greenhouse gas emissions[9]. Therefore, renewable promotion of clean energy is eagerly required [10]. An agreement to monitor emission of these greenhouse emissions was made with the overall pollution prevention targets, the objectives of the Kyoto Protocol agreement[11].

One of the pathways to follow in order to achieve the goals of sustainable development is an increased reliance on renewable energy. The energy resources have been split into three categories: fossil fuels, renewable resources and nuclear resources[12]. Renewable energy sources are those resources which can be used to produce energy again and again, e.g. solar energy, wind energy, biomass energy, geothermal energy, etc. and are also often called alternative sources of energy[13]. For now, renewable energy sources (RES) supply 14% of the total world energy demand. Renewable energy conversion technologies generally depend on energy flows through the earth's ecosystem fed by solar radiation and on the geothermal energy of the earth[14]. RES includes biomass, hydropower, geothermal, solar, wind and marine energies, which are clean or inexhaustible energy resources [15, 16]. Large-scale hydropower supplies 20 percent of global electricity. Wind power in coastal and other windy regions is promising source of energy [17, 18]. Main renewable energy sources and their usage forms are given in Table 1.1. Shares of energy sources in EU-28's total production of primary energy in 2014 are showed in Fig. 1.2. The share of RES in total global primary energy supply is expected to increase very significantly (30–80% in 2100)[18]. Renewables are expected to be suitable alternatives in a sustainable energy future for several reasons[14]:

Renewable energy sources that meet domestic energy requirements have the potential to provide energy services with zero or almost zero emissions of both air pollutants and greenhouse gases. Renewable energy system development will make it possible to resolve the presently most crucial tasks like leading to a diversification of energy sources and improving energy supply reliability by increasing the share of a diverse mixture of renewable sources,

and thus to an enhanced energy security; solving problems of local energy and water supply; improving the development of local economies and creating jobs for the local population; ensuring sustainable development of the remote regions in the desert and mountain zones; implementation of the obligations of the countries with regard to fulfilling the international agreements relating to environmental protection[19]. Development and implementations of renewable energy project in rural areas can create job opportunities and thus minimizing migration towards urban areas[20]. Harvesting the renewable energy in decentralized manner is one of the options to meet the rural and small scale energy needs in a reliable, affordable and environmentally sustainable way[21].

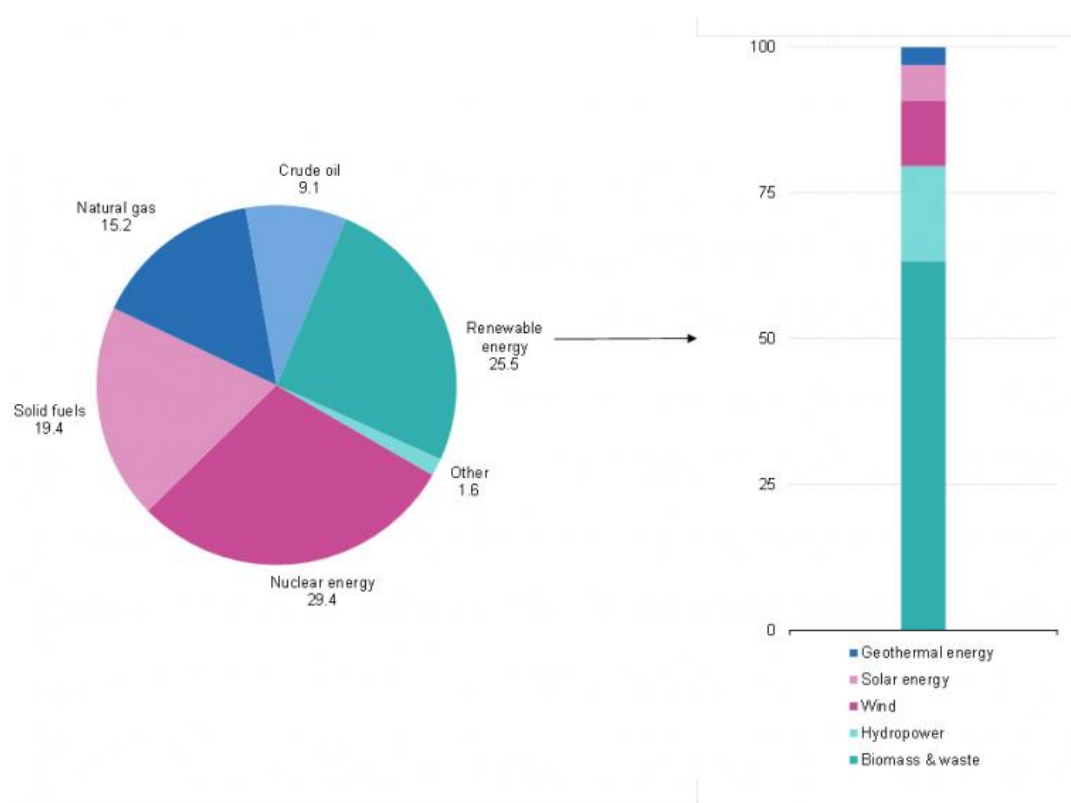


Fig. 1.2 Shares of energy sources in EU-28's total production of primary energy in 2014

Table 1.1 Main renewable energy sources and their usage form[22]

Energy source	Energy conversion and usage options
Hydropower	Power generation
Modern biomass	Heat and power generation, pyrolysis, gasification, digestion
Geothermal	Urban heating, power generation, hydrothermal, hot dryrock
Solar	Solar home system, solar dryers, solar cookers
Direct solar	Photovoltaic, thermal power generation, water heaters
Wind	Power generation, wind generators, windmills, water pumps
Wave	Numerous designs
Tidal	Barrage, tidal system

1.2 Solar energy

Solar energy is widely accepted as a free, abundant and endlessly renewable source of clean energy, which could meet current and future human energy demand. Carrying out analysis on the origin, all the energy sources are directly or indirectly derived from solar radiation. Biomass energy is produced by plants as a result of photosynthesis generated by the sun; wind energy is also indirectly derived from the heat generated by the sun. Among these renewable energy sources, solar energy has received much attention in solving the environmental and energy crisis due to its clean and inexhaustible feature, and thus occupies a

central position as renewable energy. Efficient utilization of solar energy could alleviate many energy and environmental issues, as the solar energy irradiating upon the Earth's surface (1.3×10^5 TW) exceeds the current global human energy consumption (1.6×10^1 TW in 2010) by roughly four orders of magnitude[23].

Solar energy has an enormous potential but cannot be employed directly; it must be captured and converted into useful forms of energy. Thus, the harvest and conversion of solar energy into a usable energy form is highly desirable[24]. Because solar power is diffuse (342 Wm^{-2}) and intermittent, conversion should involve concentration and storage. Solar energy conversion mainly includes photothermal conversion, photovoltaic conversion and photochemical conversion.

1.2.1 Solar energy conversion

1.2.1.1 Photothermal conversion

Solar thermal power generation is an important direction of solar energy utilization. Solar thermal energy (STE) is a form of energy and a technology for harvesting solar energy to generate thermal energy or electrical energy for use in industry, and in the residential and commercial sectors.

Solar thermal collectors are classified by the United States Energy Information Administration as low-, medium-, or high-temperature collectors. Low-temperature collectors are flat plates generally used to heat swimming pools. Medium-temperature collectors are also usually flat plates but are used for heating water or air for residential and commercial use. High-temperature collectors concentrate sunlight using mirrors or lenses and are generally used for fulfilling heat requirements up to $300^\circ\text{C}/20$ bar pressure in industries and for electric power production. Two categories include Concentrated Solar Thermal (CST) for fulfilling heat requirements in industries, and Concentrated Solar Power (CSP) when the heat collected is used for power generation. CST and CSP are not replaceable in terms of application.

In the modern sense, the whole contents of the development of solar energy conversion technology can be divided into two main aspects:

- a. To collect solar energy efficiently, the key parameters includes:

- (1) Selective surface technology;
- (2) The optical design of receives;
- (3) Thermal structure design and analysis of solar energy collector
- (4) The mechanical structure design of device.

b. To convert the collected solar energy to other useful forms, the main technical issues include:

- (1) Reduce the all kinds of heat and electricity loss in the process of energy conversion;
- (2) Excellent system design.

Solar energy heating is the most obvious application of the solar energy. The efficiency of solar energy heating utilization, in other words, the thermal conversion efficiency, mainly depends on the quality and performance of solar radiation collectors. Therefore, the solar energy collector is one of the most critical parts of solar-thermal conversion process.

Solar cooling can also be achieved for a building or district cooling network by using a heat-driven absorption or adsorption chiller (heat pump). There is a productive coincidence that the greater the driving heat from insulation, the greater the cooling output. In 1878, Auguste Mouchout pioneered solar cooling by making ice using a solar steam engine attached to a refrigeration device[25].

Solar collectors mainly include flat collectors and concentrating collectors.

Flat plate collector is a kind of not concentrating collectors, which means that the absorption area of solar radiation equals to the collector surface in size. It is known as concentrating collectors if the absorption area is larger. Flat collectors are mainly used for the application of water heating, domestic heating and refrigeration. With a high heat loss coefficient, the working temperature are usually under 80°C. This limits the scope of its use.

In order to improve solar collector utilization in medium and high temperature, we must improve the operation characteristics. Concentrating collectors were born as the only way for the development. In the mid-high temperature solar energy utilization, the current research

directions mainly include the medium temperature solar industrial heating, solar refrigeration and air conditioning and high temperature solar thermal power technology. Concentrating solar thermal systems take advantage of the abundant, high-quality energy resource of the sun. The energy conversion process is as following: These systems firstly concentrate beam radiation onto a receiver and then the radiation is converted to thermal energy to be used in heat engine to produce work or electricity (see Fig. 1.3). Beam radiation is concentrated onto a smaller surface in order to minimize radiative heat losses and to achieve higher temperatures for thermal cycles to produce higher efficiencies.

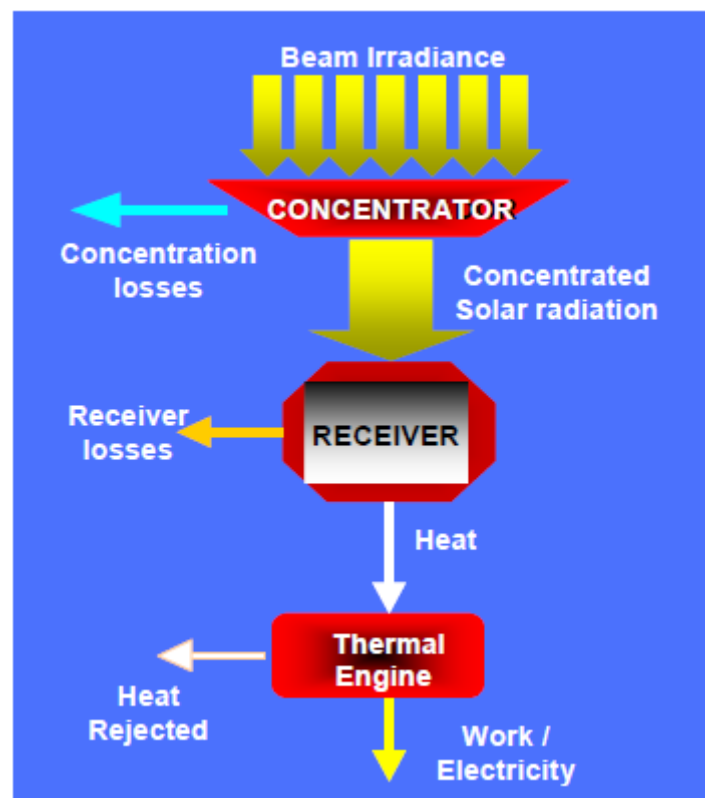


Fig. 1.3 Basic configuration of the Concentrating Solar Power (CSP)

There are typically four main types of concentrating systems: trough, tower, dish and Fresnel reflection (Fig. 1.4).

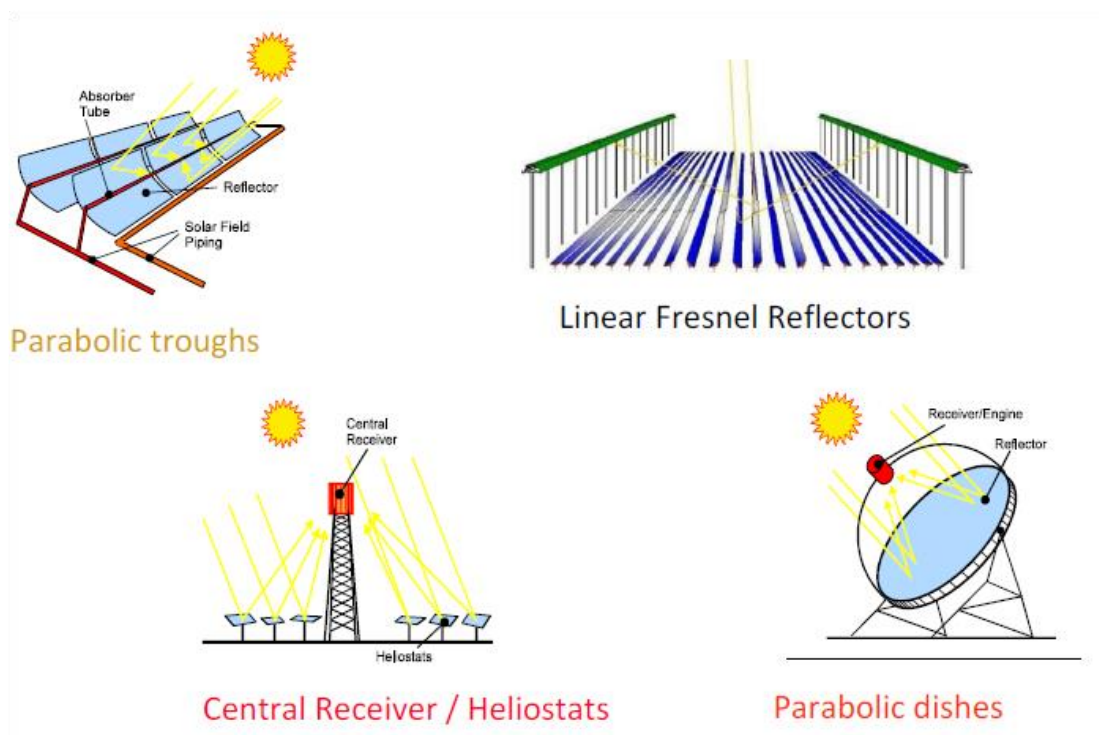


Fig. 1.4 Typical concentrating technologies

1.2.1.1.1 Tracking Systems

One-axis and two-axis tracking systems orient solar receivers or reflectors towards the sun in both Solar PV arrays and CSP technologies. In concentrating solar power applications, orienting the reflector towards the sun optimizes solar power output. This technology is especially important for parabolic trough and parabolic solar dish technologies that require some type of tracking to be effective over the course of the day.

Parabolic Trough

Parabolic collectors use the geometry of a parabola (or ellipse) to focus the incoming solar radiation on to a point at the focus. They are moving on a 1-axis-tracking system according to the sun's movement. These systems use a heat transfer fluid (at the focus) to collect the thermal energy and transfer it to a working fluid in a Rankine Cycle.

Parabolic Dish

Solar Thermal Parabolic Dishes are two-axis tracking parabolic dishes that are able to focus all of the sun's direct radiation to one point (instead of one line as with parabolic trough). Most modern designs direct the sun's energy towards a Stirling engine which converts solar

thermal energy into mechanical energy and finally into electricity. Dishes are modular ranging in power from 3 to 25 kW. Multiple solar dishes are installed on one site to produce a significant amount of energy.

Central Receiver System (Power Tower)

In a central receiver system, commonly called a power tower, a field of heliostat mirrors are used to track the sun and reflect its light towards a central point at the top of the tower. the power tower generates heat of about 1,000 °C. By transferring the reflected concentrated solar radiation to a fluid, steam is being produced that expands on a turbine in order to generate the electricity.[22] Thermal storage can easily be used to store energy for electricity production after the sun goes down. Currently the largest power tower plant exists in Spain producing 20 MW.

Linear Fresnel

This technology uses flat mirrors with on unique focal point. Water flows through the pipe which runs directly through the focal point of the mirrors. The Linear Fresnel arrangement approximates the parabolic shape of trough systems. It is a simple receiver design that facilitates direct steam generation. Thus, heat transfer fluids are not needed while applying this technology.

1.2.1.1.2 Thermal Energy Storage (TES)

Thermal energy storage technologies store energy in a thermal reservoir for use later. TES can be coupled with CSP technologies by storing some portions of energy generated during daylight hours for use as solar energy diminishes. It can be important in extending solar energy generation to address evening energy demands. Currently, parabolic trough and central receiver systems utilize molten nitrate salts for thermal energy storage. Molten nitrate salts have a viscosity similar to that of water, making them easy to pump. However, great care must be taken to maintain them at high enough of a temperature to preclude freezing/solidification.

1.2.2 Photochemical conversion

Photosynthetic organisms are ubiquitous in nature; they are responsible for the development and sustenance of all life on Earth. They may be quite different, but all of them use the same basic strategy, in which light is initially absorbed by antenna proteins containing many chromophores, followed by energy transfer to a specialized reaction center protein, in

which the captured energy is converted into chemical energy by means of electron-transfer reactions[26]. Photochemical conversion and storage of solar energy has been a subject of considerable interest in the past few years.

There are many forms of photochemical conversion, but the main form is photocatalysis which is widely applied in industry product and science research. In chemistry, photocatalysis is a reaction which uses light to activate a substance which modifies the rate of a chemical reaction without being involved itself. The significant features of the photocatalytic system are the desired band gap, suitable morphology, high surface area, stability and reusability.[27-29] Photocatalytic technology is expected to become an effective way to solve the problem of environment and energy. Through converting solar energy into clean hydrogen, water splitting technology will completely solve the crisis of fossil energy depletion. And the light catalytic degradation technology which is able to remove toxic organic pollutants will be a potential solution to environmental problems.

Photocatalysis using semiconductors under irradiation has been extensively studied for about three decades. In 1972, Fujishimna and Honda discovered the photocatalytic splitting of water on TiO_2 electrodes. This event marked the beginning of a new era in heterogeneous photocatalysis. Hydrogen production from water photolysis, as a new way to utilize renewable solar energy, has attracted more and more attentions.[30] Another main focus of previous studies has been to investigate the principal applicability of photocatalysis systems for efficient treatment of water polluted with toxic substances. Quantum size effects on photoreactions for semiconductor nanoparticles have only been recently studied. Today, semiconductors are usually selected as photocatalysts, because semiconductors have a narrow gap between the valence and conduction bands. In order for photocatalysis to proceed, the semiconductors need to absorb energy equal to or more than its energy gap. This movement of electrons forms e^-/h^+ or negatively charged electron/positively charged hole pairs. The hole can oxidize donor molecules. Semiconductor photocatalysts are semiconductors which are able to cause and/or to accelerate chemical reactions upon light absorption, typically sunlight. By utilizing the energy of absorbed photons, photocatalysts can be optimized to carry out a wide variety of important chemical processes such as (Fig. 1.5):

- Environmental remediation - the destruction of organic pollutants for water or air purification
- Solar Fuels Production - production of fuels, H_2 from water or methane/methanol from CO_2

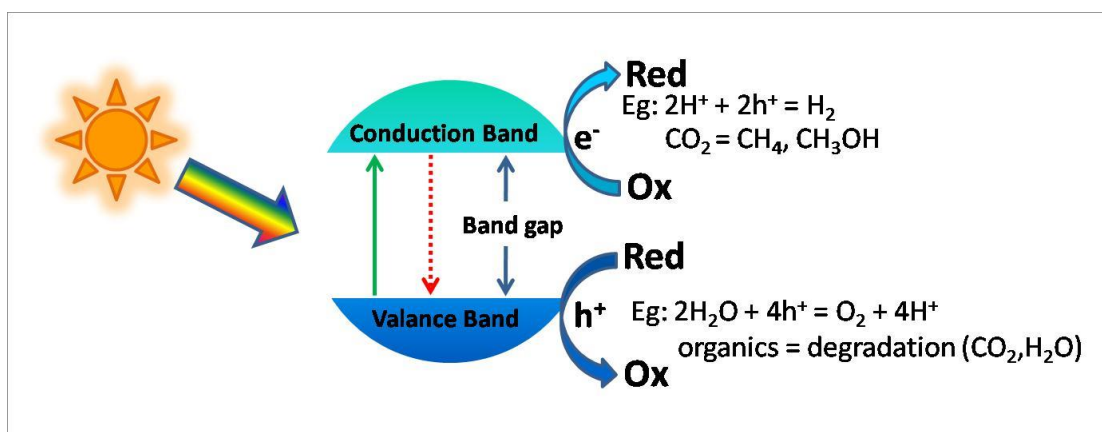


Fig. 1.5 Main processes of photocatalytic fuel production or depollution

1.2.2.1 Electrochemical water splitting

The water splitting reaction is an uphill reaction in which the Gibbs free energy increases by 237 kJ.mol^{-1} . The energy needed to drive photocatalytic and PEC water splitting is provided by light or ideally sunlight. There are usually three steps during this process of water splitting as follows (Fig. 1.6).

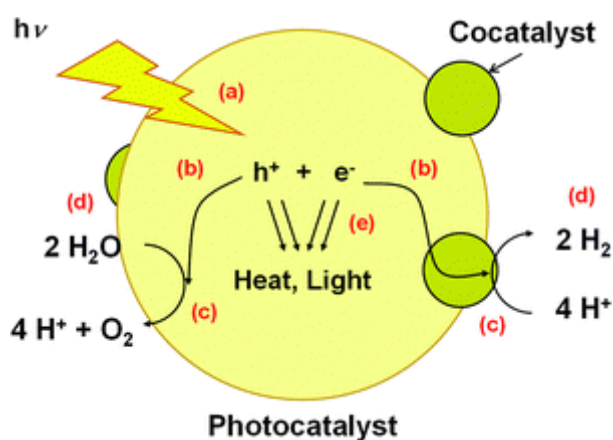


Fig. 1.6 Reaction processes of water splitting on a heterogeneous photocatalyst. (a) Light absorption, (b) charge transfer, (c) redox reactions, (d) adsorption, desorption, and mass diffusion of chemical species, and (e) charge recombination[27]

The first step (i) is absorption of photons to form electron–hole pairs (Fig 1.6 (a)). Under suitable illumination, when a semiconductor absorbs photons with energies higher than its band gap energy, electrons in the valence band are excited to the conduction band. As a result, excited electrons and holes are generated in the conduction and valence bands, respectively. These photogenerated carriers can drive reduction and oxidation reactions if the charge injections into the reactants are thermodynamically favourable. Direct bandgap materials absorb more efficiently than indirect bandgap materials. Water molecules are reduced by the electrons to form H_2 and are oxidized by the holes to form O_2 for overall water splitting. Important points in the semiconductor photocatalyst materials are the width of the band gap and levels of the conduction and valence bands. The bottom level of the conduction band has to be more negative than the redox potential of H^+/H_2 with respect to the normal hydrogen electrode (NHE), while the top level of the valence band be more positive than the redox potential of O_2/H_2O (1.23 V).

The second step (ii) consists of charge separation and migration of photo-generated carriers (Fig 1.6 (b)). Crystal structure, crystallinity and particle size strongly affect this step. The higher the crystalline quality is, the smaller the amount of defects is. The defects operate as trapping and recombination centers between photo-generated electrons and holes, resulting in a decrease in the photocatalytic activity. If the particle size becomes small, the distance that photo-generated electrons and holes have to migrate to reaction sites on the surface becomes short and this results in a decrease in the recombination probability.

The third step (iii) is surface chemical reactions (the construction of surface reaction active sites for the evolution of H_2 and O_2) (Fig 1.6 (c)). Photo-excited holes accumulate on the surface of the semiconductor and are consumed in oxidation reactions, while electrons are used in reduction reactions. The important points for this step are surface character (active sites) and quantity (surface area). Even if the photogenerated electrons and holes possess

thermodynamically sufficient potentials for water splitting, they will have to recombine with each other if the active sites for redox reactions do not exist on the surface.

A sufficiently negative flat band potential, a good absorption cross-section over a wide spectral range, photostability and an appropriate band gap are also essential. In this context, metal oxides such as TiO_2 [31-33], SrTiO_3 [34, 35] and NaTiO_3 [36, 37] based materials have been studied in detail as a result of their suitable band structures, low environmental impact and low toxicity as well as high stability. However, Sunlight (AM1.5G) consists of three main components in terms of wavelengths: ultraviolet (UV) rays ($\lambda < 400$ nm), visible light ($400 \text{ nm} < \lambda < 800$ nm), and infrared rays ($\lambda > 800$ nm), accounting for 4, 53, and 43% of the total solar energy, respectively. These wide band gap oxides have only low conversion efficiencies as they are only active under UV light, which accounts for just 4% of the solar spectrum. It is necessary to harvest visible light for effective solar-to-chemical conversion because UV light accounts for only a small portion of solar energy. And it is important to understand the complex interface electron dynamics in all of these assemblies which will allow us to use these systems in various applications. Co-catalysts(Fig(1.6)) and/or the addition of sacrificial agents(SRs)(Fig 1.7(c)) to photocatalyst can result in an improved performance[30, 38].

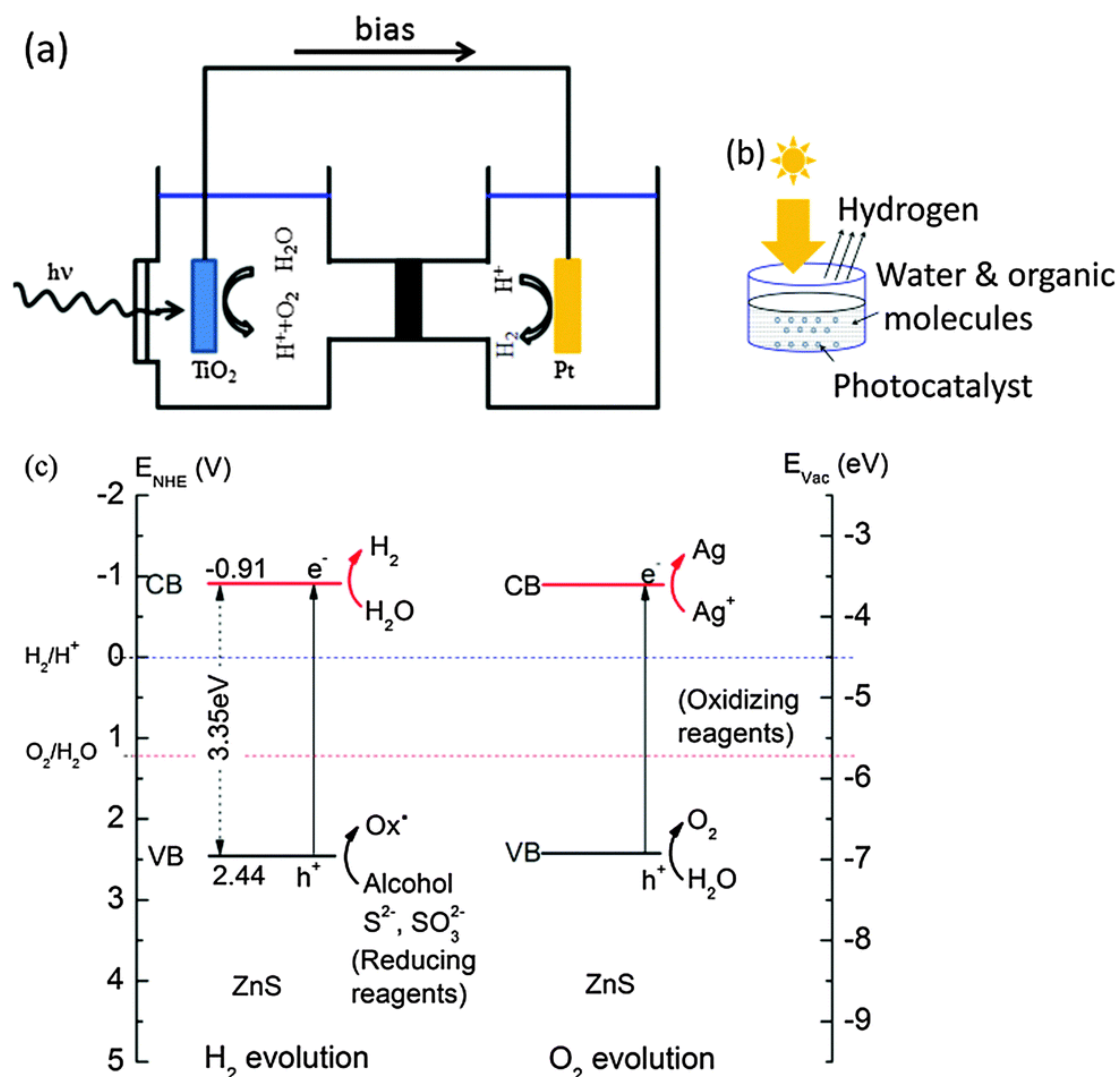


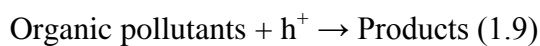
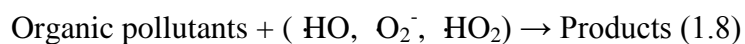
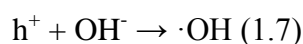
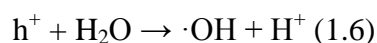
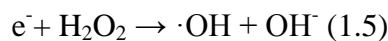
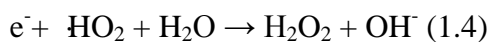
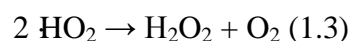
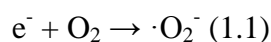
Figure 1.7. Schematic diagrams of the setup for photo electrochemical water splitting: (a) after Fujishima and Honda[38]; (b) using powdered photocatalysts (after Bard[39]); and (c) basic principle of water splitting with photocatalyst materials (after Kudo and Misekia[30])

1.2.2.2 Environmental remediation

The utilization of heterogeneous photocatalysis for environmental purification (both in the liquid and gas phase) has been extensively investigated as photoactivated semiconductors have proven activities to unselectively mineralize various types of toxic, refractory and non-biodegradable organic pollutants under mild conditions.[40] The basement for the

destruction of organic pollutants for water or air purification is quite similar expect for the requirement of the band edge of the semiconductors.

The photo-generated electrons can react with the adsorbed O_2 on the semiconductor surface and form various active substances, such as O_2^- , HO_2 , H_2O_2 , $\cdot OH$, etc (formula 1.1-1.5). Meanwhile, the photo-generated holes will react with the adsorbed H_2O or OH^- ions on the semiconductor surface and generate hydroxyl radicals $\cdot OH$ (formula 1.6, 1.7). These active substances can decompose most organic compounds (formula 1.8). In addition, for the most used photocatalyst such as anatase TiO_2 ($E_g = 3.2$ eV), since the electric potential of its photo-generated hole is greater than 3.0 eV, which is higher than that of chlorine, ozone and permanganate, thus showing strong oxidation. Therefore, such photo-generated holes provide another way to decompose the organic pollutants (formula 1.9)[41].



1.2.3 Photovoltaic conversion

Photovoltaics (PV) are best known as a method covering the conversion of light into electricity using semiconducting materials that exhibit photovoltaic effect, a phenomenon studied in physics, photochemistry, and electrochemistry. The PV effect refers to photons of light exciting electrons into a higher state of energy, allowing them to act as charge carriers

for an electric current. The photovoltaic effect was first observed in 1839 by Alexandre-Edmond Becquerel while studying the effect of light on electrolytic cells. Solar cells were developed rapidly in the 1950s owing to space programs and used on satellites (crystalline Si efficiency of 6–10%). The energy crisis of the 1970s greatly stimulated research and development for PV. Solar cells based on compound semiconductors (III–V and II–VI) were first investigated in the 1960s. At the same time, polycrystalline Si (pc-Si) and thin-film solar cell technologies were developed to provide high production capacity at reduced material consumption and energy input in the fabrication process, and integration in the structure of modules by the deposition process and consequently cost reduction for large-scale terrestrial applications. The rapid growth of the PV market began in the 1980s due to the application of multi-megawatt PV plants for power generation. In the last two decades the global solar PV market has experienced rapid expansion, with an average annual growth rate of 40% (IEA, 2010) and 60% between 2004 and 2009 (REN21, 2010), similar to that of the telecommunication and computer sectors. Approximately 28GW of installed capacity was added in 2012, bringing total Cumulative installed capacity to approximately 100 GW worldwide. A large share of the market is concentrated in Europe, which accounts for 70 GW of the total installed capacity (Fig. 1.8).

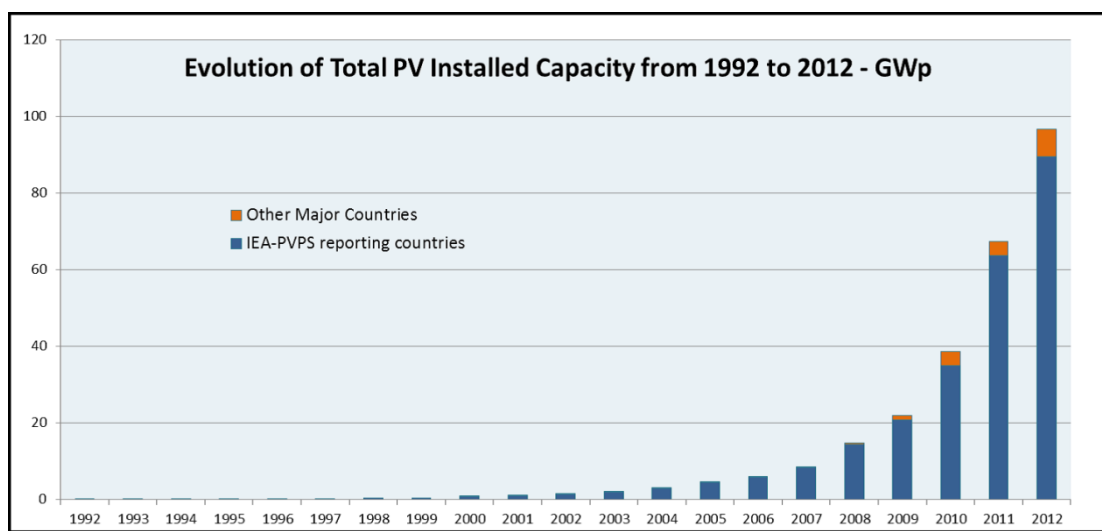


Fig. 1.8 Evolution of total PV installed capacity from 1992 to 2012 (Source: IEA, 2012)

The "photovoltaic effect" is the basic physical process through which a solar cell converts sunlight into electricity. The operation of a photovoltaic cell follows three steps: i) the absorption of light, generating either electron-hole pairs or excitons, ii) the separation of various types of charge carriers, iii) the separate extraction of those carriers to an external circuit.

1.2.3.1 P-N junction: working principle of semiconductor based solar cell

To understand junction effect, we should understand n-type and p-type material. Doping process which means inserting another atom into the bulk crystal is needed to obtain n-type or p-type materials (Fig. 1.9). Consider silicon crystal: each silicon atom has four electrons in its valence band and these electrons make bonds with other silicon atoms. You can see the silicon crystal in the left side with valence electrons of each Si atom. Note that we call that structure as crystal since all Si atoms are perfectly aligned. We can convert this structure in to n-type or p-type semiconductor by doping different atoms. For example, let's dope it by boron. Boron atom has 3 electrons in its valence band. When we insert a B atom instead of a Si atom, one bond between B atom and a Si atom will be very weak. To complete the perfect symmetry in this structure, crystal will be aimed to catch an external electron. As you can see an electron is missing since B atom has 3 electrons in its valence band. This missing bond can be treated as a positively charged particle called 'hole'. This material is called p-type material. When P atom is inserted into the Si lattice, 4 electrons will be able to make bonds with neighbour Si atoms. However, a 5th electron will be hanging on. So, it will be in an energy level very close to the conduction band since it will be nearly free. This nearly free electron can easily leave P atom with a small thermal energy. Note that there is an extra electron in this new structure. So we call this new material n-type material. In contrast to p-type material, n-type material has a tendency to give electrons. Consequently, we have two types of materials. One wants to give electrons and the other wants to receive electrons. We can create a p-n junction by bringing them together.

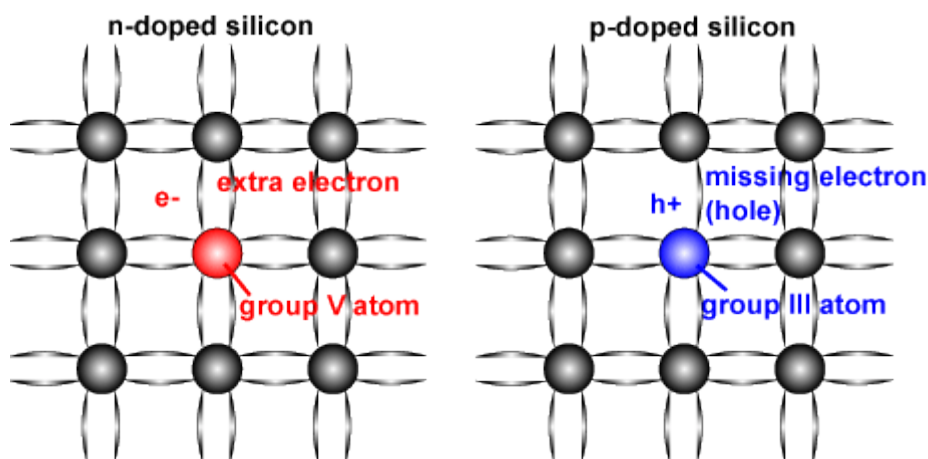


Fig. 1.9 Schematic of a silicon crystal lattice doped with impurities to produce n-type and p-type semiconductor material

When we bring p-type and n-type materials together, diffusion occurs on the surface between them. Electrons start to diffuse from n-type to p-type. Similarly, holes diffuse from p-type region to n-type region. This diffusion creates an electron-hole free region in a very short distance at the interface region. This thin layer is called space region or charge depletion region. Then as you see there is an electric field from the n-side to the p-side of the depletion region. Since the electrons are negative charges this electric field applies a force to an electron entering the depletion region. Any electron generated by sun light in the vicinity of the depletion region may pass to the n-side of the junction very easily. If we connect a wire or any load between the ends of n-type and p-type regions with metal contacts, this electron will flow to the p-type through this external load. So we need an external energy to create this current: something should energize the electrons in the p-type region to enter the depletion region. Solar radiation is an excellent energy source to do this job.

Fig. 1.10 indicates the working principle of semiconductor based solar cells with the following steps for photo charge generation and separation.

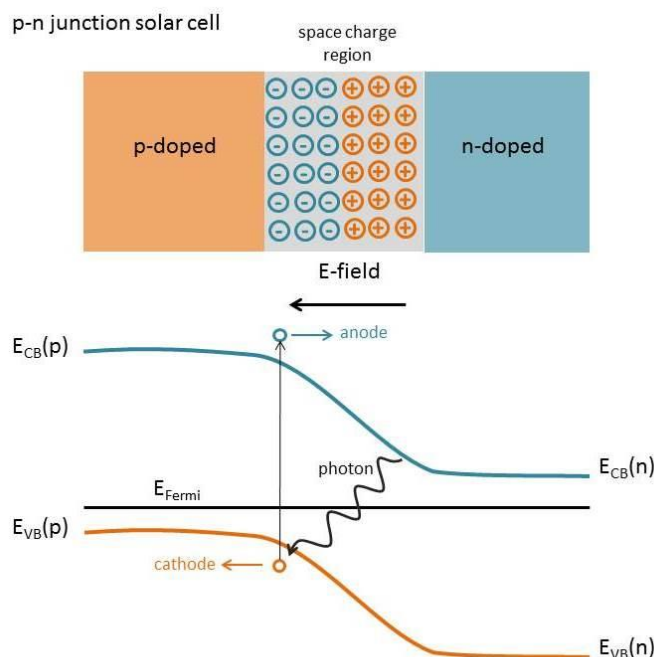


Fig. 1.10 P-N junction: working principle of semiconductor based solar cell

Step (i): Light (photon) absorption by a valence band electron occurs if the photon energy amounts to at least the band gap energy. The excited electron is then in the conduction band of the semiconductor material and free to move, as is the hole in the valence band. In the case of the exciton, the electron and hole are bound until separation occurs.

Step (ii): Because of the electric field at a p-n junction, photoexcited electrons and holes flow in opposite directions close to the junction: either electrons are swept into the n-layer, or holes are swept into the p-layer, depending on where the photoexcitation occurred.

1.2.3.2 Efficiency limits

Fig. 1.11 shows a typical construction of a Photovoltaic Cell. The thermodynamic efficiency of various devices is of wide interest because of the relevance of this parameter for energy conversion. The classic limiting efficiency for an ideal single-homojunction solar cell was analyzed by Shockley and Queisser and is about 31%[42]. The efficiency of a single-junction device is limited by transmission losses of photons with energies below the bandgap and thermal relaxation of carriers created by photons with energies above the

bandgap. In the classic case, every photon absorbed in a solar cell produces at most one electron–hole pair. Kodolinski et al. demonstrated an quantum efficiency higher than 100% in the short-wavelength range for a-Si solar cell[43]. This can be explained as an optically induced Auger mechanism: the energy in excess of the bandgap that one of the carriers receives from a high-energy photon is used in a second electron–hole generation. This result has led to the revision of the Shockley–Queisser model of the ideal solar cell, widely accepted as the physical limit of PV conversion.

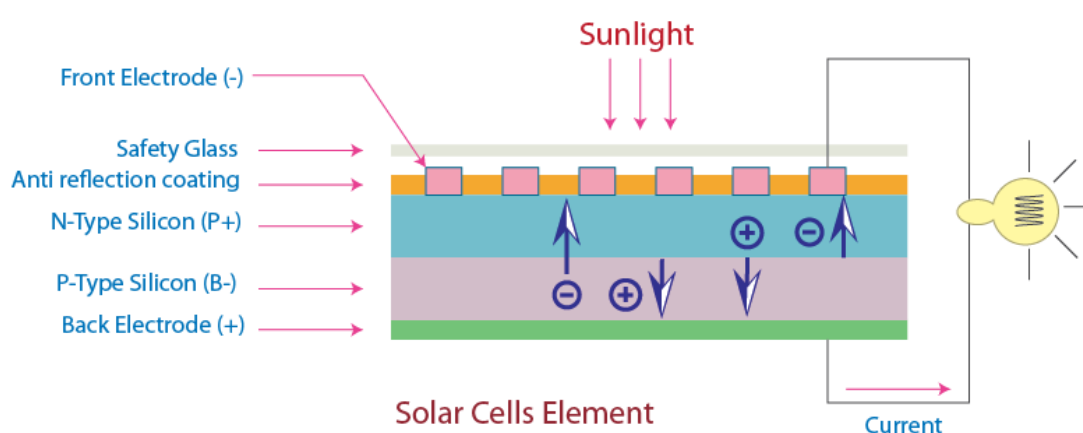


Fig. 1.11 Structure of photovoltaic solar cell

Fig. 1.12 gives an estimate of achievable cost with c-Si technology and comparison with projected achievable costs with other PV technologies[44]. It is generally agreed that c-Si wafer technology would not be able to meet the low-cost targets, whereas thin-film technologies have the potential to provide a viable alternative in the near future. The so-called “third-generation PV” will be based on nanostructures.

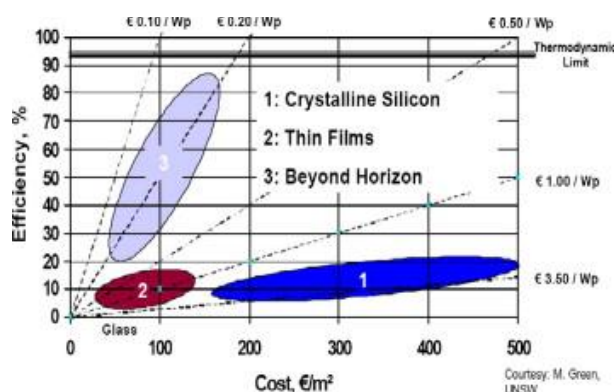


Fig. 1.12 Cost-efficiency analysis for (1) first-generation, (2) second-generation and (3) third generation photovoltaic technologies

1.2.3.3 Classification and development of solar cells

There were lots of kinds of solar cells with different materials and structures in the developing history in order to improve the thermodynamic efficiency including several leading types, such as c-Si, pc-Si, and amorphous-Si (a-Si), and III–V, II–VI, and I–III–VI₂ semiconductors and their alloys and nano-PV as shown in Fig. 1.13.

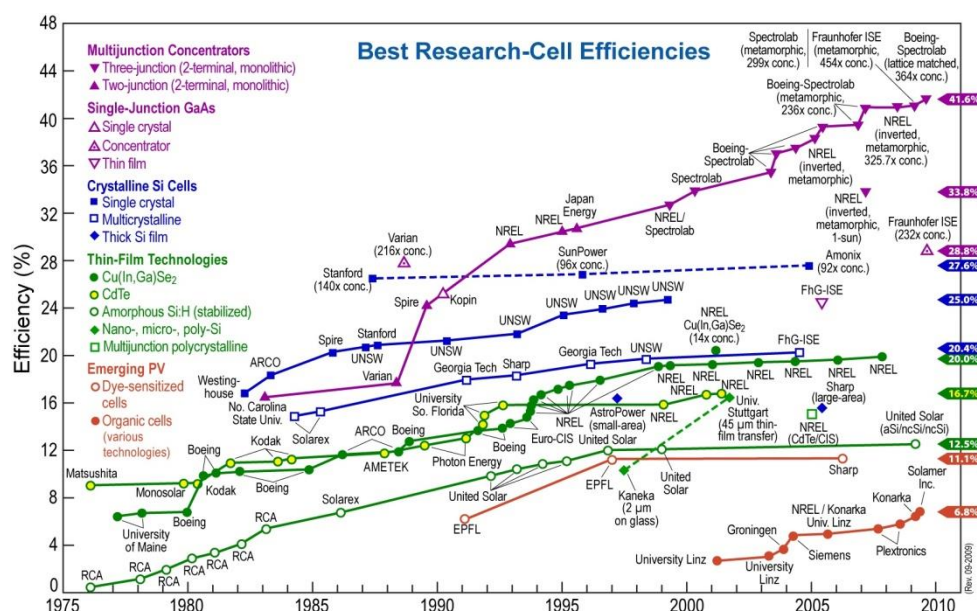


Fig. 1.13 Record efficiencies for different types of solar cells in the laboratory

Crystalline silicon is the first generation PV cell made from silicon. Single crystalline silicon is also called monosilicon[45, 46] while the polycrystalline silicon is called polysilicon[47, 48]. Monosilicon has higher efficiency and also higher cost. Commercial monosilicon cell efficiency approximates 22% as produced by US and Japanese solar manufacturers. For 80 μm thick Si cells, the devices have theoretical limiting efficiency of 29% and can achieve an energy payback period of 1-2 years. Commercial pc-Si cells have efficiencies of 12–15%.

The second generation PV cell applies monosilicon, polycrystalline, amorphous and nanocrystalline silicon (black silicon on glass) to a plastic or metal surface by chemical vapor deposition[49-52]. Thin film silicon is opposed to wafer silicon (also called bulk or crystalline silicon). Thin-film Si solar cells have the following important advantages compared to crystalline cells: (i) The thickness of Si can be drastically reduced to 50 μm ; (ii) Thin films can be deposited on low-cost substrates; (iii) Thin films can be fabricated on module-sized substrates and in integrally interconnected structures. According to some calculations, the thickness of Si films can be reduced down to 1 μm . [49] Overall thin film solar cells have lower efficiency and are less expensive than crystalline silicon. Most thin film cells have an efficiency of 12-20%, prototype module efficiency of 7-13% and production module efficiency of 9%. State-of-the-art thin film cells can reach the efficiency of 10-16%, with the highest reported efficiency being 18%.

In the early 1960s, thin-film chalcogenide such as $\text{Cu}_x\text{S}-\text{CdS}$, $\text{Cu}_x\text{Se}-\text{CdSe}$, and $\text{Cu}_x\text{Te}-\text{CdTe}$ solar cells were developed[53, 54]. Among them, cadmium telluride (CdTe , II–VI solar cells) based thin-film solar cell modules currently represent one of the fastest-growing segments of commercial module production. Its bandgap width of ~ 1.45 eV is quite favorable for conversion of the solar spectrum into electricity with a single-junction solar cell. Its very high optical absorption (10^5 cm^{-1}) and p-type conductivity make it an ideal material for PV applications. During the 20+ years of research undertaken by the CdTe Group, much effort has been directed at producing CdTe structures that allow more light to penetrate the top layers of the device (the transparent conducting contacts and cadmium sulfide (CdS) layers) to achieve high efficiency. The most common CdTe thin-film solar cell structure comprises a p-type CdTe absorber layer and n-type CdS window layer forming a hetero-junction, which has an intermixed interface region. Current solar cell structures are based on the device shown

in Fig. 1.14. Over 10% efficiency was achieved for CdTe cells with the highest to-date efficiency being 16.5%[55].

Among I–III–VI₂ compounds, CIGS-based thin-film solar cell modules currently represent the highest-efficiency alternative for large-scale, commercial thin-film solar cells for the following reasons: (a) a very high optical absorption coefficient ($\approx 10^5 \text{ cm}^{-1}$) and consequently, a very thin layer (0.1–0.3 μm) is enough for solar cells; (b) the possibility to change the type of conductivity (p- or n-); (c) the formation of solid solutions (different bandgaps), allowing bandgap engineering and therefore the fabrication of high-efficiency thin-film solar cells. Its bandgap of 1 eV is rather low for solar cells, and it is usual to replace indium with an alloy of indium and gallium-Cu(In,Ga)Se₂ to increase the bandgap and hence the open-circuit voltage. The world-record efficiency of almost 20% (the highest value for thin-film cells) on a CIGS cell has already been achieved[56, 57]. In terms of large-scale terrestrial applications, this material has a disadvantage because indium and gallium are very limited on Earth. Recently, aluminium was used instead of gallium, and more than 17% efficiency was obtained for Cu(In,Al)Se₂ cell[58].

The CdTe and CIGS thin-film technologies (Fig. 1.14) have demonstrated excellent potential for cost-effective production of solar electricity. However, these technologies, especially CdTe, suffer from the perception of toxicity of the constituent element Cd, which is a stable compound in thin-film modules. Issues raised include the hazards associated with the materials used during processing and fabrication of CdTe/CdS and CdS/CIGS solar cells and risks associated during the cradle-to-grave operating lifetime of these modules.

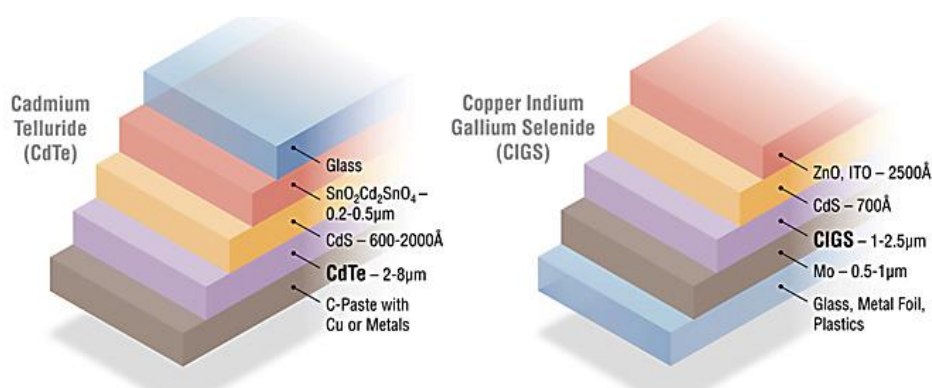


Fig. 1.14 Schematic illustration of a typical CdTe superstrate thin-film and CIGS substrate thin-film PV device

Meanwhile, other types of solar cells such as III–V single- and multi-junction solar cells (GaAs single-junction solar cells and InGaP/InGaAs/Ge triple-junction concentrator solar cell) [59, 60], Quantum well solar cells [61, 62], Quantum dot solar cells [63, 64], Dye-sensitized solar cells [65, 66] and Organic solar cells [67, 68] have also been extensively studied and have made great progress.

Further research and development will be directed toward increasing the efficiency of thin-film CIGS, CdTe, and Si as well as multi-junction III–V cells and nano-PV devices. And at the same time, emphasis should be put on developing cost-effective manufacturing technologies.

1.3 Thermoelectric (TE) conversion

The development of high efficiency thermoelectric materials is one of the important research directions for solar power utilization. In the daily life, there are lots of natural temperature differences and also much heat energy generated by costing energy, but eventually abandoned such as automobile exhaust and gas emissions of factory boilers, etc. The worldwide energy consumption reached 15 TW in 2008 and is projected to be about 30 TW by 2050 due to the growing global production and population. Among them, no less than 50 % of the energy was lost as heat. Electricity is the most widely used form of energy presently and the consumption of conventional energy sources based on oil, coal, and natural gas are playing lead role to meet the energy demand. Thermoelectric (TE) effect is a very interesting technology to re-use the lost heat for generating electricity.

Thermoelectric materials are materials which can provide the direct conversion of applied temperature gradient into electricity or electricity into temperature difference. A thermoelectric device can create voltage when there is a temperature difference on each side. Conversely, using an applied voltage, it creates a temperature difference. Indeed, many common materials, including metals and semiconductors, have a certain thermoelectric effect. At the atomic scale, an applied temperature gradient promotes charge carriers diffusion in the material from the hot side to the cold side.

Thermoelectricity has been investigated for about two hundred years since Seebeck effect and Peltier effect were discovered by Thomas Johann Seebeck [69] and Jean Charles Athanase Peltier [70] respectively. By the 1950's, A. F. Ioffe and his colleagues had developed the theory of thermoelectric conversion using the concept of figure of merit ZT [71, 72]. This formed the basis of all modern thermoelectric theory and accelerated a wide research focused on developing materials with high ZT in 1950s and 1960s. However, thermoelectric have long been too inefficient to be cost-effective in most applications [73].

In early 1990s, the development of "phonon-glass electron-crystal" (PGEC) concept by G. Slack led to a better understanding of the mechanism [74]. In a good thermoelectric material, the phonons should be disrupted like in a glass but the electrons should have high mobility like they do in crystalline semiconductors. Since mid-1990s, the need of new renewable energy sources has driven a resurgence of interest when theoretical predictions suggested that thermoelectric efficiency could be greatly enhanced through nano-structural engineering. This led to experimental efforts to demonstrate the proof-of-principle and high-efficiency materials [75-79]. At the same time, complex bulk materials (such as skutterudites [80], clathrates [81], and Zintl phases [82]) have been explored and found. All of these developments make it possible to obtain TE materials with high efficiencies [83]. The reliability and simplicity of thermoelectricity enable niche applications for this solid-state technology without moving parts even though conventional processes for electricity generation can be more efficient.

Thermoelectric material can be applied in a variety of applications [84]. The best known is thermocouple for temperature measurement [85]. The need for reliable and remote power sources provides some niche applications for thermoelectric power generation based on Seebeck effect. A typical application is radioisotope thermoelectric generators [86] which can provide electric power for spacecraft and satellites. Besides, thermoelectric devices could also convert waste heat [87] from thermal power plant and automobile into useful electricity. Moreover, Peltier coolers based on thermoelectric materials, thanks to its lack of moving parts or circulating liquid, near-infinite life and invulnerability to potential leaks as well as its small size and flexible shape, have occupied a small but stable industry [88].

1.3.1 Basic thermoelectric principle

1.3.1.1 Thermoelectric effect

The thermoelectric effect is a kind of direct conversion from temperature differences to electric voltage and vice versa. This effect can be used to generate electricity, measure temperature or change the temperature of objects. The term "thermoelectric effect" encompasses three separately identified effects: the Seebeck effect, Peltier effect and Thomson effect.

1.3.1.1.1 Seebeck effect

The Seebeck effect is the conversion of temperature differences directly into electricity and is named after German physicist T. J. Seebeck, who discovered this phenomenon in 1821[69].

Different metals (or semiconductors) have different free electron densities. When two different materials come into contact with each other, the electron diffusion will occur at the interface to eliminate electron density difference. Meanwhile, the electron diffusion rate is proportional to the temperature at interface. Therefore, as long as the temperature difference between the two materials is maintained, electron diffusion will continue by generating a stable voltage. This phenomenon is schematised in Fig. 1.15 with two different materials A and B.

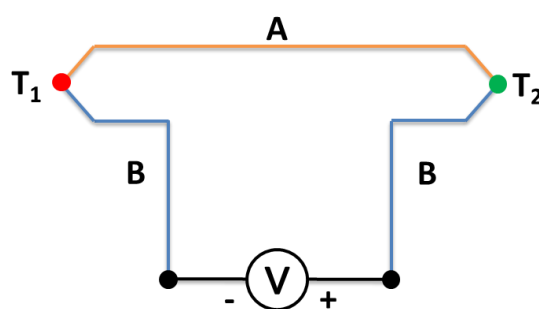


Fig. 1.15 Seebeck effect circuit

The voltage generated by the Seebeck effect can be expressed as:

$$V = \int_{T_1}^{T_2} (S_B(T) - S_A(T)) dT \quad (1.10)$$

where S_A and S_B are Seebeck coefficients (S), T_1 and T_2 are temperatures at interface. If the Seebeck coefficient in the experimental temperature range can be treated as constant, the above equation can be approximated as:

$$V = (S_B - S_A)(T_2 - T_1) \quad (1.11)$$

Actually, Seebeck coefficient depends largely on the temperature and the microstructure of the material. One way to define the Seebeck coefficient is to divide the voltage built up (ΔV) by the small temperature gradient applied to the material (ΔT):

$$S = -\Delta V / \Delta T \quad (1.12)$$

By analyzing the charge carrier mobility, it can be concluded that n-type semiconductors have negative Seebeck coefficient, which will be positive for p-type materials. Mixed n-type and p-type conduction in one material, if it exists, will lead to both charge carriers moving to the cold end, cancelling the induced Seebeck voltages.

Based on the Seebeck effect, many applications have been explored, such as thermocouple using metallic junctions and thermoelectric generator using semiconductor junctions.

1.3.1.1.2 Peltier effect

Peltier effect is named after the French physicist Jean-Charles Peltier, who made the discovery in 1834[89]. This effect is the presence of the heating at one electrified junction and the cooling at the other when electric current is maintained in a circuit of material consisting of two dissimilar conductors (Fig. 1.16). The effect is even stronger in circuits containing dissimilar semiconductors. If the current is reversed, heat generated by current flowing in one direction is absorbed. This effect can be explained from carrier energies.

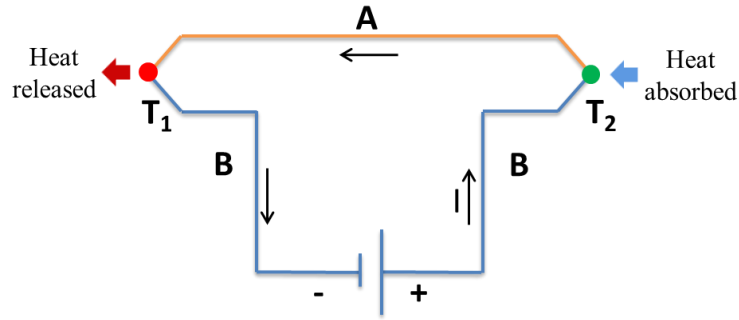


Fig. 1.16 Peltier effect circuit

Electron conductors are analyzed as an example. For a metallic junction, the energy levels of electrons in different metals are different. In Fig. 1.16, if the electron energy level in metal A is lower than in metal B, due to the existence of electric potential in a circuit, the electrons are pulled out from metal A to metal B at the green point. At this upper junction, the kinetic energy of electron will be converted to potential energy and electrons will move more slowly. Since the temperature is just a representation of the average speed of the random movements of the particles, the temperature at the upper junction will decrease. On the contrary, potential energy will be converted to kinetic energy at the lower junction (red point) by releasing heat.

Similar to metallic conjunction, the directional movement of charge carriers can generate thermal effects (endothermic or exothermic phenomenon) at the interface. In Fig. 1.16, the Peltier heat generated per unit time Q at the junction of conductor A and B (red point) is equal to,

$$Q = (\Pi_A - \Pi_B) \times I \quad (1.13)$$

where Π_A (Π_B) is Peltier coefficient of conductor A (B) and I is electric current from A to B.

Due to Peltier effect, the TE conjunctions can be used in applications ranging from travel coolers/warmers to laboratory instruments and communications systems. By cascading or pyramiding Peltier devices, quite large temperature differences can be generated.

1.3.1.1.3 Thomson effect

The Thomson effect was predicted and subsequently observed by W. Thomson in 1854. It describes the heating or cooling of a current-carrying conductor with a temperature gradient.

Any current-carrying conductor (except for a superconductor) with a temperature difference between two points either absorbs or emits heat, depending on the material. If a current density J passes through a homogeneous conductor, the heat production Q per unit volume is:

$$Q = \rho J^2 - \mu J \frac{dT(x)}{dx} \quad (1.14)$$

where ρ is material resistivity; μ is Thomson coefficient; dT/dx is the temperature gradient along the wire; and the first item is Joule heating.

Compared with the other two thermoelectric effects, Thomson effect is directly measurable for any unique material. On the contrary, no direct method exists for determining absolute Seebeck or Peltier coefficients for one material.

1.3.1.1.4 Kelvin relations

Indeed, the three thermoelectric coefficients mentioned above are not independent of each other. In 1854, Lord Kelvin found relationships among them, implying that the Thomson, Peltier, and Seebeck effects are different manifestations of one effect (uniquely characterized by the Seebeck coefficient).

The first Kelvin relation is:

$$\mu = T dS/dT \quad (1.15)$$

and the second Kelvin relation is:

$$\Pi = S \times T \quad (1.16)$$

where T is the absolute temperature. This relation expresses a subtle and fundamental connection between S , Π , and μ .

1.3.2 Thermoelectric converters

A metallic conjunction, due to the intrinsic high thermal conductivity, cannot provide high S or Π thus cannot generate high conversion efficiency as a thermoelectric converter. Semiconductors with sufficient S (or Π) are good candidates.

The electrical conductivity of a material is due to the mobility of charge carriers therein. In semiconductors, these carriers are of two different types. If conduction is ensured mainly by electrons, the material is n-type. In the opposite case, when electrons are deficient, the conduction is provided by the holes, the material is p-type. By convention, the n-type materials have a negative S (or Π) and the p-type materials a positive one.

A thermoelectric module is composed of an array of heavily doped p-type and n-type semiconductor legs (Fig. 1.17). The legs are electrically connected by metal electrodes in series but thermally connected in parallel. Then the top and bottom of this array are affixed to ceramic substrates to provide electrical insulation and good thermal conductivity.

To examine how the heat transfer occurs, the charge carriers flowing property through one pair of p-type and n-type elements within the thermoelectric module was studied and shown in Fig. 1.17.

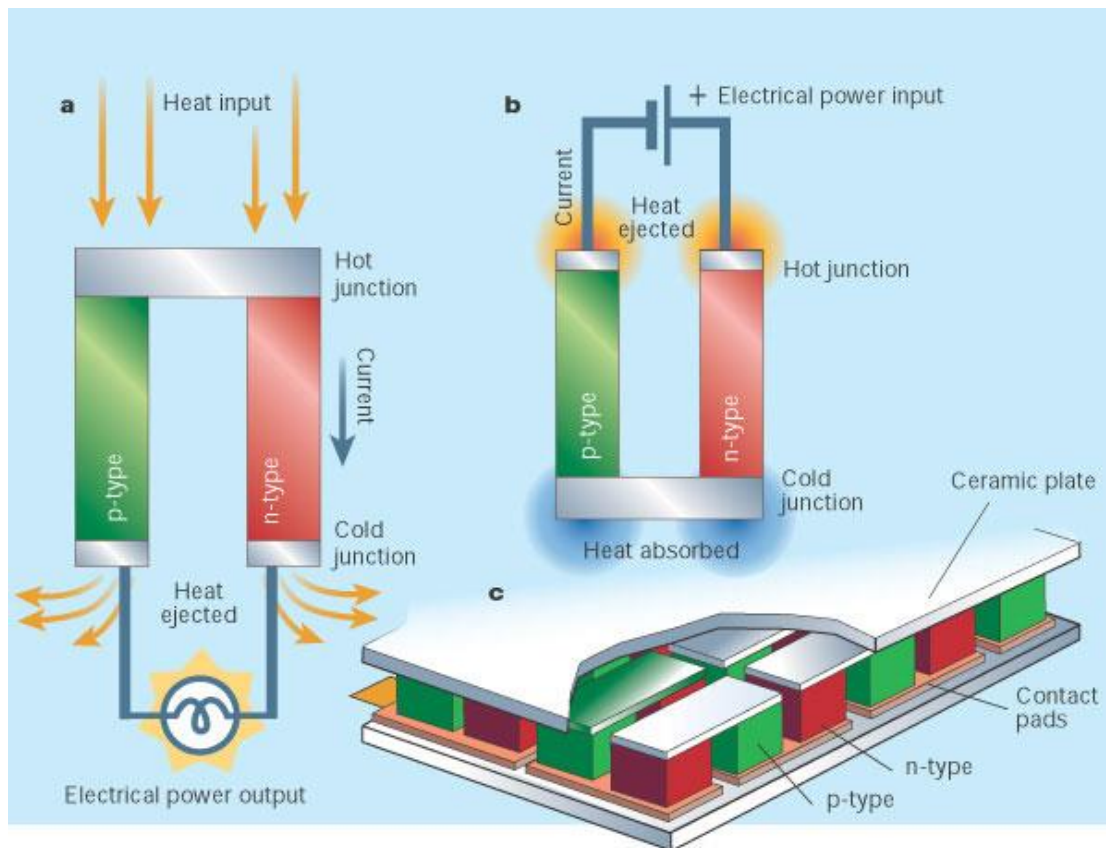


Fig. 1.17 Diagram of a thermoelectric module. a) Thermoelectric generator, b) Peltier cooler, c) Diagram of a typical thermoelectric converter

When a temperature difference is imposed across the thermoelectric device, thanks to the thermal diffusion of charge carriers, a difference in voltage will build up between the two sides based on Seebeck effect. This power source can provide power to the electrical circuits. Conversely, if a current is applied to the thermoelectric device, electrons will be forced out of p-type semiconductor, passing through the metal and into the n-type semiconductor. As electrons need to pass through the energy barriers, this is an endothermic process. As a result, a difference in temperature will build up between the two sides due to Peltier effect. If the current flow direction is opposite, the hot or cold face will be changed.

Actually, a thermoelectric generator can also be used as a Peltier cooler. However, a well-designed Peltier cooler will be a mediocre thermoelectric generator and vice-versa, due to different design and packaging requirements.

1.3.3 Material selection criteria

1.3.3.1 Power factor

S or Π is not the only coefficient that determines the usefulness of a material in a thermoelectric converter. Under a given temperature difference, the ability of one thermoelectric material producing useful electrical power is evaluated by its power factor PF ,

$$PF = S^2 \sigma \quad (1.17)$$

where S is the Seebeck coefficient, and σ is the electrical conductivity. One can see from this equation that S and σ of TE material should be as high as possible in order to obtain a high electrical power. However, many researches[90, 91] showed that S and σ are not independent because they have a close relationship with carrier concentration. Fig. 1.18 shows S , $\ln \sigma$, and $S^2 \sigma$ as a function of the carrier concentration. The highest power factors are obtained for semimetals or for heavily doped semiconductors. Therefore, a compromise between large S and σ of TE material should be chosen to maximize the power factor.

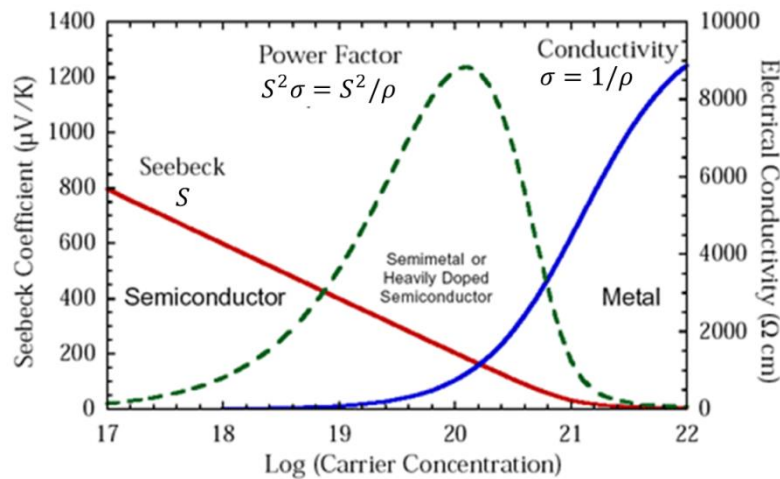


Fig. 1.18 S , σ , and $S^2 \sigma$ as a function of the logarithm of the carrier concentration[92, 93]

1.3.3.2 Figure of merit

Materials with high power factor are able to generate more energy in a space-constrained application, but they are not necessarily efficient. The optimization of a compound or material to efficiently produce thermoelectric power mainly implies the maximization of a dimensionless figure of merit ZT given by,

$$ZT = \frac{S^2 T \sigma}{\kappa_l + \kappa_e} \quad (1.18)$$

where T is absolute temperature, σ is electrical conductivity, $(\kappa_l + \kappa_e)$ is thermal conductivity caused by phonon (κ_l) and electron (κ_e).

A potential material usable for applications in the field of thermoelectric must have the highest ZT value as possible. From Equation ((1.18), it is clear that a material with interesting thermoelectric properties must have together high Seebeck coefficient, electrical conductivity, and low thermal conductivity. As electrons which participate in electrical conduction also take part in the transfer of heat, it is understandable that the exploration of new TE material is a process of compromise and optimization.

As discussed above, the maximum ZT value can be typically found in semimetals or heavily doped semiconductors with a carrier concentration between 10^{19} and 10^{21} per cm^3 .

The thermoelectric device efficiency for electricity generation, η , is defined as the ratio of energy provided to the load and heat energy absorbed at hot junction. In an actual thermoelectric module using both p-type and n-type thermoelectric materials, the maximum efficiency η_{max} is defined as:

$$\eta_{max} = \frac{T_H - T_C}{T_H} \frac{\sqrt{1 + zT} - 1}{\sqrt{1 + zT} + \frac{T_C}{T_H}} \quad (1.19)$$

Here, T_H and T_C are temperatures at the hot and cold junctions respectively. Fig shows the calculated maximum thermoelectric efficiency. From both Eq. (1.19) and Fig. 1.19, we

can see that η_{max} depends on the ZT . A remarkable high value of efficiency could be obtained if the value of ZT is enhanced. When ZT approaches infinity, the η_{max} approaches the Carnot limit. However, up to now, no known TE materials have a ZT larger than 3[83]. Therefore, how to improve thermoelectric efficiency becomes the key issue in this research field.

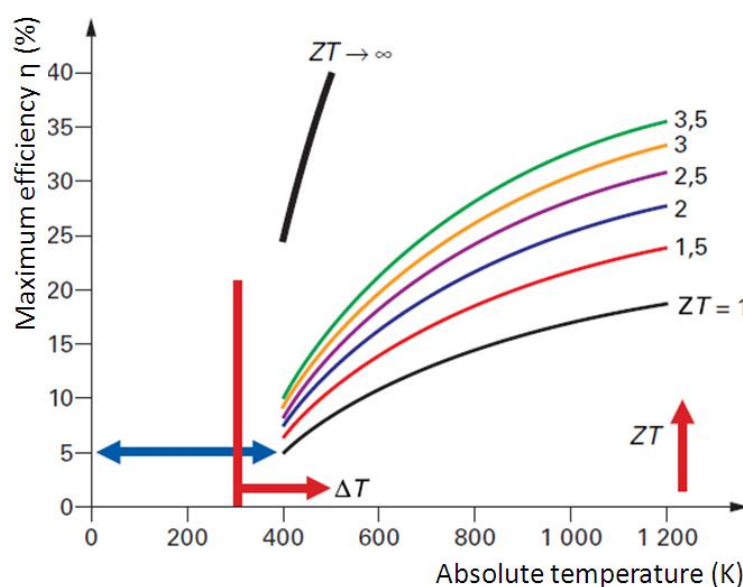


Fig. 1.19 Maximum thermoelectric device efficiency

1.4 Conclusions

With the speeding up of global industrialization, the world's energy shortage and exhaustion have become a problem that no one can ignore. Clean and renewable energy with no or minimum environment impact is attracting more and more attention, as it is the one of key issues for sustainable development.

Current annual global energy consumption is 4.1×10^{20} J (equivalent to 13 terawatts (TW)). By the end of this century, the projected population and economic growth will more than triple this global energy consumption. Fossil energy will be sooner or later exhausted. Solar energy is currently believed to be the most prominent renewable energy sources. Comparing with other energy resources such as exploitable hydroelectric resource (<0.5 TW),

the cumulative energy in all the tides and ocean currents in the world (<2 TW), or the globally extractable wind power (2-4 TW), solar energy provides about 120,000 TW striking the Earth, which can be exploited on the needed scale to meet global energy demand[94]. All routes for utilizing solar energy exploit the functional steps of capture, conversion, and storage.

In this situation, research on ways of harvesting solar energy including photothermal conversion, photovoltaic conversion, photochemical conversion and thermoelectric conversion attracts more and more attentions. Based on the analysis of the previous works, we propose to investigate the synthesis processes and the corresponding photoelectric and thermoelectric properties of the chalcogenide materials which have very interesting properties for energy conversion.

1.5 References

- [1] Pingwu Du and Richard Eisenberg, *Catalysts made of earth-abundant elements (Co, Ni, Fe) for water splitting: recent progress and future challenges*. Energy & Environmental Science, **5**(3) (2012) 6012-6021.
- [2] Arnulf Grübler and Sabine Messner, *Technological change and the timing of mitigation measures*. Energy economics, **20**(5) (1998) 495-512.
- [4] A Grübler, M Jefferson, A McDonald, S Messner, N Nakicenovic, HH Rogner and L Schrattenholzer, *Global Energy Perspectives to 2050 and Beyond*, World Energy Council (WEC). International Institute for Applied Systems Analysis (IIASA), (1995)
- [5] Peter Tertzakian, *A thousand barrels a second: The coming oil break point and the challenges facing an energy dependent world*. (2007)
- [7] Ibrahim Dincer, *Energy and environmental impacts: present and future perspectives*. Energy sources, **20**(4-5) (1998) 427-453.
- [8] REH Sims, *Renewable energy: a response to climate change*. Solar energy, **76**(1) (2004) 9-17.

- [9] Ralph EH Sims, *Bioenergy to mitigate for climate change and meet the needs of society, the economy and the environment*. Mitigation and Adaptation Strategies for Global Change, **8**(4) (2003) 349-370.
- [10] DO Hall, *Cooling the greenhouse with bioenergy*. Nature, **353**((1991) 11-12.
- [11] John Reilly, Ronald Prinn, Jochen Harnisch, Jean Fitzmaurice, Henry Jacoby, David Kicklighter, J Melillo, P Stone, A Sokolov and C Wang, *Multi-gas assessment of the Kyoto Protocol*. Nature, **401**(6753) (1999) 549-555.
- [12] A Demirbas, *Recent advances in biomass conversion technologies*. Energy Edu. Sci. Technol, **6** (2000) 19-40.
- [14] Wim C Turkenburg, Jos Beurskens, André Faaij, Peter Fraenkel, Ingvar Fridleifsson, Erik Lysen, David Mills, Jose Roberto Moreira, Lars J Nilsson and Anton Schaap, *Renewable energy technologies*. World Energy Assessment: Energy and the challenge of sustainability, (2000) 219-272.
- [15] Ibrahim Dincer, *Environmental issues: Ii-potential solutions*. Energy sources, **23**(1) (2001) 83-92.
- [16] Selcuk Bilgen, Kamil Kaygusuz and Ahmet Sari, *Renewable energy for a clean and sustainable future*. Energy sources, **26**(12) (2004) 1119-1129.
- [18] Ingvar B Fridleifsson, *Geothermal energy for the benefit of the people*. Renewable and sustainable energy reviews, **5**(3) (2001) 299-312.
- [19] RA Zakhidov, *Central Asian countries energy system and role of renewable energy sources*. Applied Solar Energy, **44**(3) (2008) 218-223.
- [20] Ariel Bergmann, Sergio Colombo and Nick Hanley, *Rural versus urban preferences for renewable energy developments*. Ecological economics, **65**(3) (2008) 616-625.
- [22] Stewart Taggart, *Hot stuff: CSP and the power tower*. renewable energy focus, **9**(3) (2008) 51-54.

- [24] Juan Carlos Colmenares and Rafael Luque, *Heterogeneous photocatalytic nanomaterials: prospects and challenges in selective transformations of biomass-derived compounds*. Chemical Society Reviews, **43**(3) (2014) 765-778.
- [25] K Butti and J Perlin, *The history of terrestrial uses of solar energy*. Solar Energy Handbook, McGraw-Hill, New York, (1981)
- [27] Takashi Hisatomi, Jun Kubota and Kazunari Domen, *Recent advances in semiconductors for photocatalytic and photoelectrochemical water splitting*. Chemical Society Reviews, **43**(22) (2014) 7520-7535.
- [28] Michael R Hoffmann, Scot T Martin, Wonyong Choi and Detlef W Bahnemann, *Environmental applications of semiconductor photocatalysis*. Chemical reviews, **95**(1) (1995) 69-96.
- [30] Akihiko Kudo and Yugo Miseki, *Heterogeneous photocatalyst materials for water splitting*. Chemical Society Reviews, **38**(1) (2009) 253-278.
- [31] Hiroshi Irie, Yuka Watanabe and Kazuhito Hashimoto, *Carbon-doped anatase TiO₂ powders as a visible-light sensitive photocatalyst*. Chemistry Letters, **32**(8) (2003) 772-773.
- [32] C Maneerat, Y Hayata, N Egashira, K Sakamoto, Z Hamai and M Kuroyanagi, *Photocatalytic reaction of TiO₂ to decompose ethylene in fruit and vegetable storage*. Transactions of the ASAE, **46**(3) (2003) 725.
- [33] Hiroshi Kominami, Jun-ichi Kato, Yoko Takada, Yoshiaki Doushi, Bunsho Ohtani, Sei-ichi Nishimoto, Masashi Inoue, Tomoyuki Inui and Yoshiya Kera, *Novel synthesis of microcrystalline titanium (IV) oxide having high thermal stability and ultra-high photocatalytic activity: thermal decomposition of titanium (IV) alkoxide in organic solvents*. Catalysis Letters, **46**(3-4) (1997) 235-240.
- [34] Hideki Kato, Mikihiro Hori, Ryoko Konta, Yoshiki Shimodaira and Akihiko Kudo, *Construction of Z-scheme type heterogeneous photocatalysis systems for water splitting into H₂ and O₂ under visible light irradiation*. Chemistry Letters, **33**(10) (2004) 1348-1349.

- [35] Akihiko Kudo, Hideki Kato and Issei Tsuji, *Strategies for the development of visible-light-driven photocatalysts for water splitting*. Chemistry Letters, **33**(12) (2004) 1534-1539.
- [36] Akira Fujishima, Xintong Zhang and Donald A Tryk, *Heterogeneous photocatalysis: from water photolysis to applications in environmental cleanup*. International journal of hydrogen energy, **32**(14) (2007) 2664-2672.
- [37] Heondo Jeong, Taehwan Kim, Dongsik Kim and Kweonill Kim, *Hydrogen production by the photocatalytic overall water splitting on NiO/Sr₃Ti₂O₇: effect of preparation method*. International journal of hydrogen energy, **31**(9) (2006) 1142-1146.
- [38] Akira Fujishima, *Electrochemical photolysis of water at a semiconductor electrode*. nature, **238**(5358) (1972) 37-38.
- [39] Allen J Bard, *Design of semiconductor photoelectrochemical systems for solar energy conversion*. The Journal of Physical Chemistry, **86**(2) (1982) 172-177.
- [40] Agatino Di Paola, Giuseppe Marci, Leonardo Palmisano, Mario Schiavello, Kohei Uosaki, Shigeru Ikeda and Bunsho Ohtani, *Preparation of polycrystalline TiO₂ photocatalysts impregnated with various transition metal ions: characterization and photocatalytic activity for the degradation of 4-nitrophenol*. The Journal of Physical Chemistry B, **106**(3) (2002) 637-645.
- [41] Yiming Xu and Cooper H Langford, *A Comparison of Acetophenone Photooxidation in Aqueous Media Via Direct Photolysis and TiO₂ Photocatalysis*. Journal of Advanced Oxidation Technologies, **2**((1997) 408-414.
- [42] William Shockley and Hans J Queisser, *Detailed balance limit of efficiency of p - n junction solar cells*. Journal of applied physics, **32**(3) (1961) 510-519.
- [43] Sabine Kolodinski, Jürgen H Werner, Thomas Wittchen and Hans J Queisser, *Quantum efficiencies exceeding unity due to impact ionization in silicon solar cells*. Applied Physics Letters, **63**(17) (1993) 2405-2407.

- [44] Martin A Green, *Third generation photovoltaics: solar cells for 2020 and beyond*. Physica E: Low-dimensional Systems and Nanostructures, **14**(1) (2002) 65-70.
- [45] W Wettling, *High efficiency silicon solar cells: State of the art and trends*. Solar energy materials and solar cells, **38**(1) (1995) 487-500.
- [47] John C Zolper, Srinivasamohan Narayanan, Stuart R Wenham and Martin A Green, *16.7% efficient, laser textured, buried contact polycrystalline silicon solar cell*. Applied Physics Letters, **55**(22) (1989) 2363-2365.
- [48] Y Inomata, K Fukui and K Shirasawa, *Surface texturing of large area multicrystalline silicon solar cells using reactive ion etching method*. Solar Energy Materials and Solar Cells, **48**(1) (1997) 237-242.
- [49] MA Green, J Zhao, A Wang and SR Wenham, *Progress and outlook for high-efficiency crystalline silicon solar cells*. Solar Energy Materials and Solar Cells, **65**(1) (2001) 9-16.
- [53] DA Cusano, *CdTe solar cells and photovoltaic heterojunctions in II-VI compounds*. Solid-State Electronics, **6**(3) (1963) 217-218.
- [54] J. Lebrun, *Realisation Et Proprietes Des Photopiles Solaires En Couches Minces De Tellurure De Cuivre Et Tellurure De Cadmium*. Revue De Physique Appliquee, **1**(3) (1966) 204-&.
- [56] Kannan Ramanathan, Miguel A Contreras, Craig L Perkins, Sally Asher, Falah S Hasoon, James Keane, David Young, Manuel Romero, Wyatt Metzger and Rommel Noufi, *Properties of 19.2% efficiency ZnO/CdS/CuInGaSe₂ thin -film solar cells*. Progress in Photovoltaics: Research and Applications, **11**(4) (2003) 225-230.
- [57] Ingrid Repins, Miguel A Contreras, Brian Egaas, Clay DeHart, John Scharf, Craig L Perkins, Bobby To and Rommel Noufi, *19.9% - efficient ZnO/CdS/CuInGaSe₂ solar cell with 81.2% fill factor*. Progress in Photovoltaics: Research and applications, **16**(3) (2008) 235-239.
- [58] Sylvain Marsillac, PD Paulson, MW Haimbodi, RW Birkmire and WN Shafarman, *High-efficiency solar cells based on Cu(InAl)Se₂ thin films*. Applied Physics Letters, **81**(7) (2002) 1350.

- [60] Masafumi Yamaguchi, Tatsuya Takamoto, Kenji Araki and Nicholas Ekins-Daukes, *Multi-junction III–V solar cells: current status and future potential*. Solar Energy, **79**(1) (2005) 78-85.
- [61] KWJ Barnham, I Ballard, JG Connolly, N Ekins-Daukes, BG Kluitinger, J Nelson, C Rohr and M Mazzer, *Recent results on quantum well solar cells*. Journal of Materials Science: Materials in Electronics, **11**(7) (2000) 531-536.
- [62] DE Ashenford, AW Dweydari, D Sands, CG Scott, M Housaf, E Aperathitis, Z Hatzopoulos and P Panayotatos, *Investigation of pin solar cell efficiency enhancement by use of MQW structures in the i-region*. Journal of crystal growth, **159**(1) (1996) 920-924.
- [64] A Martí N López, E Antolin, E C ánovas, C Stanley, Cuadra Farmer, L Cuadra and A Luque, *Novel semiconductor solar cell structures: The quantum dot intermediate band solar cell*. Thin Solid Films, **511**((2006) 638-644.
- [65] Elias Stathatos, Panagiotis Lianos, Vasko Jovanovski and Boris Orel, *Dye-sensitized photoelectrochemical solar cells based on nanocomposite organic–inorganic materials*. Journal of Photochemistry and Photobiology A: Chemistry, **169**(1) (2005) 57-61.
- [66] Michael Gr äzel, *Photoelectrochemical cells*. Nature, **414**(6861) (2001) 338-344.
- [67] Brian A Gregg, *The photoconversion mechanism of excitonic solar cells*. MRS bulletin, **30**(01) (2005) 20-22.
- [68] Afshin Hadipour, Bert de Boer and Paul WM Blom, *Organic tandem and multi - junction solar cells*. Advanced functional materials, **18**(2) (2008) 169-181.
- [69] Thomas Johann Seebeck, *Ueber die magnetische Polarisation der Metalle und Erze durch Temperaturdifferenz*. Annalen der Physik, **82**(3) (1826) 253-286.
- [70] JC Peltier, *Nouvelles experiences sur la caloricete des courans electriques*. Ann. Chem, **56**(1834) (1834) 371-387.
- [71] Abraham Fedorovich Ioffe, *Semiconductor thermoelements and thermoelectric cooling*. (1957)

- [74] Glen A Slack, *New materials and performance limits for thermoelectric cooling*. CRC Handbook of Thermoelectrics, **407** (1995)
- [75] M. S Dresselhaus, G. Chen, M. Y Tang, R. G Yang, H. Lee, D. Z Wang, Z. F Ren, J. P. Fleurial and P. Gogna, *New Directions for Low-Dimensional Thermoelectric Materials*. Advanced Materials, **19**(8) (2007) 1043-1053.
- [76] G. Chen, M. S. Dresselhaus, G. Dresselhaus, J. P. Fleurial and T. Caillat, *Recent developments in thermoelectric materials*. International Materials Reviews, **48**(1) (2003) 45-66.
- [80] G. S. Nolas, D. T. Morelli and Terry M. Tritt, *SKUTTERUDITES: A Phonon-Glass-Electron Crystal Approach to Advanced Thermoelectric Energy Conversion Applications*. Annual Review of Materials research, **29**(1999) 89-116.
- [81] Bo B. Iversen, Anders E. C. Palmqvist, David E. Cox, George S. Nolas, Galen D. Stucky, Nick P. Blake and Horia Metiu, *Why are Clathrates Good Candidates for Thermoelectric Materials?* Journal of Solid State Chemistry, **149**(2) (2000) 455-458.
- [82] Susan M. Kauzlarich, Shawna R. Brown and G. Jeffrey Snyder, *Zintl phases for thermoelectric devices*. Dalton Transactions, 21 (2007) 2099-2107.
- [83] Kanishka Biswas, Jiaqing He, Ivan D. Blum, Chun- I. Wu, Timothy P. Hogan, David N. Seidman, Vinayak P. Dravid and Mercouri G. Kanatzidis, *High-performance bulk thermoelectrics with all-scale hierarchical architectures*. Nature, **489**(7416) (2012) 414-418.
- [84] Saffa B Riffat and Xiaoli Ma, *Thermoelectrics: a review of present and potential applications*. Applied Thermal Engineering, **23**(8) (2003) 913-935.
- [86] Hongxia Xi, Lingai Luo and Gilles Fraisse, *Development and applications of solar-based thermoelectric technologies*. Renewable and Sustainable Energy Reviews, **11**(5) (2007) 923-936.
- [87] Lon E Bell, *Cooling, heating, generating power, and recovering waste heat with thermoelectric systems*. Science, **321**(5895) (2008) 1457-1461.

[90] Pinwen Zhu, Yoshio Imai, Yukihiro Isoda, Yoshikazi Shinohara, Xiaopeng Jia, Guozhong Ren and Guangtian Zou, *Electrical transport and thermoelectric properties of PbTe prepared by HPHT*. Materials transactions, **45**(11) (2004) 3102-3105.

[91] N Mateeva, H Niculescu, J Schlenoff and LR Testardi, *Correlation of Seebeck coefficient and electric conductivity in polyaniline and polypyrrole*. Journal of Applied Physics, **83**(6) (1998) 3111-3117.

[94] Nathan S Lewis and George Crabtree, *Basic research needs for solar energy utilization: report of the basic energy sciences workshop on solar energy utilization*, April 18-21, 2005.

Chapter II: Structure and photoelectric properties of $\text{Cu}_2\text{GeSe}_3\text{-Sb}_2\text{Se}_3$ ceramics

2.1 Introduction

Due to its promising characteristics such as direct and narrow band gap, high chemical stability, and high Seebeck coefficient ($1800 \mu\text{VK}^{-1}$), antimony selenide (Sb_2Se_3) is an interesting material for many potential applications, especially for photovoltaic devices and thermoelectric devices. However, research on the Sb_2Se_3 materials has been limited by its low electrical conductivity of $10^{-6} \Omega^{-1} \cdot \text{cm}^{-1}$ in bulk state[1-8]. This big issue for charge transport can be addressed by using it in combination with the Cu_2GeSe_3 phase having a relatively high conductivity of $10^1 \Omega^{-1} \cdot \text{cm}^{-1}$ [9]. The structure of Sb_2Se_3 is orthorhombic with cell parameters $a=1.113 \text{ nm}$, $b=1.142 \text{ nm}$ and $c=0.385 \text{ nm}$. It grows typically as rod-like crystals which can be easily interconnected. This is an important feature for building up an interconnected network[10]. The structure of Cu_2GeSe_3 seems more diversified as cubic ($a=0.555 \text{ nm}$), tetragonal ($a=0.560 \text{ nm}$, $b=0.548 \text{ nm}$) and orthorhombic ($a=1.186 \text{ nm}$, $b=0.396 \text{ nm}$ and $c=0.546 \text{ nm}$) phases are all reported[11, 12].

Previous research in our laboratory has demonstrated a $\text{GeSe}_2\text{-Sb}_2\text{Se}_3\text{-CuI}$ chalcogenide glass which can create an inorganic heterojunction structure within the materials by controlling the crystallization of the glass. The unique structure formed by Sb_2Se_3 and Cu_2GeSe_3 is the origin of interesting photoelectric properties[13, 14]. The enhanced charge separation and transfer were attributed to the $\text{Sb}_2\text{Se}_3\text{-Cu}_2\text{GeSe}_3$ p-n heterojunction network with high photocurrent, prepared by crystallizing the precursor glass $40\text{Sb}_2\text{Se}_3\text{-}40\text{GeSe}_2\text{-}20\text{CuI}$ (Fig. 2.1)[14]. It can be observed that the glass ceramic containing the Sb_2Se_3 and Cu_2GeSe_3 crystals demonstrates a much higher photocurrent than the two phases separately. This result shows the importance of the nanostructure of the glass ceramics. In this work, we present an original technique for preparing directly ceramics with the two semiconductors, Sb_2Se_3 and Cu_2GeSe_3 . The photoelectric properties of the $\text{Cu}_2\text{GeSe}_3\text{-Sb}_2\text{Se}_3$ ceramics will be studied in relationship with the microstructure.

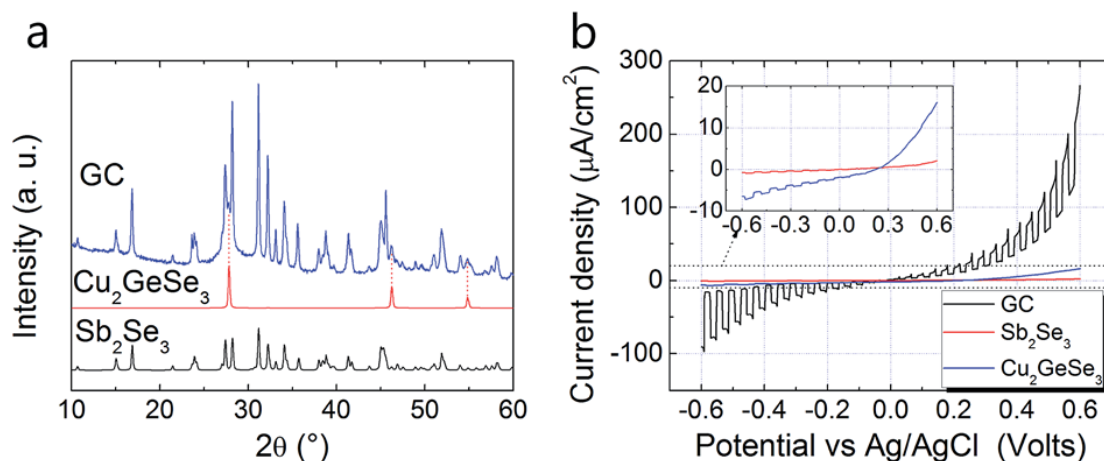


Fig. 2.1 Crystallized phases and photoelectric properties of the 40GeSe₂–40Sb₂Se₃–20CuI glass-ceramic

2.2 Experimental procedure

2.2.1 Preparation of Cu₂GeSe₃-Sb₂Se₃ ceramics

For chalcogenide ceramics synthesis, it is essential to operate in closed systems under inert atmosphere condition because of the high vapor pressure of chalcogenide melt and their tendency to react with oxygen, especially at high temperatures. Consequently, the ceramics have been produced by using the melt-quenching process with the corresponding element mixtures in sealed silica tube under vacuum. The schematic illustration of chalcogenide ceramics preparation process is shown in Fig. 2.2. This technique is widely used for chalcogenide glass preparation.

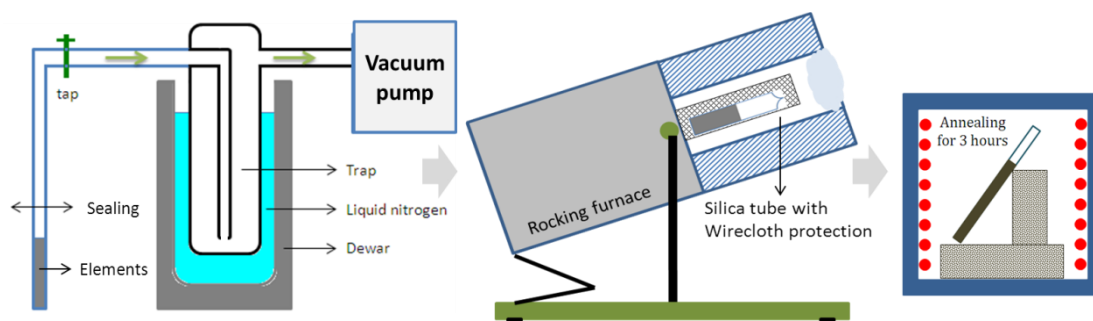


Fig. 2.2 Schematic diagram of chalcogenide ceramics preparation process

The ceramics were prepared using the Polycrystalline Germanium (99.999%), antimony (99.999%), Selenium (99.999%), Copper(99.9%) and/or CuI (98%) as starting materials. The preparation was done in a silica tube with 9 mm internal diameter. The tube was cleaned by hydrofluoric acid for one minute to eliminate dust presented on the wall. It was then thoroughly rinsed with deionized water and dried. A vacuum trap placed in liquid nitrogen is used to condense any volatile products and also to improve the vacuum. Appropriate quantities of each starting element/compound were weighed according to the composition and loaded into the silica tube which was then sealed under a typical vacuum of around 10^{-5} mbar. The tube containing the mixture was put into a rocking furnace. The typical thermal profile for the synthesis of $\text{Cu}_2\text{GeSe}_3\text{-Sb}_2\text{Se}_3$ ceramics is shown in Fig. 2.3. The silica tube containing all the starting materials was heated to 800 °C at the rate of 1.5 °C/min and hold for about 12 hours to ensure a thorough reaction and homogenization. Then the furnace was cooled down to 700 °C and the thermal quenching was performed by putting the sealed tube into water at room temperature. The rapid quenching is necessary to avoid excessive crystal growth, which could prevent the formation of the nano-scale heterojunction. At the same time, fast cooling can facilitate the separation of the rod from the silica tube. The thermal shock in the quenching process generated high mechanical stresses in the ceramics. In order to reduce these stresses, the ceramics were annealed at 200°C for 3 h. The ceramics are then cooled slowly and released from the silica tube. After the annealing, a ceramic rod of 9 cm was obtained and was sliced into discs with the thickness of about 2 mm before polishing for different measurements.

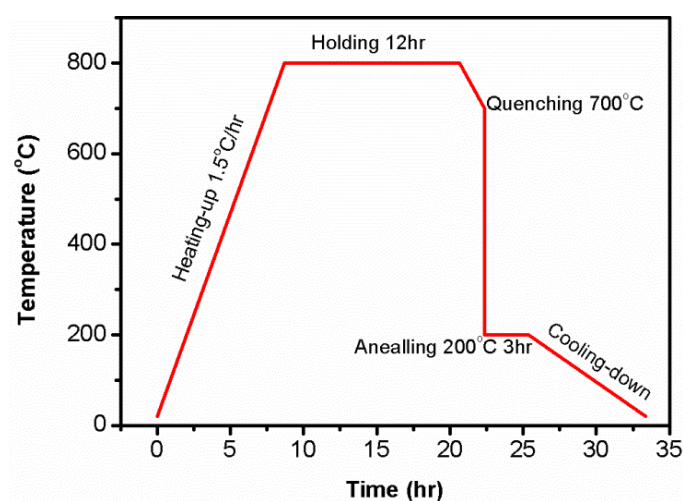


Fig. 2.3 Thermal profile for the preparation of $\text{Cu}_2\text{GeSe}_3\text{-Sb}_2\text{Se}_3$ ceramics

2.2.2 Presentation of characterization techniques

X-ray diffraction (XRD) analysis was carried out on a PANalytical's X-ray diffractometer with a step width of 0.02° and a counting duration of 0.13 s/step. Scanning electron microscope (SEM) images and Energy Dispersive Spectrometer (EDS) elemental mappings were obtained with a JEOL JSM-7100F Thermal field emission electron microscope equipped with an EDS system. Some of the characterization techniques are introduced in detail below.

2.2.2.2 X-ray diffraction (XRD) analysis

XRD analysis is based on constructive interference of monochromatic X-rays and a crystalline sample: The X-rays are generated by a cathode ray tube, filtered to produce monochromatic radiation, collimated to concentrate, and directed toward the sample. The interaction of the incident rays with the sample produces constructive interference (and a diffracted ray) when conditions satisfy Bragg's Law ($n\lambda=2d.\sin \theta$). This law relates the wavelength of electromagnetic radiation to the diffraction angle and the lattice spacing in a crystalline sample. The characteristic x-ray diffraction pattern generated in a typical XRD analysis provides a unique "fingerprint" of the crystals present in the sample. When properly interpreted, by comparison with standard reference patterns and measurements, this fingerprint allows identification of the crystalline phases.

2.2.2.3 Scanning electron microscope (SEM) images and Energy Dispersive Spectrometer (EDS) elemental mappings

Scanning electron microscope (SEM) images and energy dispersive spectrometer (EDS) elemental mappings were obtained with a JEOL JSM-7100F thermal field emission electron microscope equipped with an EDS system. The scanning electron microscope (SEM) uses a focused beam of high-energy electrons to generate a variety of signals at the surface of solid specimens. The signals that derive from electron-sample interactions reveal information about the sample including external morphology (texture), chemical composition, and crystalline structure and orientation of materials making up the sample. In most applications, data are

collected over a selected area of the surface of the sample, and a 2-dimensional image is generated that displays spatial variations in these properties. The SEM is also capable of performing analyses of selected point locations on the sample; this approach is especially useful in qualitatively and quantitatively determining chemical compositions (using EDS), crystalline structure, and crystal orientations (using diffracted backscattered electrons EBSD).

Accelerated electrons in an SEM carry significant amounts of kinetic energy, and this energy is dissipated as a variety of signals produced by electron-sample interactions when the incident electrons are decelerated in the solid sample. These signals include secondary electrons (that produce SEM images), backscattered electrons (BSE), diffracted backscattered electrons (EBSD that are used to determine crystal structures and orientations of minerals), photons (characteristic X-rays that are used for elemental analysis and continuum X-rays), visible light (cathodoluminescence–CL) and heat. Secondary electrons and backscattered electrons are commonly used for imaging samples: secondary electrons are most valuable for showing morphology and topography on samples and backscattered electrons are most useful for illustrating contrasts in composition in multiphase samples (i.e. for rapid phase discrimination). X-ray generation is produced by inelastic collisions of the incident electrons with electrons in discrete orbitals (shells) of atoms in the sample. As the excited electrons return to lower energy states, they yield X-rays that are of a fixed wavelength (that is related to the difference in energy levels of electrons in different shells for a given element). Thus, characteristic X-rays are produced for each element in a mineral that is "excited" by the electron beam. SEM analysis is considered to be "non-destructive"; that is, x-rays generated by electron interactions do not lead to volume loss of the sample, so it is possible to analyze the same materials repeatedly.

Energy dispersive x-ray analysis (EDX), referred to as EDS or EDAX, is an x-ray technique used to identify the elemental composition of materials. Applications include materials and product research, troubleshooting and more. EDX systems are attachments to electron microscopy instruments (Scanning Electron Microscopy (SEM) or Transmission Electron Microscopy (TEM)) where the imaging capability of the microscope identifies the specimen of interest. The data generated by EDX analysis consist of spectra showing peaks corresponding to the elements making up the true composition of the sample being analysed. Elemental mapping of a sample and image analysis are also possible.

2.2.2.4 Photo-electro-chemical (PEC) measurement

This measurement method is based on a PEC cell with generally an appropriate liquid electrolyte which should not be oxidized or reduced during the measurement. The principle of the measurement is the following: an electric bias is applied on the semiconductor which is illuminated with chopped light. The light will generate free charge carriers on the surface of the semiconductor in contact with the electrolyte and will consequently increase the current. The applied bias is generally scanned and the appearance or absence of photocurrent at positive or negative bias can be used for the determination of the type of the semiconductor. To characterize the photoelectric performance, the PEC measurement has been carried out by using the classic 3-electrode method with a chopped illumination of 400 W.m^{-2} from a broad band tungsten halogen lamp as shown in Fig. 2.4. The reference electrode is Ag/AgCl and the counter electrode is in platinum. The sample to be measured is used as the working electrode. The semiconducting ceramics studied here are always used as working electrodes. The working electrode has an ohmic electrical contact, created by connecting the back side (without illumination) with a copper wire with the help of conductive glue. Except the working surface of 9 mm in diameter, all edges and the backside electrical contact were sealed by a non-conducting resin as shown in Fig. 2.5. The advantage of the three-electrode method is that there is no current flow through the reference electrode to ensure the stability of the electrodes. Therefore, the measured potential is the applied bias, relative to the reference potential of Ag/AgCl, on the sample. The measurement consists of recording the current as function of the applied bias under chopped illumination to distinguish the dark and light current.

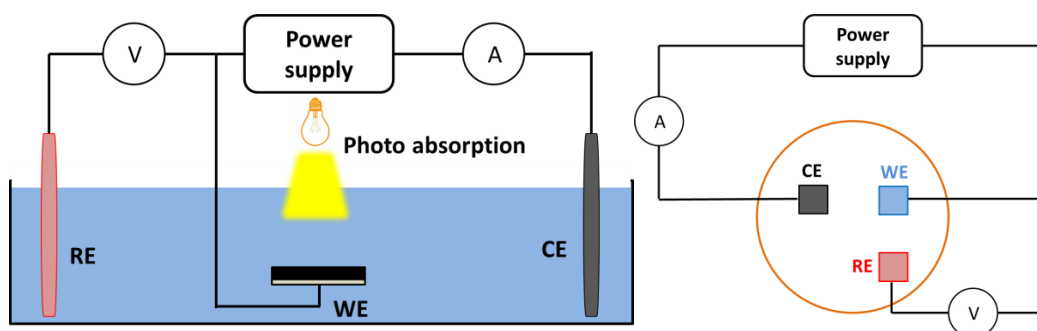


Fig. 2.4 Schematic presentation of three-electrode PEC method

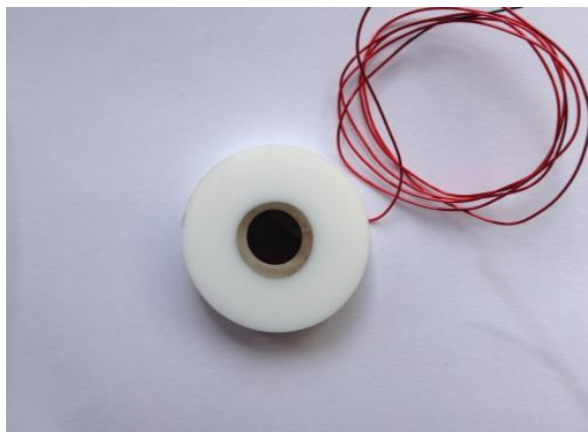


Fig. 2.5 Photograph of semiconductor working electrode

The major interest in semiconductor electrodes is due to the PEC properties of the semiconductor-electrolyte interface with the generation of additional currents following exposure to electromagnetic radiation such as solar energy. It is therefore important to describe what happens at the (idealized) interface between a semiconductor electrode and an electrolyte solution. In order for the two phases to be in equilibrium, their electrochemical potential must be the same. The electrochemical potential of the solution is determined by the redox potential of the electrolyte solution, and the redox potential of the semiconductor is determined by the Fermi level. If the redox potential of the solution and the Fermi level do not lie at the same energy, a movement of charge between the semiconductor and the solution is required in order to equilibrate the two phases. The excess charges moved to the semiconductor do not stay at the surface, as it would for a metallic electrode, but diffuse into the electrode for a significant distance ($100\text{-}10,000\text{ \AA}$). This region is referred to as the space charge region and has an associated electrical field. Therefore, there are two interface/zones to be considered: the electrode/electrolyte interface and the space charge zone.

For a p-type semiconductor, the Fermi layer is generally lower than the redox potential, and therefore electrons must transfer from the solution to the electrode to reach equilibrium. This generates a negative charge in the space charge region, which causes a downward bending in the band edges (Fig. 2.6(a)). Since the holes in the space charge region are

removed by this process, this region is again a depletion layer. For an n-type semiconductor electrode at open circuit, the Fermi level is typically higher than the redox potential of the electrolyte, and hence electrons will be transferred from the electrode into the solution. Therefore, there is a positive charge associated with the space charge region, and this is reflected in an upward bending of the band edges (Fig. 2.6(b)). Since the majority charge carrier of the semiconductor has been removed from this region, this region is also referred to as a depletion layer.

As for metallic electrodes, changing the potential applied to the electrode shifts the Fermi level. The band edges in the interior of the semiconductor (i.e., away from the depletion region) also vary with the applied potential in the same way as the Fermi level. However, the energies of the band edges at the interface are not affected by changes in the applied potential. Therefore, the change in the energies of the band edges on going from the interior of the semiconductor to the interface, and hence the magnitude and direction of band bending, vary with the applied potential. There are three different situations to be considered:

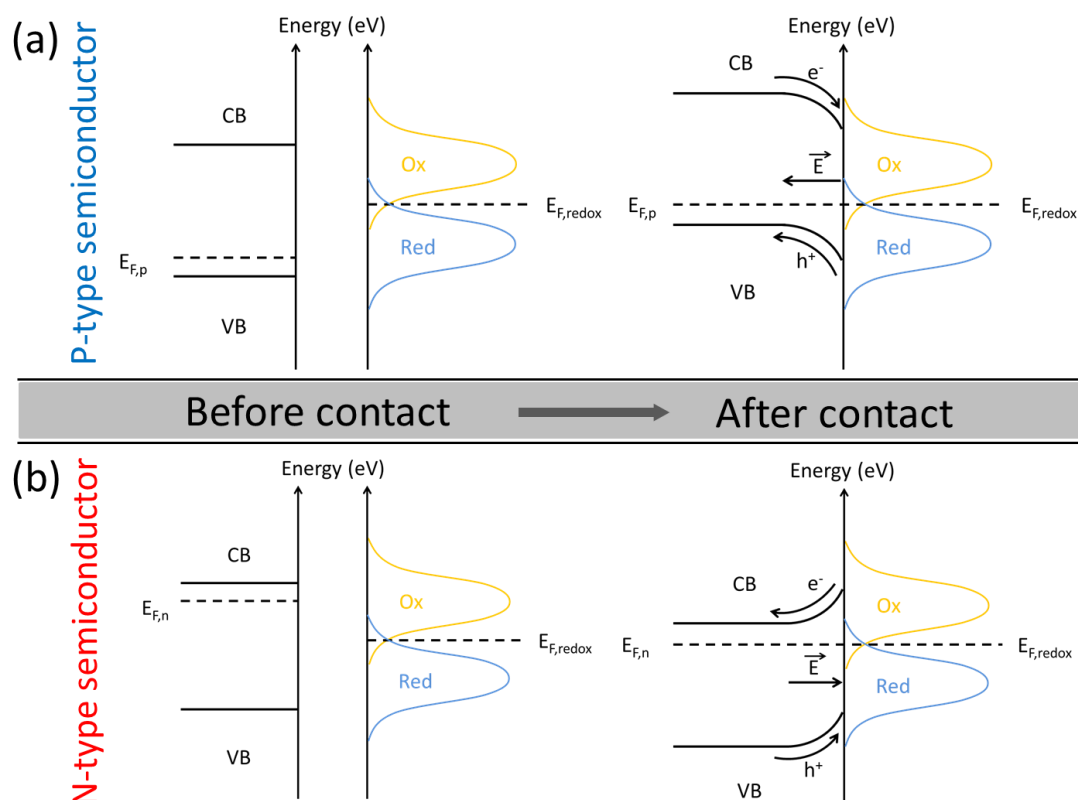


Fig. 2.6 Band bending for an n-type semiconductor and a p-type semiconductor in equilibrium with an electrolyte

At a certain potential, the Fermi energy lies at the same energy as the solution redox potential. In this case, there is no net transfer of charge, and hence there is no band bending. This potential is therefore referred to as the flat band potential.

Depletion regions arise at potentials negative of the flat band potential for a p-type semiconductor (Fig. 2.7(a)) and at potentials positive of the flat band potential for an n-type semiconductor (Fig. 2.7(d)).

At potentials negative of the flat band potential for an n-type semiconductor, there is now an excess of the majority charge carrier (electrons) in this space charge region, which is referred to as an accumulation region (Fig. 2.7(c)). An accumulation region arises in a p-type semiconductor at potentials more positive than the flat band potential (Fig. 2.7 (b)).

The charge transfer abilities of a semiconductor electrode depend on whether there is an accumulation layer or a depletion layer. If there is an accumulation layer, the behavior of a semiconductor electrode is similar to that of a metallic electrode, since there is an excess of the majority charge carrier available for charge transfer. In contrast, if there is a depletion layer, then there are few charge carriers available for charge transfer, and electron transfer reactions occur slowly.

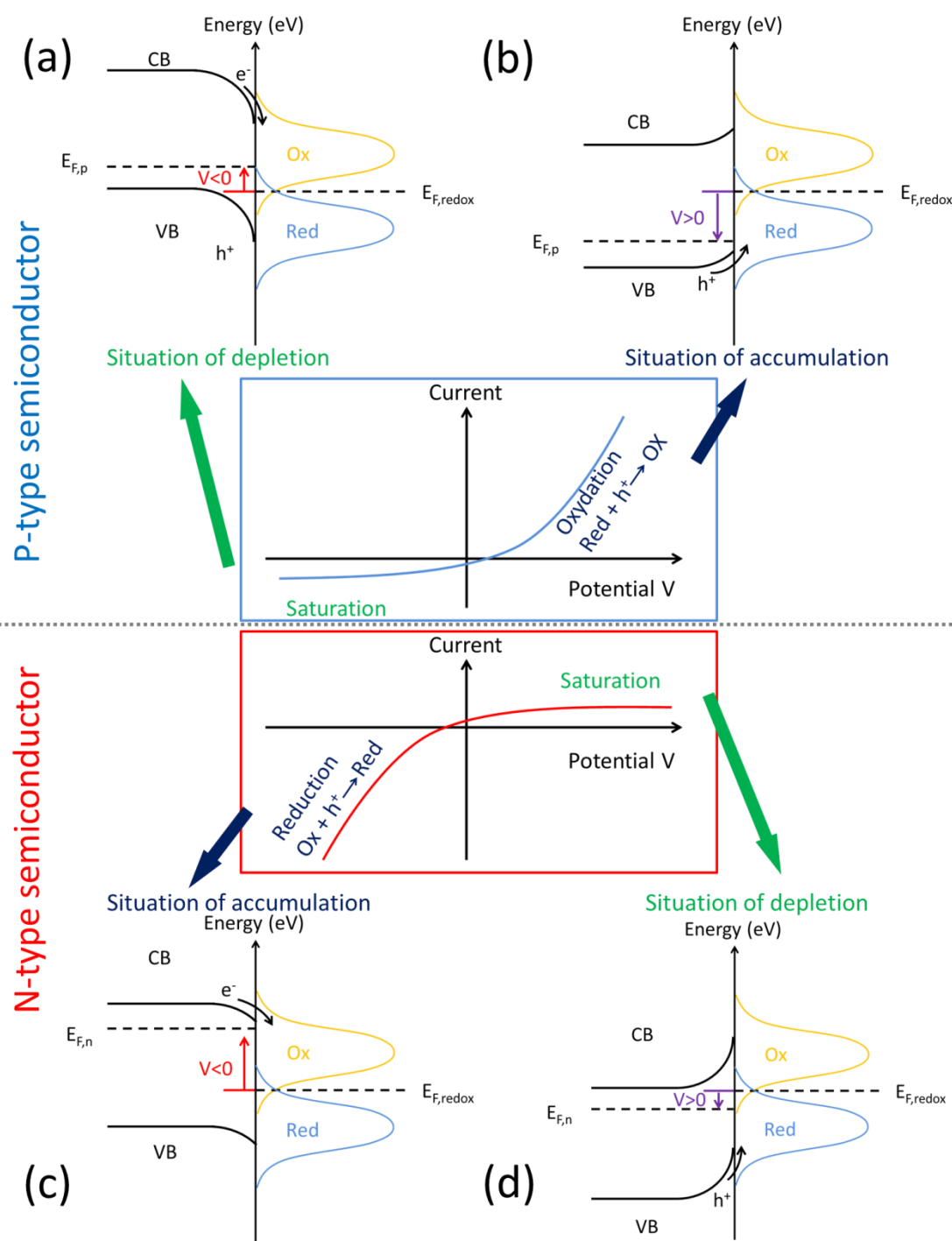


Fig. 2.7 Effect of varying the applied potential (E) on the band edges in the interior of an n-type and a p-type semiconductor

However, if the working electrode is exposed to radiation of sufficient energy, electrons can now be promoted to the conduction band. If this process occurs in the interior of the semiconductor, recombination of the promoted electron and the resulting hole typically occurs, together with the production of heat. However, if it occurs in the space charge region, the electric field in this region will facilitate the separation of the charges. For example, for an n-type semiconductor at positive potentials, the band edges curve upwards, and hence the holes move towards the interface, and the electron moves to the interior of the semiconductor. The hole is a high energy species that can extract an electron from the solution; that is, the n-type semiconductor electrode acts as a photoanode. Ideal behavior for an n-type semiconductor electrode in the dark and under irradiation is shown in Fig. 2.8. At the flat band potential, there is no current, either in the dark or upon irradiation (Region II), since there is no electric field to separate any generated charge carriers. At potentials negative of the flat band potential (Region I), an accumulation layer exists, and the electrode can act as a cathode, both in the dark and upon irradiation (the electrode is referred to as a dark cathode under these conditions). At potentials positive of the flat band potential (Region III), a depletion layer exists, so there can be no oxidative current in the dark. However, upon irradiation, a photocurrent can be observed since some of the energy required for the oxidation is provided by the radiation (via the high energy hole). Using similar reasoning, it can be shown that p-type semiconductor electrodes are dark anodes and photocathodes.

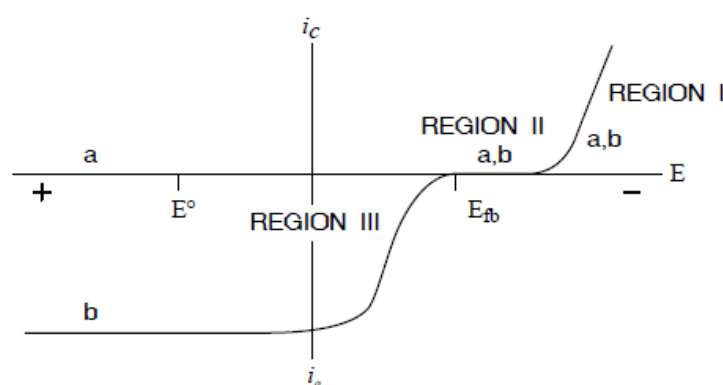


Fig. 2.8 Ideal behavior for an n-type semiconductor in the dark (a) and under irradiation (b)[15]

As a result, the PEC behavior for a p-type and an n-type semiconductor under a chopped illumination is shown in Fig. 2.9.

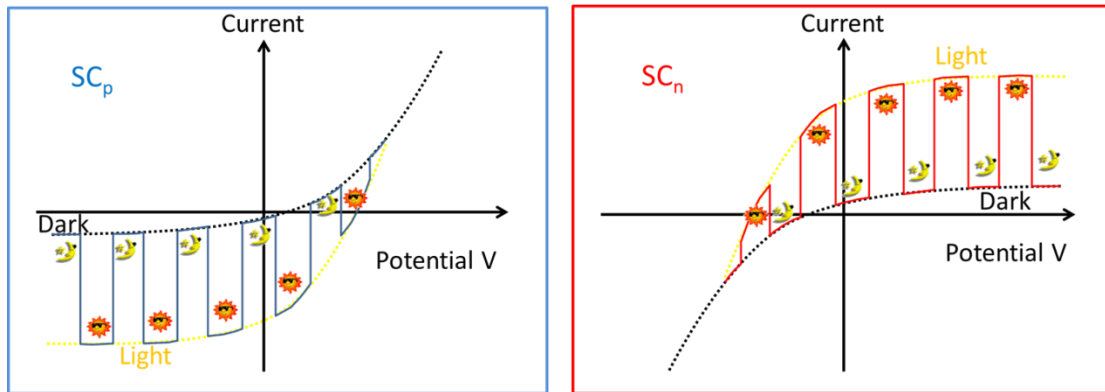


Fig. 2.9 Effect of illumination on PEC properties of an n-type and a p-type semiconductor

2.2.2.5 Electrical conductivity measurement

In our experiment, the electrical resistivity was measured by the method of four point probes, which is an easy method to test sheet electrical resistivity. As shown in Fig. 2.10, a current is passed through the outer probes and induces a voltage in the inner voltage probes.

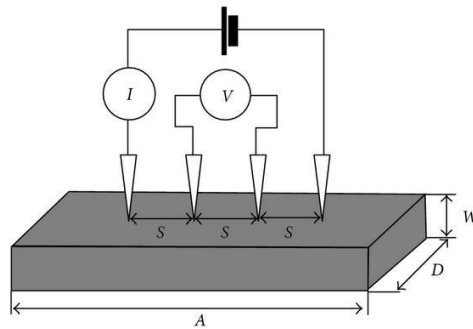


Fig. 2.10 Schematic presentation of the four-point probe method for electrical resistivity measurement

The bulk resistivity ρ can be measured using the voltage (V) and current (I) readings from the probe and sample thickness (w).

$$\rho[\Omega \cdot cm] = \frac{\pi}{\ln 2} w \frac{V}{I} = \frac{0.5324 V w}{I} \quad (2.1)$$

The above simple formula works when the wafer thickness is less than half the probe spacing ($t < s/2$). Conductivity σ is defined as the inverse of resistivity:

$$\sigma[S \cdot cm^{-1}] = \frac{1}{\rho} \quad (2.2)$$

2.2.2.6 The conductivity type measurement

The conductivity type of the as-prepared ceramics is measured with a Semilab PN tester PN-100 (Fig. 2.11). A semiconductor surface covered by a thin layer oxide is typically in depletion conditions regardless of its type. As a consequence the polarity of the surface barrier is characteristic of the conductivity type of the sample under test. Surface barrier polarity can be detected in a non-contact way by measuring the surface photovoltage. During such measurement, a chopped laser light is applied: by the high intensity illumination, excess carriers are generated and their presence decreases the surface barrier, i.e. flat band condition is approached. The barrier change due to the illumination is capacitively detected by a probe. Conductivity type is determined by the polarity of the surface barrier change due to illumination.

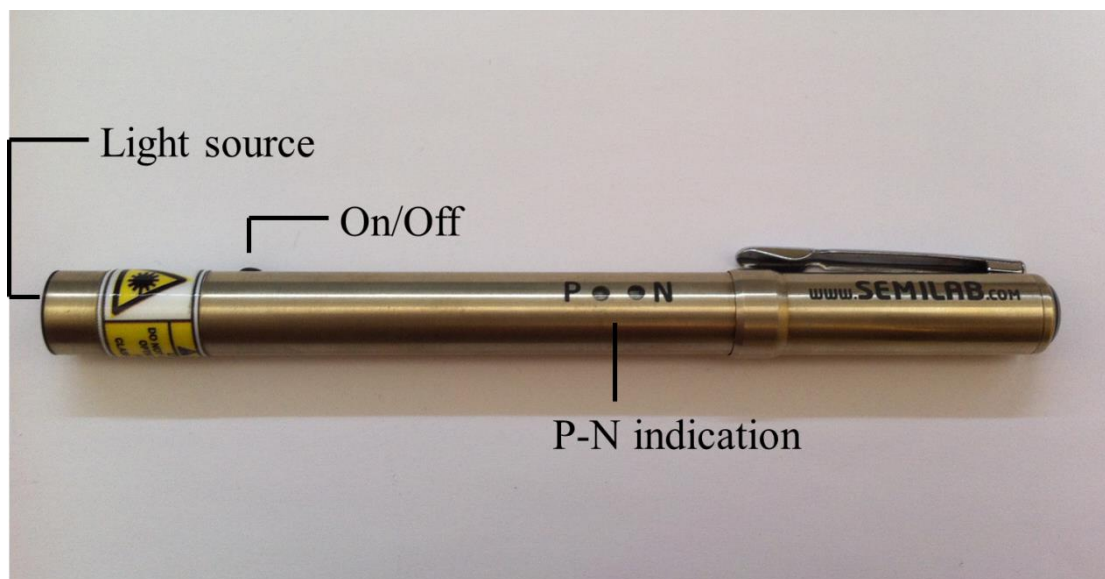


Fig. 2.11 Photograph of a Semilab PN tester

2.3 Results and discussion

2.3.1 Structure and photoelectric properties of the $x\text{Cu}_2\text{GeSe}_3-(100-x)\text{Sb}_2\text{Se}_3$ ($x=10, 20, \dots, 70$) ceramics

Fig. 2.12 shows the XRD patterns of the $x\text{Cu}_2\text{GeSe}_3-(100-x)\text{Sb}_2\text{Se}_3$ ($x=10, 20, \dots, 70$) ceramics. The diffraction peaks are in good agreement with the JCPDS standard card (JCPDS 65-2533) of the orthorhombic-phase Cu_2GeSe_3 and the card (JCPDS 15-0861) of the orthorhombic-phase Sb_2Se_3 . It can be seen that, different from the glass formation and then crystallization process before, the desired phases can be obtained directly without the generation of amorphous phases or other secondary phases[16]. In the meantime, the ratio of $\text{Cu}_2\text{GeSe}_3/\text{Sb}_2\text{Se}_3$ could also be controlled quantitatively by simply adjusting the proportion of the initial ingredients. The XRD results indicated that increasing $\text{Cu}_2\text{GeSe}_3/\text{Sb}_2\text{Se}_3$ ratio will only lead to the increase of the Cu_2GeSe_3 peaks intensity and the decrease of the Sb_2Se_3 peaks intensity, without the creation of any new crystalline phase.

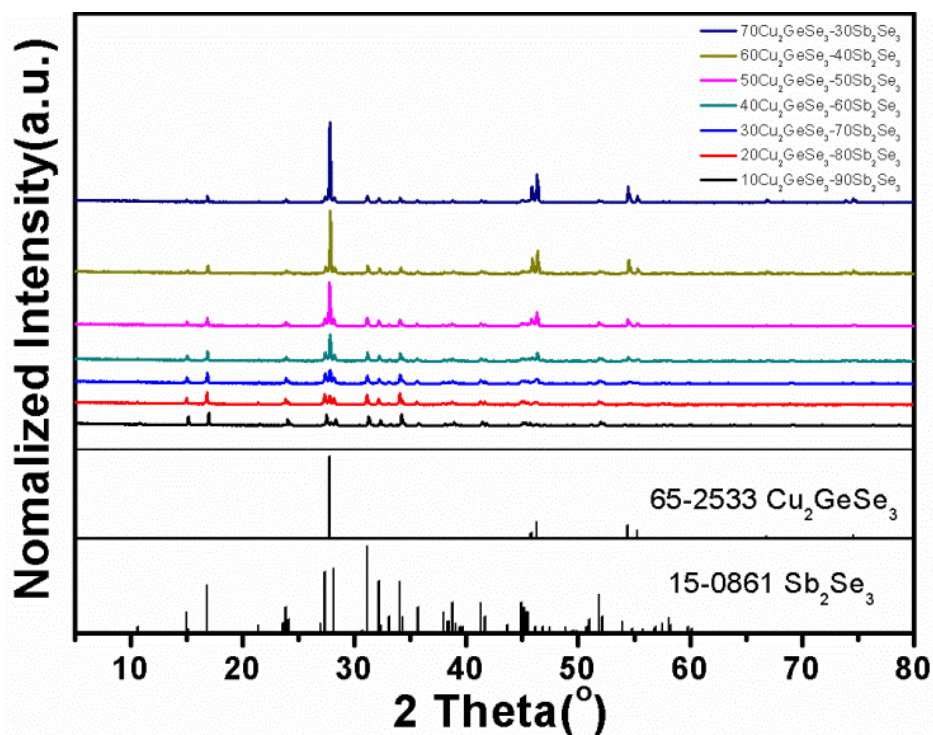


Fig. 2.12 XRD patterns of the $x\text{Cu}_2\text{GeSe}_3-(100-x)\text{Sb}_2\text{Se}_3$ ($x=10, 20, \dots, 70$) ceramics

The morphology of the cross section of the $x\text{Cu}_2\text{GeSe}_3-(100-x)\text{Sb}_2\text{Se}_3$ ($x=10, 20, \dots, 70$) ceramics is shown in Fig. 2.13. All the ceramics have a dense microstructure with low porosity and micron-scale particles appear in the samples. The contours of the crystals are clear and the characteristic clusters of crystals can be distinguished in the SEM images. As expected, with increasing Cu_2GeSe_3 or decreasing Sb_2Se_3 content, the rod-like crystals disappear progressively and the overall microstructure shows more and more symmetry.

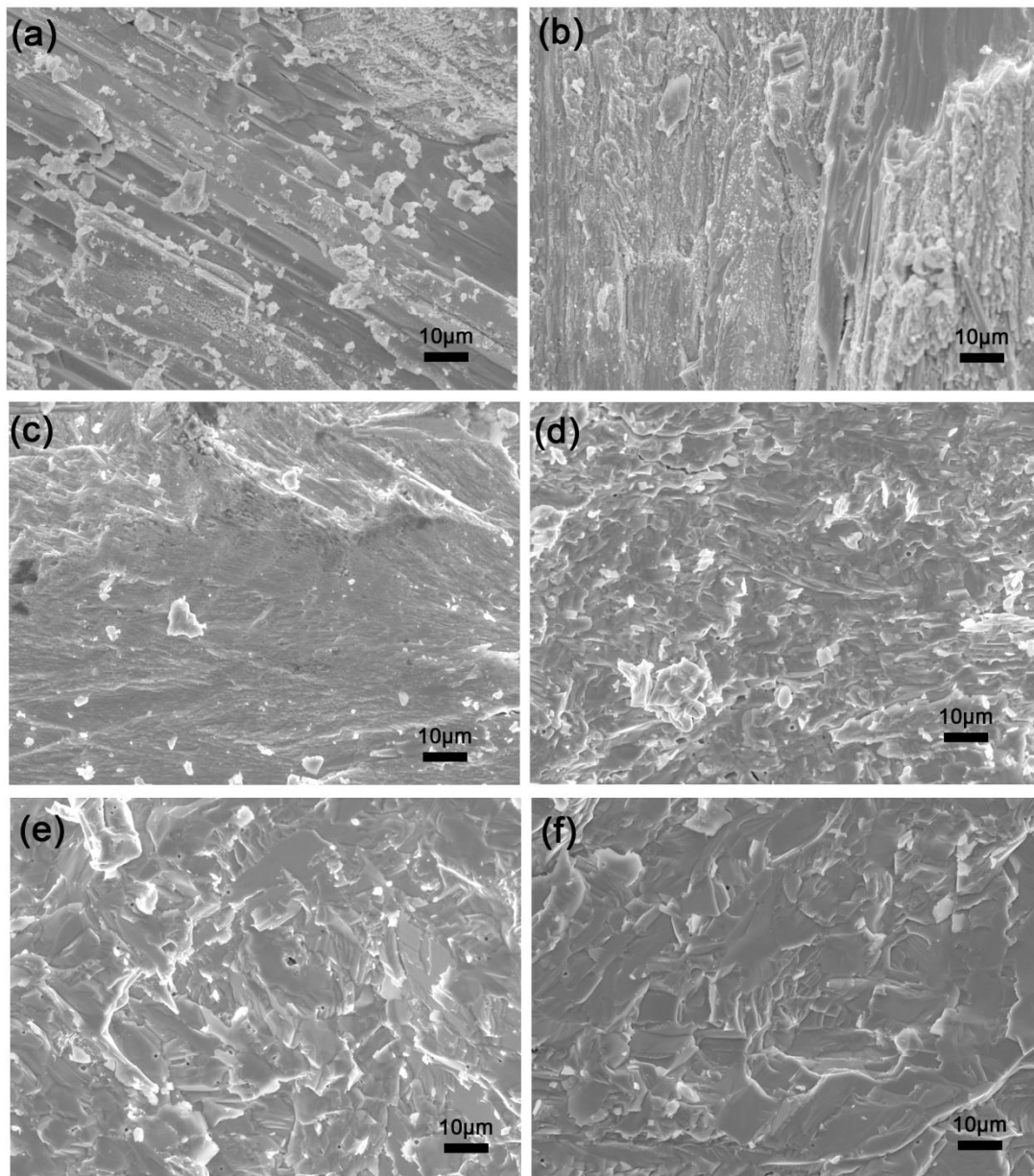


Fig. 2.13 SEM images of the cross section of the $x\text{Cu}_2\text{GeSe}_3-(100-x)\text{Sb}_2\text{Se}_3$ ($x=10, 20, \dots, 70$) ceramics: (a) $x=10$; (b) $x=20$; (c) $x=30$; (d) $x=40$; (e) $x=50$ and (f) $x=60$

Fig. 2.14 presents the photoelectric properties of the $x\text{Cu}_2\text{GeSe}_3-(100-x)\text{Sb}_2\text{Se}_3$ ($x=10, 20, \dots, 70$) ceramics, which shows a similar photocurrent intensity and variation. For all the ceramics, the I-V curve evidenced negative oscillations whose amplitude is enhanced as potentials become more negative under illumination. This phenomenon indicates that the photocurrent of these materials was sensitive to the concentration of negative charge which

was consequently the minority charge carrier. This is a clear signature of the p-type semiconductor [15, 17]. As observed earlier, the ceramics are composed of two kinds of relatively narrow direct bandgap semiconductors, 1.0-1.2 eV for Sb_2Se_3 and 0.78 eV for Cu_2GeSe_3 [18, 19]. Sb_2Se_3 is considered as a promising semiconductor for building heterojunctions to achieve high energy conversion efficiency due to the high absorption coefficient of 10^5 cm^{-1} [20]. But its high resistivity of $10^8 \Omega\cdot\text{m}$ is certainly a big issue for charge transport which can be achieved by the Cu_2GeSe_3 phase with a low resistivity of $10^{-1} \Omega\cdot\text{m}$ (Table 2.1), if these two phases are properly structured [21]. The photocurrent intensity depends on the photon absorption, the charge generation, the charge separation and the charge migration. Photons are efficiently and essentially absorbed by Sb_2Se_3 as well as by Cu_2GeSe_3 , and then the heterojunction formed by n-type Sb_2Se_3 and p-type Cu_2GeSe_3 enhances the charge separation and the charge is efficiently collected and transported to the back contact by the conductive channels throughout the bulk formed by the Cu_2GeSe_3 with relatively low resistivity.

Fig. 2.15 shows the SEM image of the $50\text{Cu}_2\text{GeSe}_3$ - $50\text{Sb}_2\text{Se}_3$ ceramic. A sandwich structured can be observed, which indicated that these two phases grow in parallel. The Cu_2GeSe_3 grew throughout the whole bulk even with only 10% of Cu_2GeSe_3 ($10\text{Cu}_2\text{GeSe}_3$ - $90\text{Sb}_2\text{Se}_3$) and the charge carriers can be transported without passing by the Sb_2Se_3 . Consequently, the photocurrent was determined only by the Cu_2GeSe_3 phase. Therefore, all the ceramics even with different $\text{Cu}_2\text{GeSe}_3/\text{Sb}_2\text{Se}_3$ ratios show a similar photocurrent intensity in the negative bias region, indicating a p-type semiconductor behavior. The conduction type of ceramics with different Cu_2GeSe_3 - Sb_2Se_3 ratios is measured with the Semilab PN tester PN-100 and summarized in Table 2.1. It is clear that all the ceramics present a feature of P-type semiconductor and that Sb_2Se_3 phase does not take part in the photoconduction process

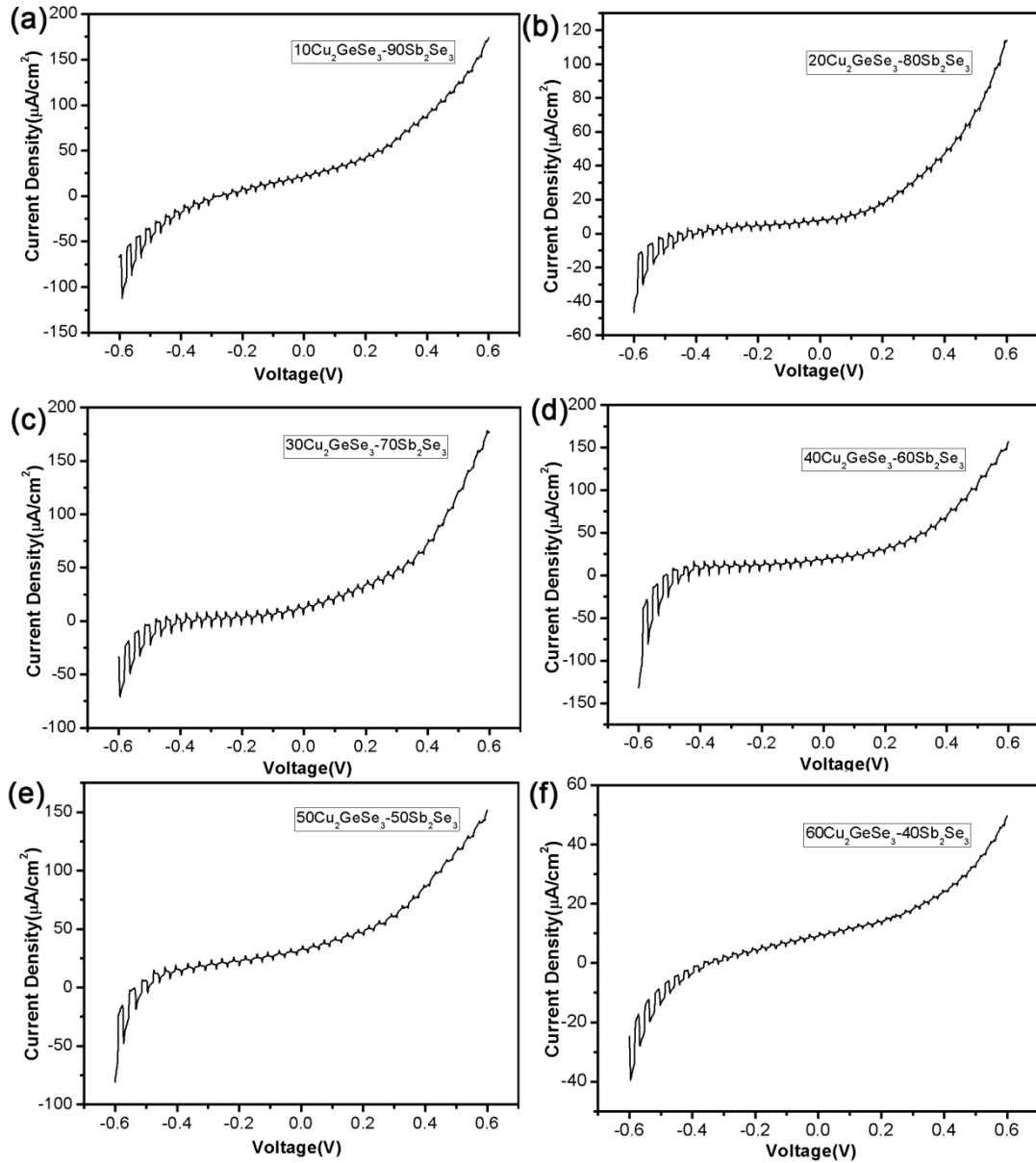


Fig. 2.14 Current-voltage characteristic of the $x\text{Cu}_2\text{GeSe}_3-(100-x)\text{Sb}_2\text{Se}_3$ ($x=10, 20, \dots, 70$) ceramics under chopped illumination: (a) $x=10$; (b) $x=20$; (c) $x=30$; (d) $x=40$; (e) $x=50$ and (f) $x=60$

Table 2.1 Resistivity of the $x\text{Cu}_2\text{GeSe}_3-(100-x)\text{Sb}_2\text{Se}_3$ ($x=10, 20, \dots, 70$) ceramics measured by the four-point probe method and p/n type measured with a Semilab PN tester

Samples	GS7-3	GS6-4	GS5-5	GS4-6	GS3-7	GS2-8	GS1-9	Sb ₂ Se ₃	Cu ₂ GeSe ₃
Cu ₂ GeSe ₃ /Sb ₂ Se ₃	7/3	6/4	5/5	4/6	3/7	2/8	1/9	-	-
Resistivity/ $\Omega\cdot\text{m}$	1.56	12.20	14.65	2.39	1.60	2.78	18.84	3.25×10^8	0.12
Conduction type	P	P	P	P	P	P	P	N	P

Fig. 2.15 shows that the Cu₂GeSe₃ phase is interconnected. Thus the conductivity of Sb₂Se₃ is too low to play any significant role. Thanks to the Cu₂GeSe₃ phase, the resistivity value of the $x\text{Cu}_2\text{GeSe}_3-(100-x)\text{Sb}_2\text{Se}_3$ ($x=10, 20\dots, 70$) ceramics shifts towards pure Cu₂GeSe₃ crystal. All the ceramics have shown similar conductivities of in the range of 1.6~19 $\Omega\cdot\text{m}$, mainly determined by Cu₂GeSe₃ phase as indicated in table 2.1. It is interesting to note that there is not any direct relationship between the conductivity and the Cu₂GeSe₃ content. The microstructure or the relative arrangement of these two crystalline phases is the main parameter that determines the conductivity.

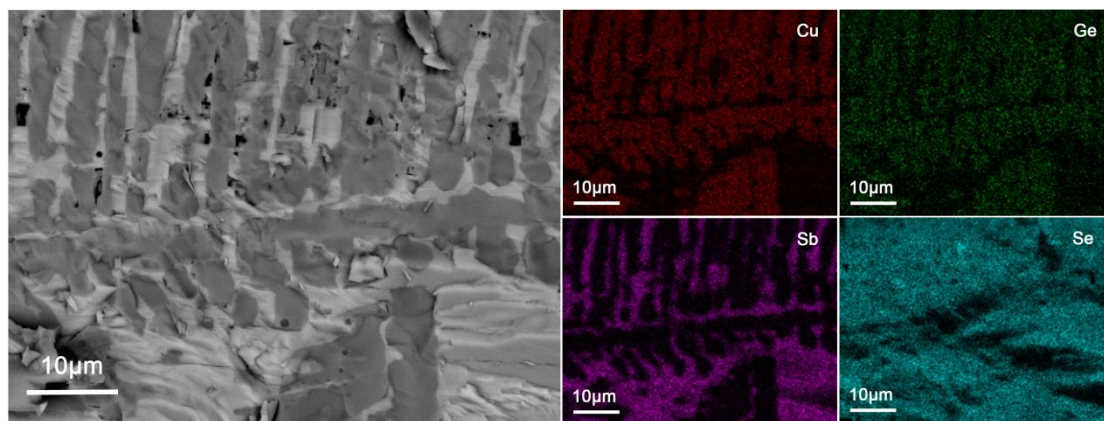


Fig. 2.15 SEM image and EDS elemental mappings of the 50Cu₂GeSe₃-50Sb₂Se₃ ceramic

2.3.2 Structure and photoelectric properties of $50(x\text{Cu}+(1-x)\text{CuI})_2\text{GeSe}_3\text{-}50\text{Sb}_2\text{Se}_3$ ceramics

It has been stated that iodine addition plays a key role determining the photoelectric properties of the $\text{GeSe}_2\text{-Sb}_2\text{Se}_3\text{-CuI}$ glass ceramics [13, 21]. In order to confirm the influence of iodine addition in these $\text{Cu}_2\text{GeSe}_3\text{-Sb}_2\text{Se}_3$ ceramics, different contents of copper(I) iodide have been used to substitute for copper in the $50\text{Cu}_2\text{GeSe}_3\text{-}50\text{Sb}_2\text{Se}_3$ ceramic. Fig. 2.16 shows the XRD patterns of the $50(x\text{Cu}+(1-x)\text{CuI})_2\text{GeSe}_3\text{-}50\text{Sb}_2\text{Se}_3$ ceramics. Similar to the $50\text{Cu}_2\text{GeSe}_3\text{-}50\text{Sb}_2\text{Se}_3$ ceramic, the diffraction peaks are also in good agreement with the JCPDS standard card (JCPDS 65-2533) of the orthorhombic-phase Cu_2GeSe_3 and the card (JCPDS 15-0861) of the orthorhombic-phase Sb_2Se_3 . With the presence of iodine, however, there are some new diffractions peaks which can be assigned to the orthorhombic phase SbSeI (JCPDS 76-1354) which increases with increasing iodine content from 0% ($50\text{Cu}_2\text{GeSe}_3\text{-}50\text{Sb}_2\text{Se}_3$) to 100% Cu substituted by CuI ($50(\text{CuI})_2\text{GeSe}_3\text{-}50\text{Sb}_2\text{Se}_3$). The $\text{Cu}_2\text{GeSe}_3/\text{Sb}_2\text{Se}_3$ ratio increases with progressively increasing iodine content. This is because the introduction of iodine promotes the formation of SbSeI , which is of course detrimental to Sb_2Se_3 .

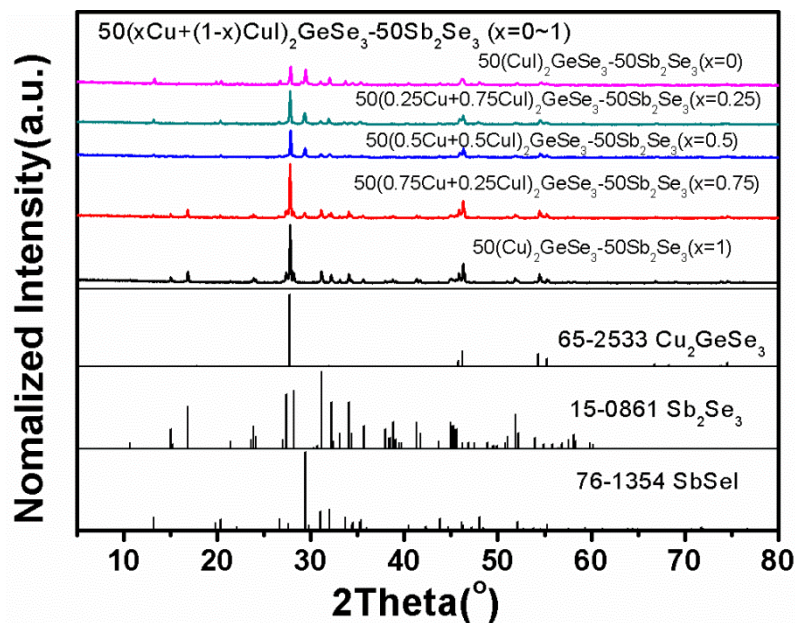


Fig. 2.16 XRD patterns of the $50\text{Cu}_2\text{GeSe}_3\text{-}50\text{Sb}_2\text{Se}_3$ ceramics with different concentration of iodine doping.

The SEM images of the cross section of $50(0.75\text{Cu}+0.25\text{CuI})_2\text{GeSe}_3$ - $50\text{Sb}_2\text{Se}_3$ and $50(0.5\text{Cu}+0.5\text{CuI})_2\text{GeSe}_3$ - $50\text{Sb}_2\text{Se}_3$ ceramics are shown in Fig. 2.17. Different from the Cu_2GeSe_3 - Sb_2Se_3 system, in the $50\text{Cu}_2\text{GeSe}_3$ - $50\text{Sb}_2\text{Se}_3$ ceramic with different contents of copper(I) iodide to substitute for copper, the original dense structure with close interconnection seems to be broken and isolated island structures appear with interpenetrating crystalline phases. By the way, the reason why we don't present the SEM images of ceramics with more I addition is that more iodine leads to brittle ceramics and it was impossible to get appropriate ceramic samples for further characterization..

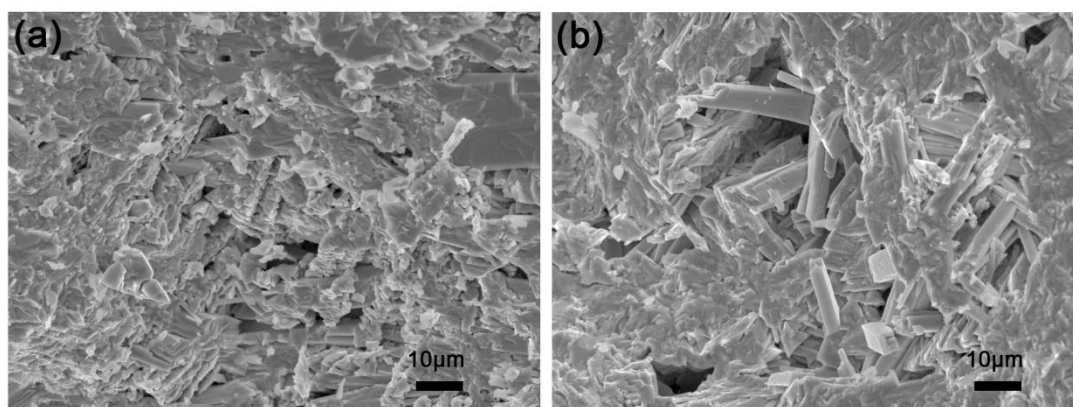


Fig. 2.17 SEM images of the cross section of the $50(x\text{Cu}+(1-x)\text{CuI})_2\text{GeSe}_3$ - $50\text{Sb}_2\text{Se}_3$ ceramics: (a) $x=0.75$ and (b) $x=0.5$

Fig. 2.18 shows the SEM image and EDS elemental mappings of the $50(0.5\text{Cu}+0.5\text{CuI})_2\text{GeSe}_3$ - $50\text{Sb}_2\text{Se}_3$ ceramic, which confirmed the presence of Cu_2GeSe_3 and Sb_2Se_3 crystal phases, as evidenced by X-rays diffraction. In comparison with $50\text{Cu}_2\text{GeSe}_3$ - $50\text{Sb}_2\text{Se}_3$ ceramic without iodine (Fig.2.15), there are also apparent interfaces between Cu_2GeSe_3 and Sb_2Se_3 or more probably SbSeI revealed by Cu, Ge, Sb and iodine EDS mappings. Selenium is homogeneously present, as the observed inhomogeneity is induced by the morphology of the examined surface. It is clear that Cu and Ge perfectly overlap and it is also the case for Sb and I. The overlap of Sb and I indicates that SbSeI phase is closely mixed with the Sb_2Se_3 phase. This is understandable, as iodine is preferentially incorporated in the Sb_2Se_3 lattice. Therefore, we can conclude that crystalline phases in the $50(0.5\text{Cu}+0.5\text{CuI})_2\text{GeSe}_3$ - $50\text{Sb}_2\text{Se}_3$ ceramic are orthorhombic-phase Cu_2GeSe_3 , Sb_2Se_3 and

new orthorhombic SbSeI phase. This is significantly different from the phases obtained by controlled crystallized of glass. In that case, a shift of diffraction peaks has been observed with the addition of I[16], The SbSeI phase appeared only with high iodine content. This is not the case here in the ceramics. The introduction of CuI, even in small quantity, leads directly to the formation of SbSeI.

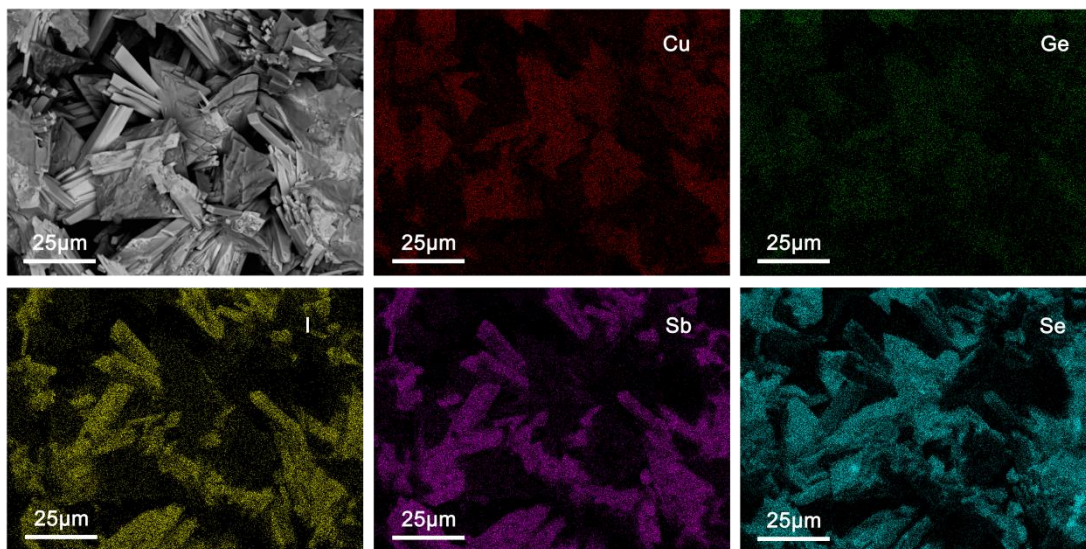


Fig. 2.18 SEM image and EDS elemental mappings of the $50(0.5\text{Cu}+0.5\text{CuI})_2\text{GeSe}_3\text{-}50\text{Sb}_2\text{Se}_3$ ceramic

From Fig. 2.18, it can be found that the Cu and Ge rich regions corresponding to the Cu_2GeSe_3 crystals are no longer interconnected with the introduction of iodine. The introduction of the iodine into the $50\text{Cu}_2\text{GeSe}_3\text{-}50\text{Sb}_2\text{Se}_3$ ceramic leads to the breakage of the conductive Cu_2GeSe_3 channels. It indicates that SbSeI is participating in the formation of conductive channels with disconnected Cu_2GeSe_3 together. One important feature of SbSeI is its much higher electric conductivity compared to Sb_2Se_3 . Therefore, the photo generated charge carriers have to go through not only the relatively conductive p-type Cu_2GeSe_3 but also the n-type SbSeI. This will of course have great influence on the PEC properties of the ceramics. The schematic illustration of the $\text{Cu}_2\text{GeSe}_3\text{-Sb}_2\text{Se}_3$ morphology with and without iodine presence is shown in Fig. 2.19.

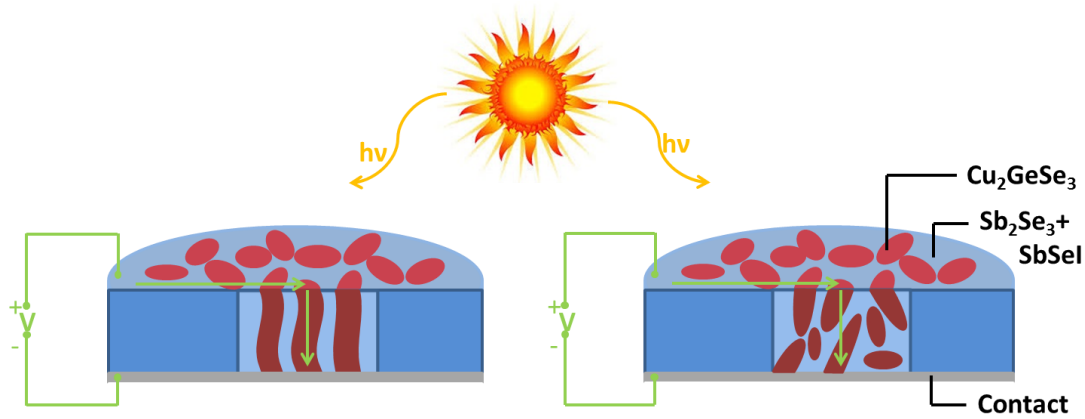


Fig. 2.19 Schematic illustration of conductive channels in the $\text{Cu}_2\text{GeSe}_3\text{-Sb}_2\text{Se}_3$ ceramics with and without iodine presence

Fig. 2.20 shows current-voltage characteristic of the $50(x\text{Cu}+(1-x)\text{CuI})_2\text{GeSe}_3\text{-}50\text{Sb}_2\text{Se}_3$ ceramics under chopped illumination. From Fig. 2.20 and Fig. 2.14 (e), it can be found that $50(x\text{Cu}+(1-x)\text{CuI})_2\text{GeSe}_3\text{-}50\text{Sb}_2\text{Se}_3$ ceramics present both n-type and p-type semiconducting behaviors, while $50\text{Cu}_2\text{GeSe}_3\text{-}50\text{Sb}_2\text{Se}_3$ ceramic only presents p-type semiconducting behaviors.

As discussed before, the interconnection between the conductive Cu_2GeSe_3 crystals can be interrupted by the introduction of iodine. The photo charge generation and charge transfer must go through the p-type Cu_2GeSe_3 as well as the n-type SbSeI . This gives rise to simultaneous n-type and p-type semiconducting behaviors as shown in Fig. 2.20. This demonstrates also the existence of p-n junctions inside the glass-ceramics, which can be very helpful for charge separation. The photocurrent intensity is similar with positive and negative bias (fig. 2.20 (a)), indicating that the conductivity of the n-type Sb_2Se_3 has been greatly improved through iodine doping. The conduction type and the resistivity of different ceramics are measured and collected in Table 2.2. In order to understand the influence of iodine presence on the resistivity of the Sb_2Se_3 phase, we prepared several samples by progressively substituting selenium with iodine. The results indicate that the resistivity markedly decreases with iodine doping and the more iodine. It can be seen from the table that with 5% selenium substituted by iodine, the resistivity can be decreased from $3.25 \times 10^8 \Omega \cdot \text{m}$ for the pure Sb_2Se_3

to $1.73 \times 10^3 \Omega \cdot \text{m}$. Further substitution will lead to still lower conductivity. At the same time, the introduction of iodine doesn't change the conduction type of Sb_2Se_3 which remains n type. The self-organized p-n junctions could be very helpful for fabricating efficient photovoltaic solar cells if the generated charge carriers can be efficiently extracted.

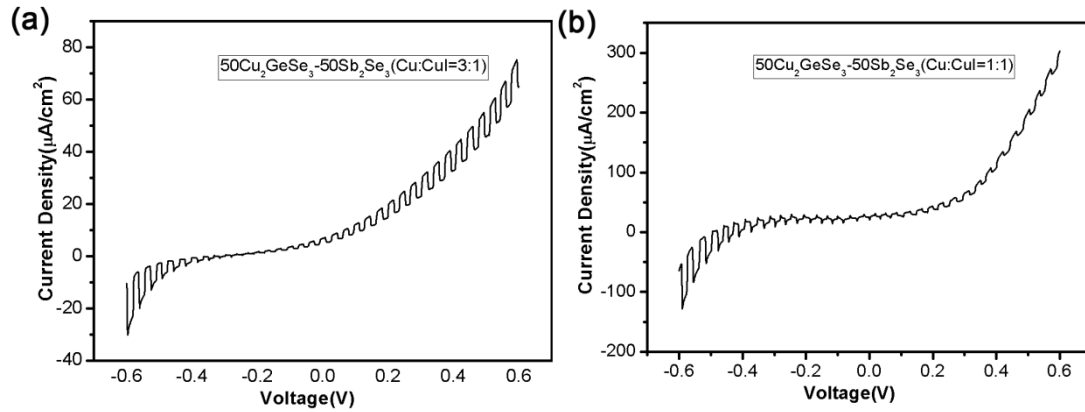


Fig. 2.20 Current-voltage characteristic of the the $50(x\text{Cu}+(1-x)\text{CuI})_2\text{GeSe}_3\text{-}50\text{Sb}_2\text{Se}_3$ ceramics under chopped illumination: (a) $x=0.75$ and (b) $x=0.5$

Table 2.2 Resistivity of the samples measured by the four-point probe method and p/n type measured with a Semilab PN tester

Samples	$50(0.75\text{Cu}+0.25\text{CuI})_2\text{GeSe}_3\text{-}50\text{Sb}_2\text{Se}_3$	$50(0.5\text{Cu}+0.5\text{CuI})_2\text{GeSe}_3\text{-}50\text{Sb}_2\text{Se}_3$	Sb_2Se_3	$\text{Sb}_2(\text{Se}_{0.95}\text{I}_{0.05})_3$	$\text{Sb}_2(\text{Se}_{0.90}\text{I}_{0.10})_3$	Cu_2GeSe_3
Resistivity/ $\Omega \cdot \text{m}$	2.17	3.30	3.25×10^8	1.73×10^3	1.76×10^2	0.12
Conduction type	N	N	N	N	N	P

2.4 Conclusions

Ceramics with an interpenetrating heterojunction network formed by two relatively narrow bandgap semiconductors have been prepared. This structure results in high

photocurrent attributed to the low conductive Sb_2Se_3 or more probably SbSeI , who is efficient for charge photo-generation and to the highly conductive Cu_2GeSe_3 crystals who plays the role of an efficient charge collector by forming conductive channels. The influence of iodine doping processes on the microstructure and photoelectrical properties of the ceramics has been investigated. The substitution of Cu by CuI in the $\text{Cu}_2\text{GeSe}_3\text{--Sb}_2\text{Se}_3$ based ceramics leads to the breakage of the conductive Cu_2GeSe_3 channels. Unlike in the glass ceramics, the introduction of iodine does not lead to partial substitution of selenium by iodine in the Sb_2Se_3 structure, but directly to the formation of n-type SbSeI with significantly higher conductivity. The obtained ceramics show simultaneous n-type and p-type semiconducting behaviors, demonstrating the existence of p-n junctions which are very useful for the separation of photogenerated charge carriers.

2.5 References

- [1] MS Iovu, EP Colomeico and IA Vasiliev, *Photoconductivity of Amorphous Sb_2Se_3 and Sb_2Se_3 : Sn Thin Films*. Chalcogenide Lett, **4**((2007) 109-113.
- [2] Rutvik J Mehta, C Karthik, Wei Jiang, B Singh, Yunfeng Shi, Richard W Siegel, Theo Borca-Tasciuc and Ganpati Ramanath, *High electrical conductivity antimony selenide nanocrystals and assemblies*. Nano letters, **10**(11) (2010) 4417-4422.
- [3] Tianyou Zhai, Mingfu Ye, Liang Li, Xiaosheng Fang, Meiyong Liao, Yongfang Li, Yasuo Koide, Yoshio Bando and Dmitri Golberg, *Single - Crystalline Sb_2Se_3 Nanowires for High - Performance Field Emitters and Photodetectors*. Advanced Materials, **22**(40) (2010) 4530-4533.
- [4] Zhengtao Deng, Masud Mansuripur and Anthony J Muscat, *Simple colloidal synthesis of single-crystal Sb-Se-S nanotubes with composition dependent band-gap energy in the near-infrared*. Nano letters, **9**(5) (2009) 2015-2020.
- [5] Xinsheng Liu, Jie Chen, Miao Luo, Meiyong Leng, Zhe Xia, Ying Zhou, Sikai Qin, Ding-Jiang Xue, Lu Lv and Han Huang, *Thermal evaporation and characterization of Sb_2Se_3*

thin film for substrate Sb₂Se₃/CdS solar cells. ACS applied materials & interfaces, **6**(13) (2014) 10687-10695.

[6] LD Ivanova, LI Petrova, Yu V Granatkina and VS Zemskov, *Thermoelectric materials based on Sb₂Te₃-Bi₂Te₃ solid solutions with optimal performance in the range 100–400 K*. Inorganic Materials, **43**(9) (2007) 933-937.

[7] E Abd El-Wahabb, SS Fouad and M Fadel, *Theoretical and experimental study of the conduction mechanism in Sb₂Se₃ alloy*. Journal of materials science, **38**(3) (2003) 527-532.

[8] Marina R Filip, Christopher E Patrick and Feliciano Giustino, *G W quasiparticle band structures of stibnite, antimonelite, bismuthinite, and guanajuatite*. Physical Review B, **87**(20) (2013) 205125.

[9] MA Villarreal, BJ Fernández, M Pirela and A Velásquez-Velásquez, *Electrical properties of the ternary compound Cu₂GeSe₃*. REVISTA MEXICANA DE FISICA S, **53**(7) (2007) 303.

[10] Debao Wang, Caixia Song, Xun Fu and Xin Li, *Growth of one-dimensional Sb₂S₃ and Sb₂Se₃ crystals with straw-tied-like architectures*. Journal of crystal growth, **281**(2) (2005) 611-615.

[11] G Marcano and R Marquez, *Variable-range hopping conductivity and magnetoresistance in p-type Cu₂GeSe₃*. Journal of Physics and Chemistry of Solids, **64**(9) (2003) 1725-1727.

[12] Bimal Kumar Sarkar, Ajay Singh Verma and PS Deviprasad, *Temperature induced band gap shrinkage in Cu₂GeSe₃: Role of electron–phonon interaction*. Physica B: Condensed Matter, **406**(14) (2011) 2847-2850.

[13] Yang Xu, Bo Fan, Xianghua Zhang, Qianhong Shen, Minjia Wang and Hongli Ma, *Crystallization optimization of the 40GeSe₂-40Sb₂Se₃-20CuI glass for improvement of photoelectric properties*. Journal of Non-Crystalline Solids, **431**((2016) 61-67.

[14] Xianghua Zhang, Yang Xu, Qianhong Shen, Bo Fan, Xusheng Qiao, Xianping Fan, Hui Yang, Qun Luo, Laurent Calvez and Hongli Ma, *Enhancement of charge photo-generation*

and transport via an internal network of Sb_2Se_3/Cu_2GeSe_3 heterojunctions. *Journal of Materials Chemistry A*, **2**(40) (2014) 17099-17106.

[15] Adrian W Bott, *Electrochemistry of semiconductors*. Current Separations, **17**((1998) 87-92.

[17] Benoit Chavillon, Laurent Cario, Adele Renaud, Franck Tessier, François Cheviré, Mohammed Boujtita, Yann Pellegrin, Errol Blart, Amanda Smeigh and Leif Hammarstrom, *P-type nitrogen-doped ZnO nanoparticles stable under ambient conditions*. *Journal of the American Chemical Society*, **134**(1) (2011) 464-470.

[18] EA El-Sayad, *Compositional dependence of the optical properties of amorphous Sb_2Se_3 - xS_x thin films*. *Journal of Non-Crystalline Solids*, **354**(32) (2008) 3806-3811.

[19] G Marcano, L Nieves and GS Perez, *Temperature dependence of the fundamental absorption edge in Cu_2GeSe_3* . *Japanese Journal of Applied Physics*, **39**(S1) (2000) 290.

[20] Christopher E Patrick and Feliciano Giustino, *Structural and electronic properties of semiconductor - sensitized solar - cell interfaces*. *Advanced Functional Materials*, **21**(24) (2011) 4663-4667.

[21] Xianghua Zhang, Yang Xu, Qianhong Shen, Bo Fan, Xusheng Qiao, Xianping Fan, Hui Yang, Qun Luo, Laurent Calvez and Hongli Ma, *Enhancement of charge photo-generation and transport via an internal network of Sb_2Se_3/Cu_2GeSe_3 heterojunctions*. *Journal of Materials Chemistry A*, **2**(40) (2014) 17099-17106.

Chapter III: Study of semiconducting ceramics in the $\text{Cu}_3\text{SbSe}_4\text{-Sb}_2\text{Se}_3$ system

3.1 Introduction

Previous works have demonstrated that the controlled crystallization of chalcogenide glasses allows to obtain glass-ceramics with promising photoelectric properties[1, 2]. It has been demonstrated that the enhanced charge separation and transfer are greatly facilitated by the intern Sb_2Se_3 - Cu_2GeSe_3 heterojunctions created by controlling the crystallization of the precursor glass $40\text{Sb}_2\text{Se}_3$ - 40GeSe_2 - 20CuI [3]. Intense photocurrent can be generated under visible illumination. And originally inspired by this work, in Chapter 2, we presented a method for preparing semiconducting ceramics directly with these two semiconducting phases, Sb_2Se_3 and Cu_2GeSe_3 having relatively narrow bandgap. The only element which is not abundant on earth is germanium even its content is relatively low, less than 10% in the ceramic.. To overcome this problem, we have studied the possibility of germanium substitution in order to reduce the cost of raw materials.

Among the possible candidates, we payed attention to the $\text{I}_3\text{-V-VI}_4$ p type semiconductor Cu_3SbSe_4 mostly known for its thermoelectric properties [4-6] and its low temperature quasi-independent thermal conductivity[7-9]. Being the structural analogue of I-III-VI chalcogenide crystals, its crystal lattice can be described as zinc-blend derived with ideal diamond-like structure consisted of elementary tetrahedron-units[10]. Thus, each chalcogenide atom is bonded to three I and one V atom in this coordination. Atomic energy levels and electronic structure of Cu_3SbSe_4 is described in details elsewhere [4, 11]. Cu_3SbSe_4 is a narrow band gap semiconductor with $E_g = 0.3\text{-}0.4\text{eV}$ inferior to the Cu_2GeSe_3 band gap estimated as $0.7\text{-}0.8\text{eV}$ [4]. It shows electrical conductivity comparable and even higher than Cu_2GeSe_3 [4, 5, 12].

As we already know, Sb_2Se_3 n-type semiconductor is a good light absorber[13]. It is widely used for the layered structure where it shows up to 97% light absorption for 350 nm-thick film [14], as well as for nanoparticles fabrication which can play the role of electron donor in Sb_2Se_3 /Metal oxide interface [15] or form the heterojunction with I-V-VI₂ compositions for light detection purposes[16]. In this study, Sb_2Se_3 is still chosen to play the role of light absorber and P-N junction former.

The main goal of this study is to demonstrate the feasibility of bulk p-n junction between Sb_2Se_3 and Cu_3SbSe_4 in order to take profit of the high absorption coefficient of Sb_2Se_3 while

minimizing the issue associated with its high resistivity. The final objective is to use this structure for having high absorption of solar spectrum to efficiently generate charge carrier and outstanding carrier separation and transportation ability.

3.2 Experimental Procedure

3.2.1 Preparation of $\text{Cu}_3\text{SbSe}_4\text{-Sb}_2\text{Se}_3$ ceramics

The preparation process of the $\text{Cu}_3\text{SbSe}_4\text{-Sb}_2\text{Se}_3$ ceramics is the same as for the $\text{Cu}_2\text{GeSe}_3\text{-Sb}_2\text{Se}_3$ system by the melt-quenching approach in vacuum sealed silica tube. The schematic diagram and thermal profile are shown in Fig. 2.2 and Fig. 2.3 in Chapter 2. The only difference is located in the raw materials type and composition. Without germanium, the base ceramics are synthesized using the polycrystalline antimony (99.999%), selenium (99.999%), Copper (99.9%) and/or CuI (98%) as starting materials.

After the process of tube cleaning, vacuum drying, raw materials loading and sealing, we can get a silica tube with 9 mm internal diameter filled with materials of a certain composition. The tube containing the mixture was then put into a rocking furnace for melt-quenching processing.

The thermal profile is as follow, the silica tube containing all the starting materials was heated to 800°C at the rate of 1.5°C/min and hold for about 12 hours to ensure a thorough reaction and homogenization. Then the furnace was cooled down to 700 °C and the thermal quenching was performed by putting the sealed tube into water at room temperature. The quenching step is to ensure the product quality and ceramics separation as mentioned in last chapter. The thermal shock in the quenching process generated high mechanical stresses in the ceramics. In order to reduce these stresses, the tube was annealed at 200 °C for 3 h. The ceramics are then cooled slowly and released from the silica tube. After the annealing, a ceramic rod of 9 cm was obtained and was sliced into discs with the thickness of about 2 mm before polishing for different measurements.

3.2.2 Presentation of characterization techniques

As stated in chapter 2, X-ray diffraction (XRD) analysis was carried out on a PANalytical's X-ray diffractometer with a step width of 0.02 ° and a counting duration of 0.13

s/step. To characterize the photoelectric performance, the photo-electro-chemical (PEC) measurement has been carried out by using the classic 3-electrode method with a chopped illumination of 400 W.m^{-2} from a broad band tungsten halogen lamp. Scanning electron microscope (SEM) images and Energy Dispersive Spectrometer (EDS) elemental mappings were obtained with a JEOL JSM-7100F Thermal field emission electron microscope equipped with an EDS system. High resolution transmission electron microscopy (HRTEM) images and Energy Dispersive Spectrometer (EDS) data were obtained from a JEOL JEM-2100 field emission transmission electron microscope. Electric conductivity of the ceramics was measured by the four-point probe method.

3.3 Results and discussion

3.3.1 Structure and photoelectric properties of $x(0.9\text{Cu}+0.1\text{CuI})_3\text{SbSe}_4-(100-x)\text{Sb}_2\text{Se}_3$ ceramics ($x=30, 40, \dots, 70$)

Taking the classical $40\text{Sb}_2\text{Se}_3-40\text{GeSe}_2-20\text{CuI}$ glass-ceramic as reference, we fixed the proportion of Sb/I as 4:1 at first. So the copper source of raw materials is about 90% from Cu and 10% from CuI. Then we adjusted the ratio of raw materials to get ceramics with different composition $x(0.9\text{Cu}+0.1\text{CuI})_3\text{SbSe}_4-(100-x)\text{Sb}_2\text{Se}_3$ ($x=30, 40, \dots, 70$).

Fig. 3.1 shows the X-ray diffraction patterns of as prepared bulk samples with different $\text{Cu}_3\text{SbSe}_4/\text{Sb}_2\text{Se}_3$ ratios. Cu_3SbSe_4 is clearly identified in the compounds and the diffraction patterns are in perfect agreement with PDF 85-0003 pattern card showing tetragonal structure with $I4_2m$ symmetry space group and lattice constants $a=5.66$, $b=5.66$, $c=11.28$, $\alpha=\beta=\gamma=90^\circ$

Sb_2Se_3 is crystallized in orthorhombic structure with $\text{Pbnm}(62)$ space group. However, the peak positions of certain orientations are slightly deviated from standard pattern of PDF 15-0861 card which is probably due to the iodine doping. This phenomena has been observed elsewhere [3]. It is generally observed that the relative intensity between Cu_3SbSe_4 and Sb_2Se_3 peaks is changed as function of composition (with different $\text{Cu}_3\text{SbSe}_4/\text{Sb}_2\text{Se}_3$ ratios), but no shift for peaks position can be observed. But here something happens to Sb_2Se_3 with the introduction of iodine. The addition of iodine doesn't lead to new peaks corresponding to the phase of SbSeI , as it was the case with the $\text{Cu}_2\text{GeSe}_3\text{-Sb}_2\text{Se}_3$ system studied in chapter 2. Iodine may exist in the lattice of Sb_2Se_3 by replacing selenium and causes the shift of diffraction peaks on XRD patterns. No shift can be observed with the diffraction peaks

attributed to Cu_3SbSe_4 . Therefore, it is easy to control the ratio of the p-type Cu_3SbSe_4 over the n-type (iodine-doped) Sb_2Se_3 ratios in the final samples simply by adjusting the starting compositions. No secondary phase will be created.

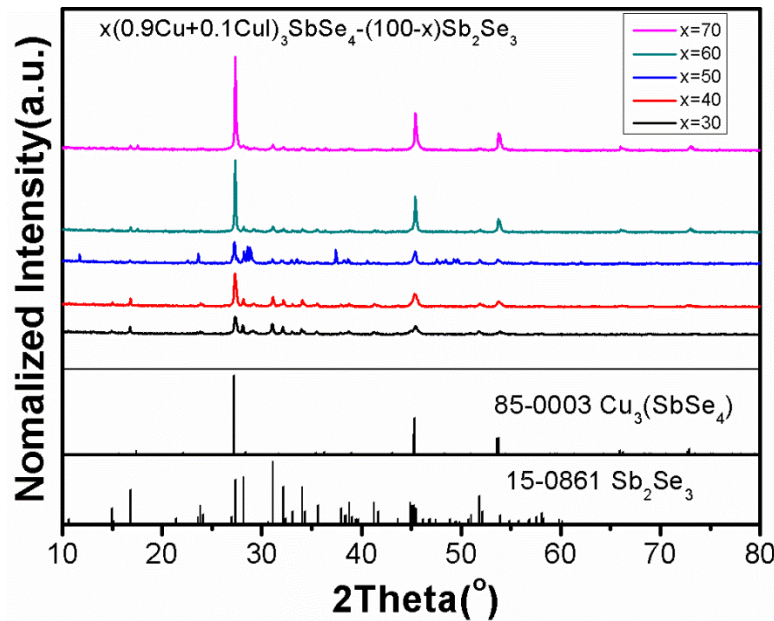


Fig. 3.1 XRD patterns of the $x(0.9\text{Cu}+0.1\text{CuI})_3\text{SbSe}_4-(100-x)\text{Sb}_2\text{Se}_3$ ceramics ($x=30, 40, \dots, 70$)

It is known that Sb_2Se_3 upon crystallization tends to form the rod-like crystals[3, 17]. Fig. 3.2 (a) is the SEM image for $30(0.9\text{Cu}+0.1\text{CuI})_3\text{SbSe}_4-70\text{Sb}_2\text{Se}_3$ ceramic (SS3-7). One can observe Sb_2Se_3 rods with diameter of $2-3\mu\text{m}$ along with numerous flake-like crystals of different sizes which can be assigned to Cu_3SbSe_4 with higher symmetry. With the increase of Cu_3SbSe_4 fraction (Fig. 3.2(b), (c)), the rods of Sb_2Se_3 crystals in the $40(0.9\text{Cu}+0.1\text{CuI})_3\text{SbSe}_4-60\text{Sb}_2\text{Se}_3$ ceramic (SS4-6) and $50(0.9\text{Cu}+0.1\text{CuI})_3\text{SbSe}_4-50\text{Sb}_2\text{Se}_3$ ceramic (SS5-5) become less visible and are more and more immersed in the Cu_3SbSe_4 crystals. In the $60(0.9\text{Cu}+0.1\text{CuI})_3\text{SbSe}_4-40\text{Sb}_2\text{Se}_3$ ceramic (Fig. 3.2 (c)), for example, a network of Sb_2Se_3 rods can be clearly observed in the gap between two Cu_3SbSe_4 crystals. With further increase of Cu_3SbSe_4 concentration, we observed the transformation of leaf-like structure (Fig. 3.2 (d)) to denser structure where leafs of Cu_3SbSe_4 are sintered (Fig. 3.2 (e)) and completely cover Sb_2Se_3 rods which are now barely observable in this type of topology.

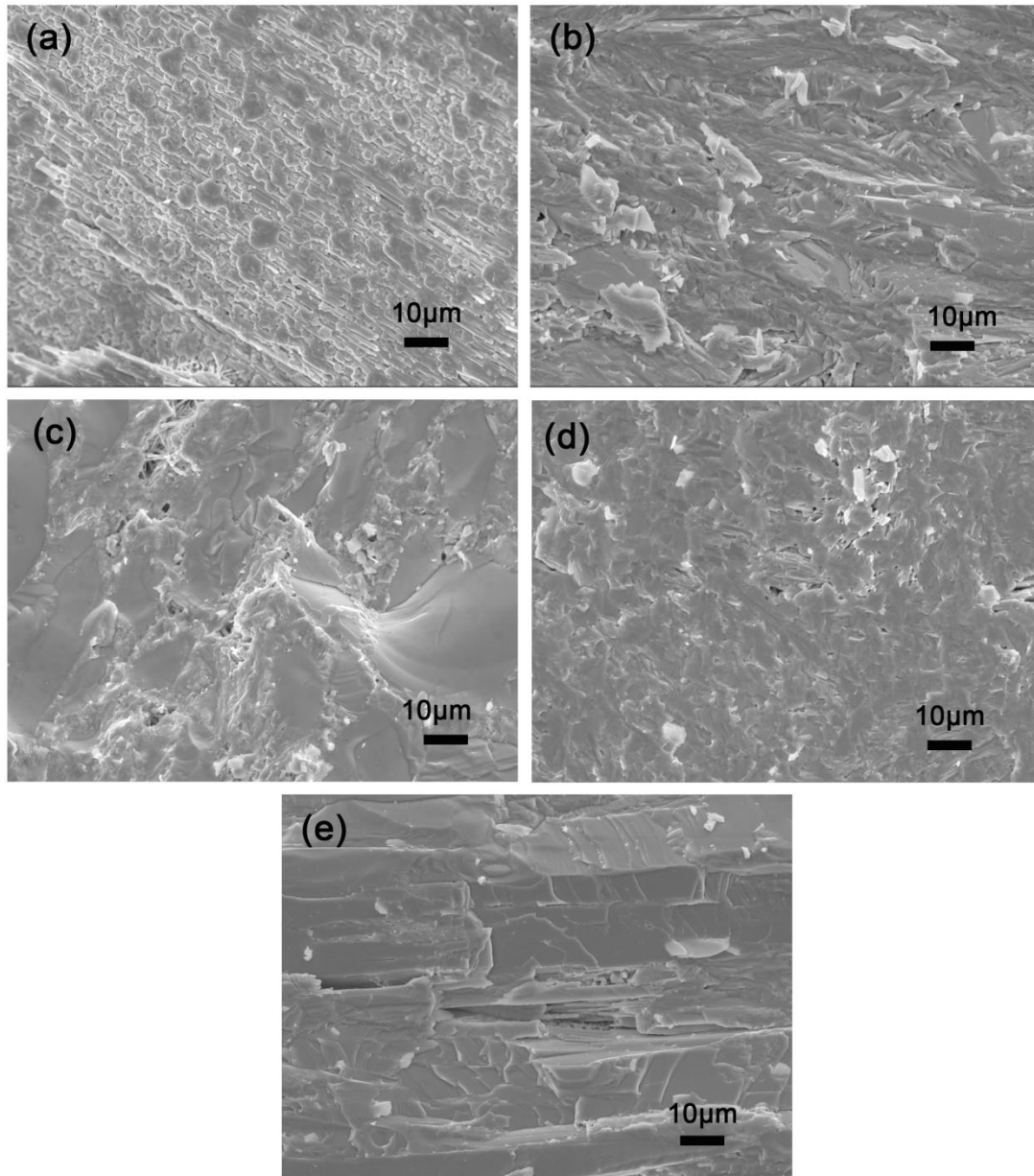


Fig. 3.2 SEM images of the cross section of the $x(0.9\text{Cu}+0.1\text{CuI})_3\text{SbSe}_4-(100-x)\text{Sb}_2\text{Se}_3$ ceramics: (a) $x=30$; (b) $x=40$; (c) $x=50$; (d) $x=60$, (e) $x=70$

Table 3.1 represents the resistivity of the prepared samples. In this system, Cu_3SbSe_4 ($10^{-1}\Omega\cdot\text{m}$) is known to have much lower resistivity than Sb_2Se_3 ($10^8\Omega\cdot\text{m}$). However, it can be

see that the composition with 30% of Cu_3SbSe_4 shows the lowest resistivity equal to $0.29 \Omega\cdot\text{m}$. Higher Cu_3SbSe_4 content does not lead to lower resistivity. In fact, the resistivity strongly depends on the microstructure. An efficient conduction structure is a well-connected network, easily formed by rod-like Sb_2Se_3 crystals and covered by conductive Cu_3SbSe_4 crystals. This type of structures will form heterojunctions facilitating charge separation and transport. Similar structure has already been reported[3]. The $50(0.9\text{Cu}+0.1\text{CuI})_3\text{SbSe}_4$ - $50\text{Sb}_2\text{Se}_3$ composition showed the highest resistivity among all the prepared ceramics. While on the whole, all the ceramics as prepared showed a resistivity in the same order of magnitude ($10^{-1}\Omega\cdot\text{m}$) because each one has a similar heterojunction network in macro-levels. Thanks to the network formed by Sb_2Se_3 and the Cu_3SbSe_4 conductive channel, the resistivity values of the all $x(0.9\text{Cu}+0.1\text{CuI})_3\text{SbSe}_4$ -($1-x$) Sb_2Se_3 ceramics shift towards pure Cu_3SbSe_4 crystal within the precision of the measurement.

Table 3.1 Resistivity of the pure phase crystals and the ceramics

Samples	SS7-3	SS6-4	SS5-5	SS4-6	SS3-7	Sb_2Se_3	Cu_3SbSe_4
$\text{Cu}_3\text{SbSe}_4/\text{Sb}_2\text{Se}_3$	7/3	6/4	5/5	4/6	3/7	-	-
Resistivity/ $\Omega\cdot\text{m}$	0.53	0.55	0.70	0.43	0.29	3.25×10^8	0.57

To characterize the photoelectric performance, the photo-electro-chemical (PEC) measurement has been performed for different compositions by using the classic 3-electrode method with a chopped illumination of $400 \text{ W}\cdot\text{m}^{-2}$ from a broad band tungsten halogen lamp. The results are shown in fig. 3.3. The ceramics containing iodine show both p-type and n-type semiconducting phases because the photocurrent is measured both at positive and negative bias[18, 19]. By comparing the PEC performance of different compositions, it can be seen that there is no obvious dependence between conductivity and photocurrent density. The $50(0.9\text{Cu}+0.1\text{CuI})_3\text{SbSe}_4$ - $50\text{Sb}_2\text{Se}_3$ ceramic shows weaker conductivity compare to the other compositions. However, this composition gives the most intense photocurrent, up to

$50 \mu\text{A}/\text{cm}^2$. A highly conductive network is of course favorable for charge conduction. However, the photocurrent intensity depends also on the light absorption, charge generation and separation efficiency as well as its life time.

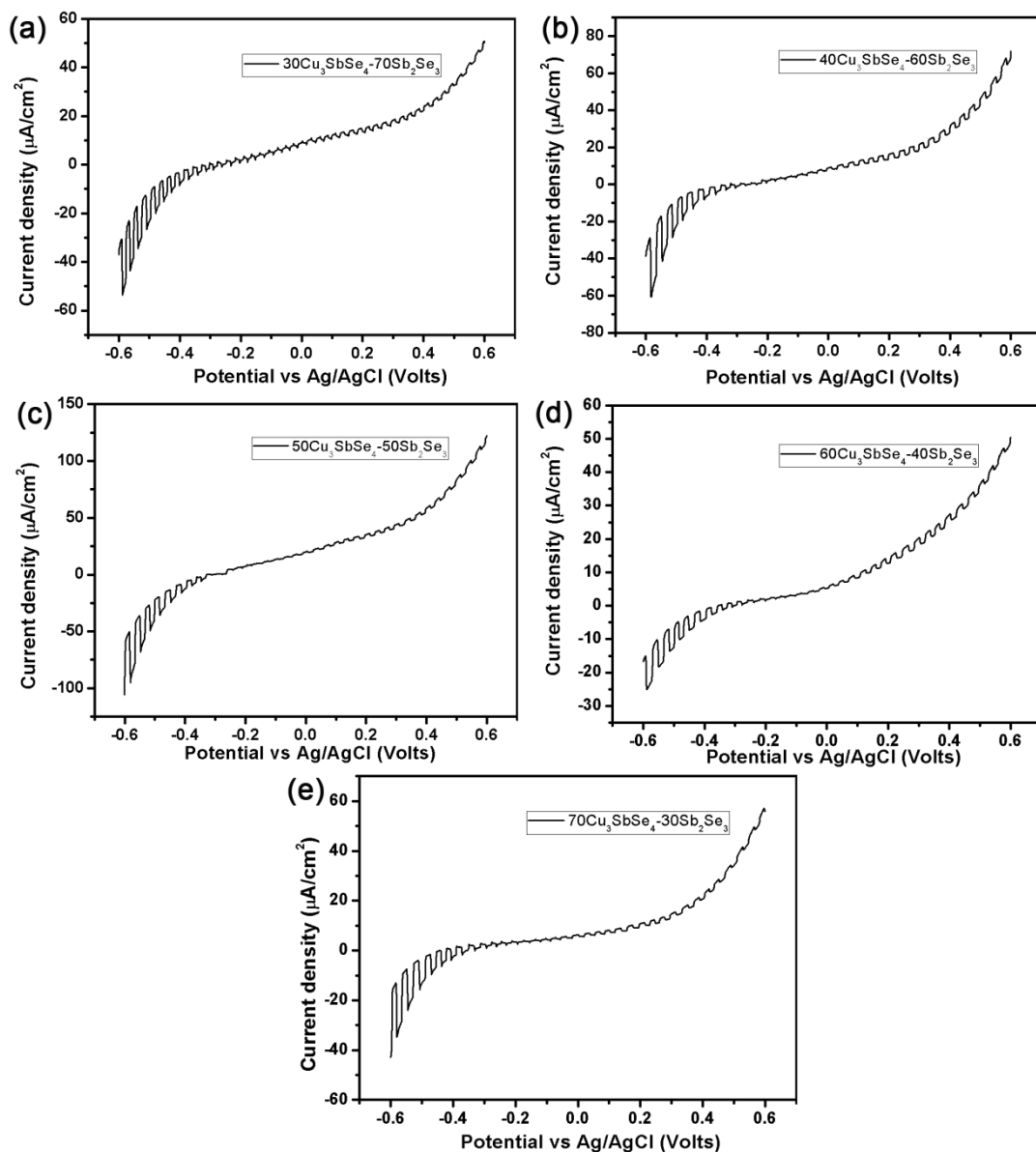


Fig. 3.3 Current-voltage characteristic of the $x(0.9\text{Cu}+0.1\text{CuI})_3\text{SbSe}_4-(1-x)\text{Sb}_2\text{Se}_3$ ceramics under chopped illumination lamp: (a) $x=30$; (b) $x=40$; (c) $x=50$; (d) $x=60$, (e) $x=70$

To confirm the formation of p-n heterojunctions, the $60(0.9\text{Cu}+0.1\text{CuI})_3\text{SbSe}_4\text{-}40\text{Sb}_2\text{Se}_3$ ceramic is observed under TEM. In order to obtain TEM samples with high quality, there are several preprocessing tasks to the ceramic discs that must be performed. Firstly, the discs were cut into squares of $2\text{mm}\times 2\text{mm}$. The sample thickness was reduced to under $100\mu\text{m}$ by thinning with dimple grinder. Further thickness reduction was carried out by argon ion beam milling until the perforation. The TEM results are shown in Fig. 3.4(a). Two types of crystals are clearly present with very different lattice parameter, corresponding respectively to Sb_2Se_3 and Cu_3SbSe_4 . HRTEM images show that the typical lattice spacing of the top left part is 5.20 \AA , which is in good agreement with the standard value for (120) plane of Sb_2Se_3 orthorhombic phase. The lattice spacing of the other part (down right) is 11.68 \AA , which corresponds to the (001) plane of Cu_3SbSe_4 tetragonal phase. The tight interface indicates the heterojunction formed by two crystals.

EDS elemental mapping is shown in fig. 3.4 (b) where we can easily recognize a copper-poor area on the top and a copper-rich area on the bottom. The difference of copper content also confirmed that the top and bottom sections belong to different phases which can be defined as Sb_2Se_3 and Cu_3SbSe_4 respectively. The residual detection of Cu in Sb_2Se_3 is due to the analysis technique which measures the composition in the whole thickness. Even the sample is very thin, it is likely that Cu_3SbSe_4 can be above and under the Sb_2Se_3 crystals.

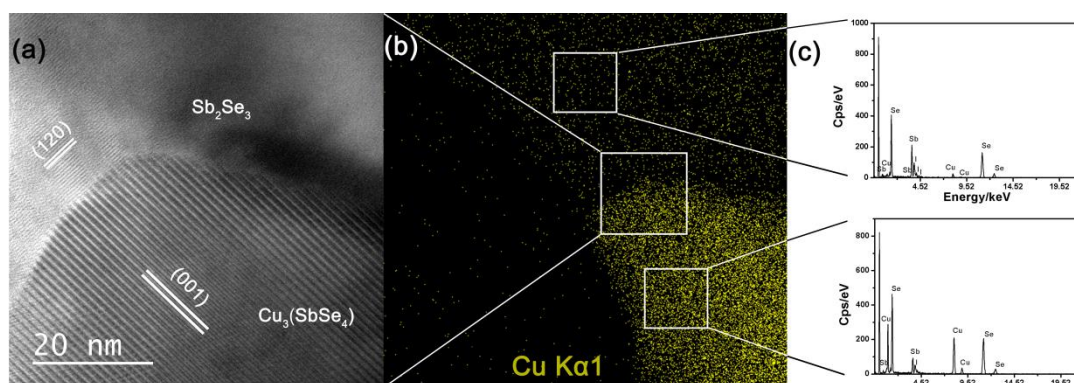


Fig. 3.4 (a) HRTEM images, (b)EDS elemental mapping and (c)EDS spectroscopy analysis of the $60\text{Cu}_3\text{SbSe}_4\text{-}40\text{Sb}_2\text{Se}_3(\text{Sb/I}=4:1)$

Fig. 3.4 (c) shows the EDS spectroscopy of two corresponding zones. The top figure shows a copper-poor result and the bottom figure gives the inverted result. The detailed information for each element is presented in Table 3.2. The copper-poor zone has an elementary composition of $\text{Cu}_{3.48}\text{Sb}_{35.14}\text{Se}_{61.39}$, close to Sb_2Se_3 , and the copper-rich part has an elementary composition of $\text{Cu}_{27.15}\text{Sb}_{13.17}\text{Se}_{59.17}\text{I}_{0.51}$, close to Cu_3SbSe_4 . The residual detection of Cu and iodine in Sb_2Se_3 and detection of iodine in Cu_3SbSe_4 may due to the analysis technique which analyzes the composition of the whole thickness. By considering the XRD patterns, we know that iodine is not in Cu_3SbSe_4 phase, but in the Sb_2Se_3 crystals

Table 3.2 Detailed EDS data of the junction

Zone in fig. 3.4	Cu	Se	Sb	I
Top zone/atom%	3.48	61.39	35.14	0
Bottom zone/atom%	27.15	59.17	13.17	0.51

The $40(0.9\text{Cu}+0.1\text{CuI})_3\text{SbSe}_4-60\text{Sb}_2\text{Se}_3$ ceramic has also been observed by SEM with EDS and elemental mapping. The element I distribution is rather complementary to that of Cu and this tends to confirm that iodine is not in Cu_3SbSe_4 . Sb and Se are (should be) present everywhere. The observed inhomogeneity of Sb and Se is likely due to the morphology of the observed surface which is not smooth..

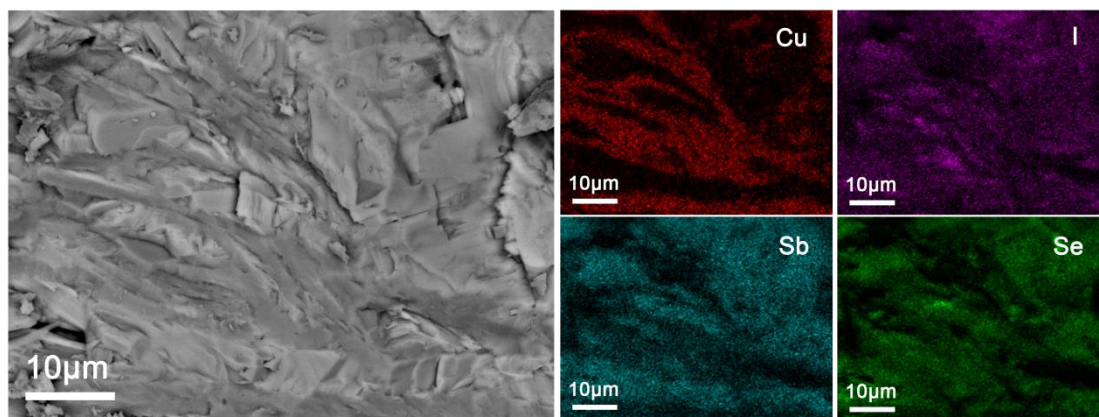


Fig. 3.5 SEM image and EDS elemental mappings of the $40(0.9\text{Cu}+0.1\text{CuI})_3\text{SbSe}_4\text{-}60\text{Sb}_2\text{Se}_3$ ceramic

3.3.2 Structure and photoelectric properties of the $40\text{Cu}_3\text{SbSe}_4\text{-}60\text{Sb}_2\text{Se}_3$ ceramics

It has been reported that the presence of iodine has a critical influence on the resistivity and the photoelectric properties of similar compounds[3, 20] and it has been demonstrated that iodine is localized in Sb_2Se_3 crystals, while the exact role of iodine has not been explained. In chapter 2, we have tried to give the fundamental explanation of iodine role in the $\text{Cu}_2\text{GeSe}_3\text{-Sb}_2\text{Se}_3$ system. In this chapter, we have prepared the $40\text{Cu}_3\text{SbSe}_4\text{-}60\text{Sb}_2\text{Se}_3$ ceramic without addition of element I in order to determine the role of iodine in $\text{Cu}_3\text{SbSe}_4\text{-Sb}_2\text{Se}_3$ ceramics.

As shown in Fig. 3.6, it can be seen that similar XRD patterns with and without addition of I for the $40\text{Cu}_3\text{SbSe}_4\text{-Sb}_2\text{Se}_3$ system can be observed. When the iodine was introduced, there are no new diffractions peaks appear which means that the introduction of iodine doesn't create new phases. This phenomenon is different from the $\text{Cu}_2\text{GeSe}_3\text{-Sb}_2\text{Se}_3$ system in which new SbSeI phase was created when introducing I.

From the relative diffraction intensity, it can be seen that the $\text{Cu}_3\text{SbSe}_4/\text{Sb}_2\text{Se}_3$ ratio decreases with the introduction of iodine. The mechanism for this decrease is still unclear and need to be studied in the future.

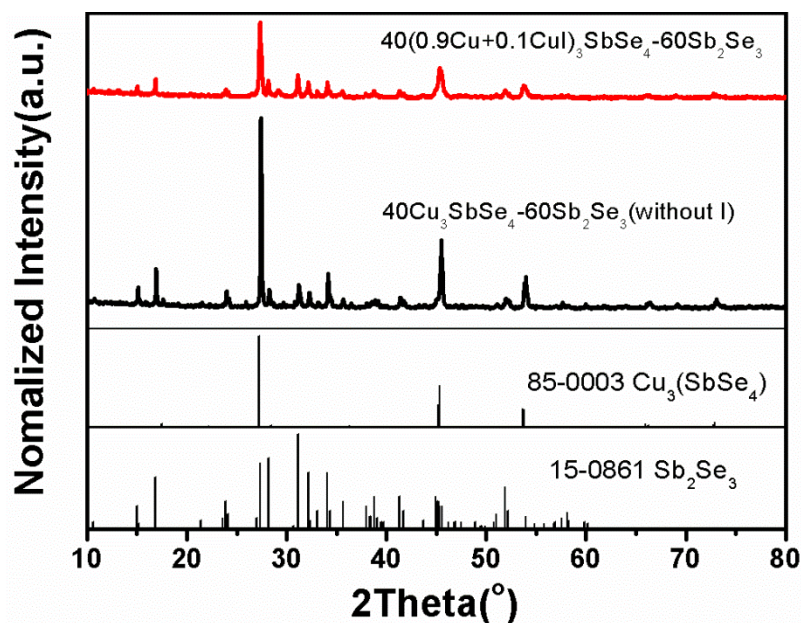


Fig. 3.6 XRD patterns of the $40\text{Cu}_3\text{SbSe}_4\text{-}60\text{Sb}_2\text{Se}_3$ ceramics with and without iodine addition

It is important to note that the introduction of iodine leads to an important decrease of resistivity. For example, the resistivity of the ceramic decreased from $9.98 \text{ } \Omega\cdot\text{m}$ for the $40\text{Cu}_3\text{SbSe}_4\text{-}60\text{Sb}_2\text{Se}_3$ to $0.43 \text{ } \Omega\cdot\text{m}$ for the $40(0.9\text{Cu}+0.1\text{CuI})_3\text{SbSe}_4\text{-}60\text{Sb}_2\text{Se}_3$ ceramic. In order to verify if iodine really modifies the Sb_2Se_3 significantly, two additional samples were prepared where 5 mol% and 10 mol% of selenium were equimolecularly substituted with iodine in the Sb_2Se_3 . As it can be seen from Table 3.2, the resistivity of the $\text{Sb}_2(\text{Se}_{0.95}\text{I}_{0.05})_3$ is $1.73 \times 10^3 \text{ } \Omega\cdot\text{m}$, which is much lower than that of the Sb_2Se_3 ($3.25 \times 10^8 \text{ } \Omega\cdot\text{m}$). The introduction of iodine is supposed to lower the valence band, leading to a wider bandgap. The rapid increase of conductivity is probably due to the formation of transport levels within the band gap. Obviously, the role of iodine is similar for both $\text{Cu}_3\text{SbSe}_4\text{-Sb}_2\text{Se}_3$ and $\text{Cu}_2\text{GeSe}_3\text{-Sb}_2\text{Se}_3$ systems. It gives a huge boost of conductivity for Sb_2Se_3 and allows it to participate in the charge transfer mechanism. This is an important finding, as Sb_2Se_3 has been considered for many applications with the major issue of too low conductivity.

Table 3.2 Resistivity of the pure phase crystals and the ceramics

Samples	$40(0.9\text{Cu}+0.1\text{CuI})_3\text{SbSe}_4$ - $60\text{Sb}_2\text{Se}_3$	$40\text{Cu}_3\text{SbSe}_4$ - $60\text{Sb}_2\text{Se}_3$	Sb_2Se_3	$\text{Sb}_2(\text{Se}_{0.95}\text{I}_{0.05})_3$	$\text{Sb}_2(\text{Se}_{0.90}\text{I}_{0.10})_3$	Cu_3SbSe_4
Resistivity/ $\Omega\cdot\text{m}$	0.43	9.98	3.25×10^8	1.73×10^3	1.76×10^2	0.57

From PEC curves shown in Fig. 3.3 (a-e), we can clearly see that samples containing iodine formed p-n junctions, while in the absence of iodine (Fig. 3.7) there only is p-type Cu_3SbSe_4 which contributes to the photocurrent. As stated earlier, the n-type semiconductor contributes to the photocurrent under positive bias, while p-type to the photocurrent under negative bias[18, 19]. Having both p and n type semiconductors is contributing to the photocurrent under both biases. By comparing PEC performance of different compositions in relationship with the conductivity, one can conclude that there is no absolute dependence between these two properties. The composition $50\text{Cu}_3\text{SbSe}_4$ - $50\text{Sb}_2\text{Se}_3$ shows relatively weak conductivity compared to the other compositions. However, we can observe the most intense photocurrent up to $50\mu\text{A}/\text{cm}^2$ for this composition. It should be pointed out that the photocurrent intensity depends on several parameters such as light absorption coefficient, charge generation and separation efficiency, lifetime of charge carriers and charge transfer capability.

As we could observe in Fig. 3.7, the $40\text{Cu}_3\text{SbSe}_4$ - $60\text{Sb}_2\text{Se}_3$ ceramic without iodine shows only p-type photocurrent which signifies that the charge generation and transfer path do not take place in the n-type phase. However, p-n junctions between Cu_3SbSe_4 and Sb_2Se_3 can still exist, which facilitate the separation of charges generation in the p-type phase. This can explain why this ceramic has much higher photocurrent than the Cu_3SbSe_4 alone.. The insufficient conductivity of Sb_2Se_3 in the absence of iodine prevents it from the participation in charge transfer process. The charges generated inside the Sb_2Se_3 do not have enough mobility. The charges can only be efficiently collected and transported to the back contact by the conductive channels throughout the bulk formed by the Cu_3SbSe_4 with relatively low resistivity.

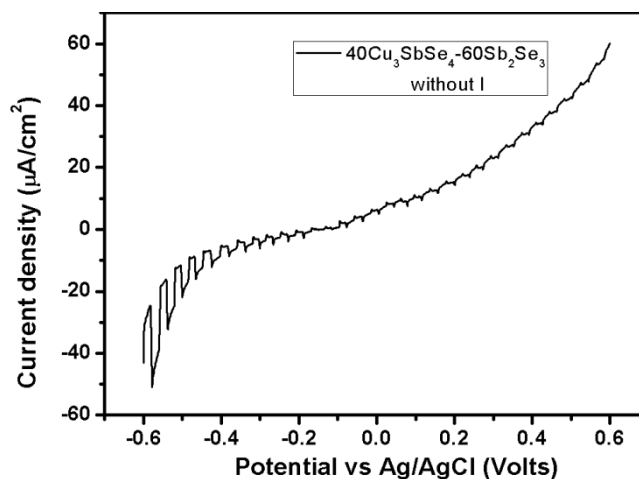


Fig. 3.7 Current-voltage characteristic of the ceramic of $40\text{Cu}_3\text{SbSe}_4\text{-}60\text{Sb}_2\text{Se}_3$ under chopped illumination lamp

Fig. 3.8 shows the SEM image and EDS elemental mappings of the $40\text{Cu}_3\text{SbSe}_4\text{-}60\text{Sb}_2\text{Se}_3$ ceramic (without I). We can find logically that Sb and Se are homogeneously distributed since they exist in both phases. The observed inhomogeneity is due to the morphology of the surface which is not polished and far from smooth. A sandwich structured (copper-rich zone and -poor zone) is observed and these two phases grow in parallel. Unlike the sample with I, the parallel conductive channels of Cu_3SbSe_4 are more regular and complete which can be more efficient for the transportation of charge carriers. This complete channel may also be the reason of the only p-type behavior of this ceramic as shown in Fig. 3.7.

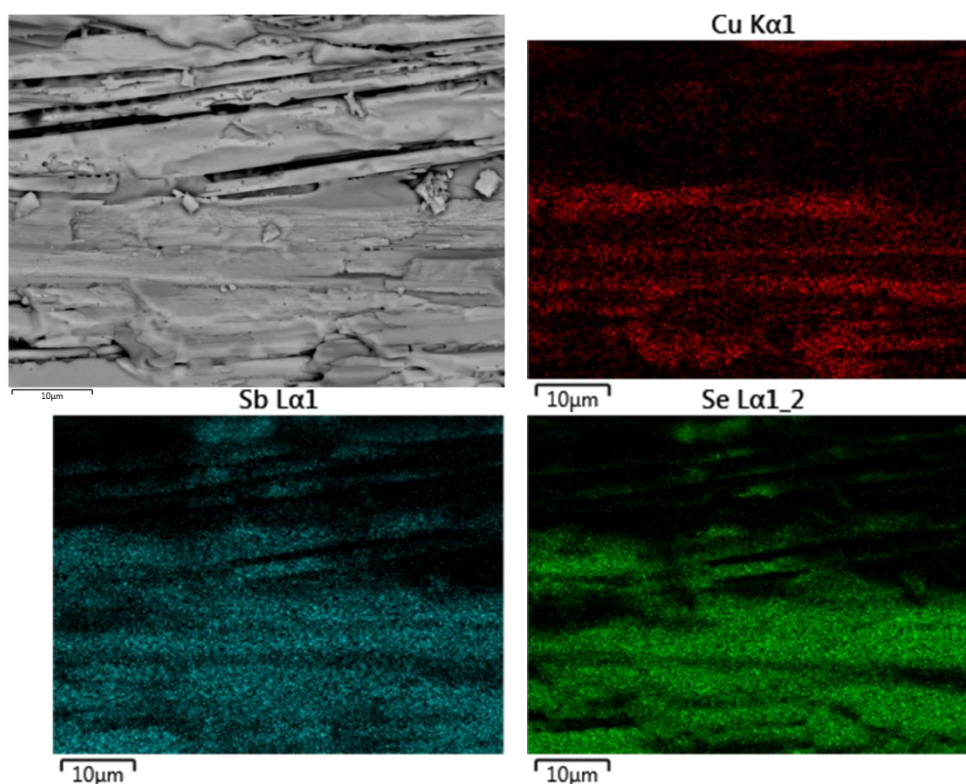


Fig. 3.8 SEM image and EDS elemental mappings of the ceramic $40\text{Cu}_3\text{SbSe}_4\text{-}60\text{Sb}_2\text{Se}_3$ (without I)

3.3.3 Preparation and properties of $40[(\text{Cu}, \text{CuI})_3(\text{Sb}, \text{Sn})\text{Se}_4]\text{-}60\text{Sb}_2\text{Se}_3$ ceramics

It has been well studied and confirmed that the metal doping could significantly improve the conductivity of Cu_3SbSe_4 [21, 22]. Like the doping with bore in silicon, leading to p-type semiconductor, we chose the tin element to substitute partially antimony in the Cu_3SbSe_4 phase to get a more p-type semiconductor and to improve its conductivity. Here we still chose the ceramic of $40\text{Cu}_3\text{SbSe}_4\text{-}60\text{Sb}_2\text{Se}_3$ as the base ceramic and tin is introduced with or without the presence of iodine. 10% of Sb in Cu_3SbSe_4 was substituted by tin in terms of atomic fraction, leading to the ceramics of $40\text{Cu}_3\text{Sb}_{0.9}\text{Sn}_{0.1}\text{Se}_4\text{-}60\text{Sb}_2\text{Se}_3$ and $40(0.9\text{Cu}+0.1\text{CuI})_3\text{Sb}_{0.9}\text{Sn}_{0.1}\text{Se}_4\text{-}60\text{Sb}_2\text{Se}_3$.

Fig. 3.9 shows the XRD patterns of the $40\text{Cu}_3\text{SbSe}_4\text{-}60\text{Sb}_2\text{Se}_3$, $40\text{Cu}_3\text{Sb}_{0.9}\text{Sn}_{0.1}\text{Se}_4\text{-}60\text{Sb}_2\text{Se}_3$ and $40(0.9\text{Cu}+0.1\text{CuI})_3\text{Sb}_{0.9}\text{Sn}_{0.1}\text{Se}_4\text{-}60\text{Sb}_2\text{Se}_3$. We can find that the introduction of the tin and the iodine doesn't give rise to a new crystal phase. The

Cu_3SbSe_4 and Sb_2Se_3 are still the main phases which indicate that we can manage to introduce tin and iodine in the lattice of these two phases without creating new phases. The absence of new phase is a good news as it confirms the doping of Cu_3SbSe_4 and Sb_2Se_3 . The influence of Sn or/and iodine addition on the two crystalline phases need to be studied more in detail in the future.

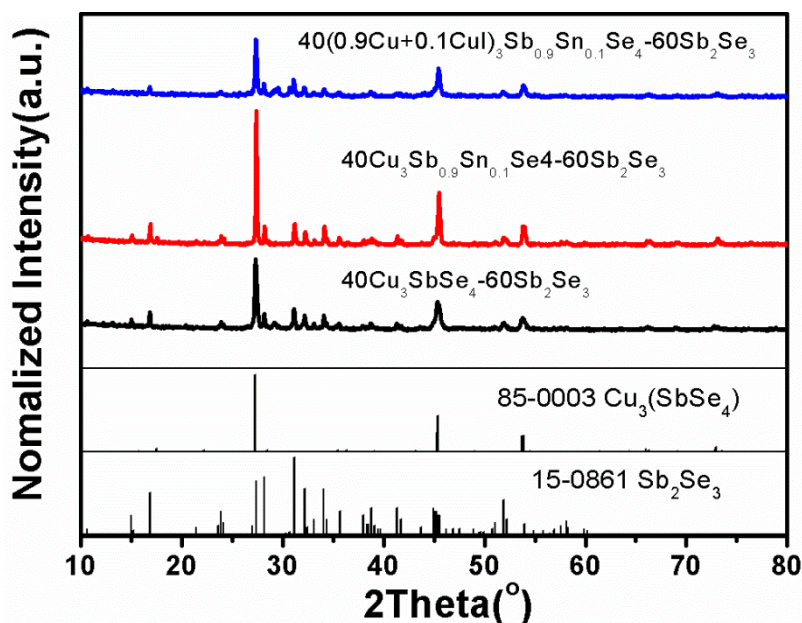


Fig. 3.9 XRD patterns of the $40\text{Cu}_3\text{SbSe}_4\text{-}60\text{Sb}_2\text{Se}_3$, $40\text{Cu}_3\text{Sb}_{0.9}\text{Sn}_{0.1}\text{Se}_4\text{-}60\text{Sb}_2\text{Se}_3$ and $40(0.9\text{Cu}+0.1\text{CuI})_3\text{Sb}_{0.9}\text{Sn}_{0.1}\text{Se}_4\text{-}60\text{Sb}_2\text{Se}_3$ ceramics

Fig. 3.10 shows the photoelectric properties of two ceramics with Sn or/and I addition. The $40\text{Cu}_3\text{Sb}_{0.9}\text{Sn}_{0.1}\text{Se}_4\text{-}60\text{Sb}_2\text{Se}_3$ ceramic indicates a p-type semiconducting behavior by displaying a photocurrent of about $20 \mu\text{A}/\text{cm}^2$ at -0.6 V . We can discover that the current-voltage curve climbs quickly at positive bias and reach a relatively high value which is probably due to a bad preparation of the sample, leading to a slight short-cut between the electric wire (back contact of the sample) and the electrolyte.

The $40(0.9\text{Cu}+0.1\text{CuI})_3\text{Sb}_{0.9}\text{Sn}_{0.1}\text{Se}_4\text{-}60\text{Sb}_2\text{Se}_3$ ceramic presents both p-type and n-type semiconducting behaviors, as photocurrent is measured both at positive and negative bias

even though it displays photocurrent signals with very weak intensity at positive bias. It demonstrates that in spite of the participation of tin, the iodine still plays the role of improving the conductivity of Sb_2Se_3 and changing the conductive paths of the ceramics.

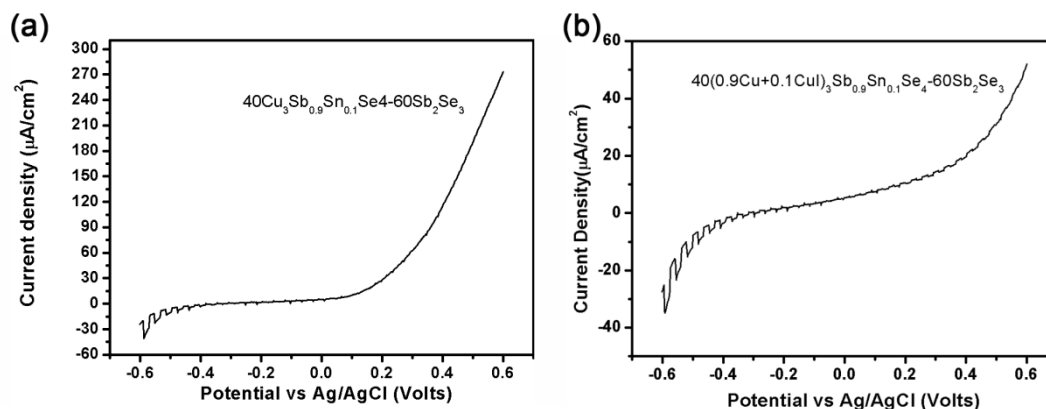


Fig. 3.10 Current-voltage characteristic of the ceramics under chopped illumination lamp (a) $40\text{Cu}_3\text{Sb}_{0.9}\text{Sn}_{0.1}\text{Se}_4\text{-}60\text{Sb}_2\text{Se}_3$ and (b) $40(0.9\text{Cu}+0.1\text{CuI})_3\text{Sb}_{0.9}\text{Sn}_{0.1}\text{Se}_4\text{-}60\text{Sb}_2\text{Se}_3$

3.4 Conclusions

In the present work, we have demonstrated the formation of p-n heterojunctions in the binary $x(0.9\text{Cu}+0.1\text{CuI})_3\text{SbSe}_4\text{-(}100\text{-x)}\text{Sb}_2\text{Se}_3$ ceramics ($x=30, 40, \dots, 70$). The presence of iodine plays a key role determining the photo-electro-chemical properties of the ceramic. It was shown that even small quantities of iodine can increase the conductivity of Sb_2Se_3 by more than 10^5 times. The photo-electro-chemical (PEC) measurements under a chopped light source (400 W.m^{-2}) showed a photocurrent of $50 \mu\text{A/cm}^2$ at the bias of -0.6 V which is much higher than the two semiconducting phases separately. The p-n junction interface was directly observed by means of TEM and EDS. This study indicates that Cu_3SbSe_4 can substitute the Cu_2GeSe_3 to form heterojunctions with Sb_2Se_3 , leading to efficient charge separation and transport.

Some other modifications based on this system have also been tried, especially by substituting partially Sb by Sn with and without the presence of iodine which always plays an important role similar to its role in other systems studied earlier. It is interesting to notice that these doping do not create new phases, indirectly confirming that the Sn and I go inside the

existing crystalline phases. The detailed influence of these additions on the structure is still to be studied in order to find compositions with superior photoelectric properties.

3.5 References

- [1] Laurent Calvez, Mathieu Roze, Yannick Ledemi, Hong-Li Ma, Jacques Lucas, Mathieu Allix, Guy Matzen and Xiang-Hua Zhang, *Controlled crystallization in Ge-(Sb/Ga)-(S/Se)-MX glasses for infrared applications*. Journal of the Ceramic Society of Japan, **116**(1358) (2008) 1079-1082.
- [2] SZ Zhu, HL Ma, M Matecki, XH Zhang, JL Adam and J Lucas, *Controlled crystallization of $\text{GeS}_2\text{-Sb}_2\text{S}_3\text{-CsCl}$ glass for fabricating infrared transmitting glass-ceramics*. Journal of non-crystalline solids, **351**(40) (2005) 3309-3313.
- [3] Xianghua Zhang, Yang Xu, Qianhong Shen, Bo Fan, Xusheng Qiao, Xianping Fan, Hui Yang, Qun Luo, Laurent Calvez and Hongli Ma, *Enhancement of charge photo-generation and transport via an internal network of $\text{Sb}_2\text{Se}_3/\text{Cu}_2\text{GeSe}_3$ heterojunctions*. Journal of Materials Chemistry A, **2**(40) (2014) 17099-17106.
- [4] Chongyin Yang, Fuqiang Huang, Liming Wu and Ke Xu, *New stannite-like p-type thermoelectric material Cu_3SbSe_4* . Journal of Physics D: Applied Physics, **44**(29) (2011) 295404.
- [5] Kriti Tyagi, Bhasker Gahtori, Sivaiah Bathula, Vijaykumar Toutam, Sakshi Sharma, Niraj Kumar Singh and Ajay Dhar, *Thermoelectric and mechanical properties of spark plasma sintered Cu_3SbSe_3 and Cu_3SbSe_4 : promising thermoelectric materials*. Applied Physics Letters, **105**(26) (2014) 261902.
- [6] TH Zou, XY Qin, D Li, GL Sun, YC Dou, QQ Wang, BJ Ren, J Zhang, HX Xin and YY Li, *Simultaneous enhancement in thermoelectric power factor and phonon blocking in hierarchical nanostructured $\beta\text{-Zn}_4\text{Sb}_3\text{-Cu}_3\text{SbSe}_4$* . Applied Physics Letters, **104**(1) (2014) 013904.

- [7] Eric J Skoug, Jeffrey D Cain and Donald T Morelli, *Structural effects on the lattice thermal conductivity of ternary antimony-and bismuth-containing chalcogenide semiconductors*. Applied Physics Letters, **96**(18) (2010) 181905.
- [8] Yongsheng Zhang, Eric Skoug, Jeffrey Cain, Vidvuds Ozoliņš, Donald Morelli and Christopher Wolverton, *First-principles description of anomalously low lattice thermal conductivity in thermoelectric Cu-Sb-Se ternary semiconductors*. Physical Review B, **85**(5) (2012) 054306.
- [9] Kriti Tyagi, Bhasker Gahtori, Sivaiah Bathula, AK Srivastava, AK Shukla, Sushil Auluck and Ajay Dhar, *Thermoelectric properties of Cu_3SbSe_3 with intrinsically ultralow lattice thermal conductivity*. Journal of Materials Chemistry A, **2**(38) (2014) 15829-15835.
- [10] Yubo Zhang, Lili Xi, Youwei Wang, Jiawei Zhang, Peihong Zhang and Wenqing Zhang, *Electronic properties of energy harvesting Cu-chalcogenides: p - d hybridization and d -electron localization*. Computational Materials Science, **108**((2015) 239-249.
- [11] Dat Do, Vidvuds Ozolins, Subhendra D Mahanti, Mal-Soon Lee, Yongsheng Zhang and Christopher Wolverton, *Physics of bandgap formation in Cu-Sb-Se based novel thermoelectrics: the role of Sb valency and Cu d levels*. Journal of Physics: Condensed Matter, **24**(41) (2012) 415502.
- [12] Saburo Endo, Ichiro Sudo and Taizo Irie, *On the Electrical and Thermal Properties of Ternary Chalcogenides $A_2^I B^{IV} X_3$, $A^I B^V X_2$ and $A_3^I B^V X_4$ ($A^I = \text{Cu}$; $B^{IV} = \text{Ge, Sn}$; $B^V = \text{Sb}$; $X = \text{S, Se, Te}$) III. Electrical Properties of Cu_2GeSe_3* . Japanese Journal of Applied Physics, **10**(2) (1971) 218.
- [13] W Procarione and C Wood, *The optical properties of Sb_2Se_3 & Sb_2Te_3* . physica status solidi (b), **42**(2) (1970) 871-878.
- [14] Meiyong Leng, Miao Luo, Chao Chen, Sikai Qin, Jie Chen, Jie Zhong and Jiang Tang, *Selenization of Sb_2Se_3 absorber layer: An efficient step to improve device performance of $\text{CdS}/\text{Sb}_2\text{Se}_3$ solar cells*. Applied Physics Letters, **105**(8) (2014) 083905.
- [15] Néstor Guijarro, Thierry Lutz, Teresa Lana-Villarreal, Flannan O'Mahony, Roberto Gómez and Saif A Haque, *Toward antimony selenide sensitized solar cells: efficient charge*

photogeneration at spiro-OMeTAD/Sb₂Se₃/metal oxide heterojunctions. The journal of physical chemistry letters, **3**(10) (2012) 1351-1356.

[16] Shuo Chen, Xvsheng Qiao, Fengxia Wang, Qun Luo, Xianghua Zhang, Xia Wan, Yang Xu and Xianping Fan, *Facile synthesis of hybrid nanorods with the Sb₂Se₃/AgSbSe₂ heterojunction structure for high performance photodetectors*. Nanoscale, **8**(4) (2016) 2277-2283.

[17] Guang-Yi Chen, Bin Dneg, Guo-Bin Cai, Tie-Kai Zhang, Wen-Fei Dong, Wan-Xi Zhang and An-Wu Xu, *The fractal splitting growth of Sb₂S₃ and Sb₂Se₃ hierarchical nanostructures*. The Journal of Physical Chemistry C, **112**(3) (2008) 672-679.

[18] Adrian W Bott, *Electrochemistry of semiconductors*. Current Separations, **17**((1998) 87-92.

[20] Yang Xu, Bo Fan, Xianghua Zhang, Qianhong Shen, Minjia Wang and Hongli Ma, *Crystallization optimization of the 40GeSe₂–40Sb₂Se₃–20CuI glass for improvement of photoelectric properties*. Journal of Non-Crystalline Solids, **431**((2016) 61-67.

[21] X. Y. Li, D. Li, H. X. Xin, J. Zhang, C. J. Song and X. Y. Qin, *Effects of bismuth doping on the thermoelectric properties of Cu₃SbSe₄ at moderate temperatures*. Journal of Alloys and Compounds, **561**((2013) 105-108.

[22] D. Li, R. Li, X. Y. Qin, C. J. Song, H. X. Xin, L. Wang, J. Zhang, G. L. Guo, T. H. Zou, Y. F. Liu and X. G. Zhu, *Co-precipitation synthesis of nanostructured Cu₃SbSe₄ and its Sn-doped sample with high thermoelectric performance*. Dalton Trans, **43**(4) (2014) 1888-96.

Chapter IV: Synthesis of CuSe nanoparticles and single-crystalline two-dimensional nanoplatelets

4.1 Introduction

Recently, extensive attention has been paid to the preparation and characterization of metal-selenides mostly due to their unique electronic properties such as high concentration and mobility of electrons and temperature tunable band-gap [1-6]. These properties are of crucial importance for the design of nanoscale electronic components operating in near infrared [7, 8]. Since the early 1960s, thin-film chalcogenides such as Cu_xS – CdS , Cu_xSe – CdSe , and Cu_xTe – CdTe have already been studied for fabricating solar cells [9, 10] and copper chalcogenides have been considered as one important photovoltaic material.

Copper selenides (CS) is a particularly interesting class of materials due to its ability to form various stoichiometric and nonstoichiometric compounds. For instance, Riha et al. showed the possibility of tuning the electronic structure thanks to the controllable surface oxidation of Cu_2Se (copper rich) nanoparticles, which allows a transition from Cu_2Se monoclinic crystal cell to $\text{Cu}_{1.8}\text{Se}$ cubic cell [11]. A detailed description of the Cu_2Se crystal structure can be found elsewhere [12, 13]. At the same time, CuSe_2 (copper poor) compounds were studied as a possible anion conductors due to the dominant chalcogen character at the Fermi level and consequent absence of electronic correlation inherent in copper rich compounds [14]. Between copper rich and copper poor compounds, a variety of stable and metastable phases such as Cu_7Se_4 , Cu_3Se_2 , CuSe exist in different crystallographic forms: orthorhombic, cubic, tetragonal, hexagonal etc [15]. It has been reported that copper selenides are p-type semiconductors whose thermal stability and band gap strongly depend on the stoichiometry and phase [16, 17].

The tunability of the electronic properties upon the stoichiometry opens a vast field of possible applications such as solar cells, optical filters, nanoswitches, thermoelectric and photoelectric energy convertors, superconductors [18-23]. For example, with good electrical properties and an inherently complex crystal structure, Cu_{2-x}Se is a potential “phonon glass electron crystal” thermoelectric material that has previously not attracted much interest. Xingxing Xiao et al. have synthesized Cu_{2-x}Se ($0 \leq x \leq 0.25$) compounds by a melting-quenching method, which were then sintered by spark plasma sintering to obtain bulk materials. The thermoelectric properties of Cu_{2-x}Se were investigated and very interesting results have been obtained[24].

Many attempts to prepare copper selenides nanomaterials in different stoichiometries and morphologies have been reported, such as particles[25], wires[26], tubes[27], and flake-like structures[28]. Synthesis route involving thermal decomposition of $\text{Cu}(\text{Se}=\text{CNEt}_2)_2$ in refluxing 4-ethylpyridine solutions has been described [29]. Platelet shaped nanostructures of CuSe have been also synthesized through solution phase reaction [30, 31]. The solution-phase synthetic method for CuSe was successfully utilized to obtain nanoplates[32]. Chemical reaction involved in the synthesis is the reduction of copper selenite with hydrazine hydrate. The reaction is performed in various solvents and in the presence of different capping agents. Single crystalline Cu_{2-x}Se nanowires with lengths up to 50 μm are synthesized via a modified composite hydroxide mediated method[33]. On the other hand, the surfactant-thermal method for synthesis of metal chalcogenides attracted also attention. It was shown by W.W.Xiong et al. that the surfactant media could serve as a cheaper and multifunctional analogue of the ionic liquids, demonstrating the possibility of obtaining metal-chalcogenide quantum dots, quantum wires, nanoplates and bulk crystals in a wide variety of stoichiometries by changing synthesis time and surfactant solvent [34-36]. This method has demonstrated its efficiency also for the synthesis of complex quaternary two-dimensional chalcogenides for photocatalytic and photovoltaic applications[37, 38].

However, the above mentioned and widely used methods either use toxic compounds or are complicated, time-consuming or energy inefficient. In this chapter, we report a new rapid-injection approach to prepare CuSe nanoplates with high quality single-crystalline and two dimensional nanostructure. The forming mechanism of two-dimensional structure from nanoparticles will be proposed. To the best of our knowledge, this is the first report of this particular synthesis route for CuSe nanoplates which match the primitive hexagonal phase. This study opens a new way for energy-efficient, environment friendly and low cost controllable synthesis of binary chalcogenides.

4.2 Experimental procedure

4.2.1 Synthesis of the Cu_xSe nanocrystals

Synthesis of uniform nanocrystals is very important because the size uniformity of an ensemble of nanocrystals is directly related to the homogeneity of their chemical and physical properties. Classical theory suggests that burst nucleation and diffusion-controlled growth are

the most important factors for the control of the size distribution in colloidal synthesis[39]. To understand how the nucleation process influences the size distribution of the crystal particles, a reaction system is considered (shown in Fig. 4.1), where homogeneous nucleation occurs, nucleation occurs randomly all the time during the crystallization process and all of the particles have different growth histories. This results in a uncontrolled growth of the particles and a broad size distribution. On the other hand, an ideal case is depicted wherein all of the particles nucleate at the same time and grow under the same conditions. In such a case, all of the particles would have the same growth history and the size distribution would become monodisperse. The homogeneous nucleation reaction has a very high energy barrier and an extremely high supersaturation level is required to commence the homogeneous nucleation process in the solution. Once started, nucleation and the subsequent growth of particles lower the supersaturation level rapidly. Consequently, the nucleation process terminates by itself. Due to this self-regulating nature of the homogeneous nucleation process, it takes place only for a short moment when the supersaturation level remains very high. This short duration of the homogeneous nucleation process, or “burst nucleation” is very close to the ideal single nucleation event[39, 40].

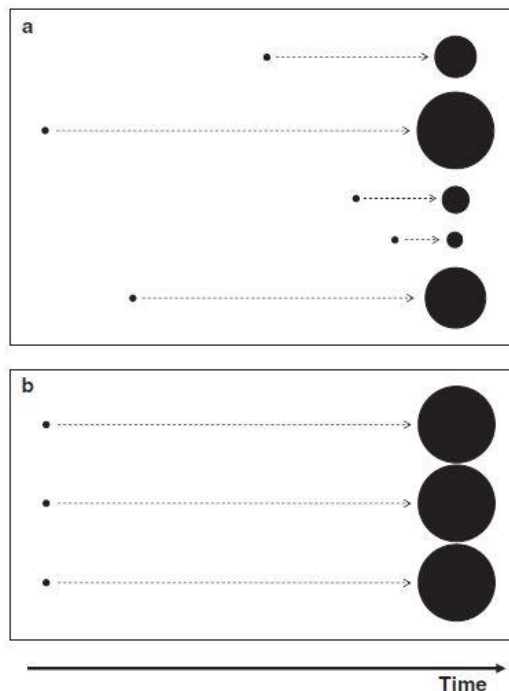


Fig. 4.1 Schematics for the crystallization reaction systems in which homogeneous nucleation occurs randomly (a) and at the same time (b) The dots (•) on the left of the

arrows indicate the formation of nuclei. Each arrow and black circle shows the growth of the corresponding particle over time

In the last two decades, numerous reports on the synthesis of uniform nanocrystals have popularized two major synthetic methods, namely, hot-injection and heat-up, to obtain uniform nanocrystals of various materials including metals, semiconductors and oxides. For chalcogenide nanocrystals synthesis, the method named hot-injection was chosen which involved the injection of a “cold” (room temperature) solution of precursor molecules into hot liquid. Hot injection leads to instantaneous nucleation, quenched by fast cooling of the reaction mixture[39, 41]. The hot-injection organometallic synthesis method proved to be highly versatile and was adapted to prepare other nanocrystal compounds of II-VI, IV-VI and III-V semiconductors. The schematic diagram of chalcogenide nanocrystals preparation by hot-injection process is shown in Fig. 4.2.

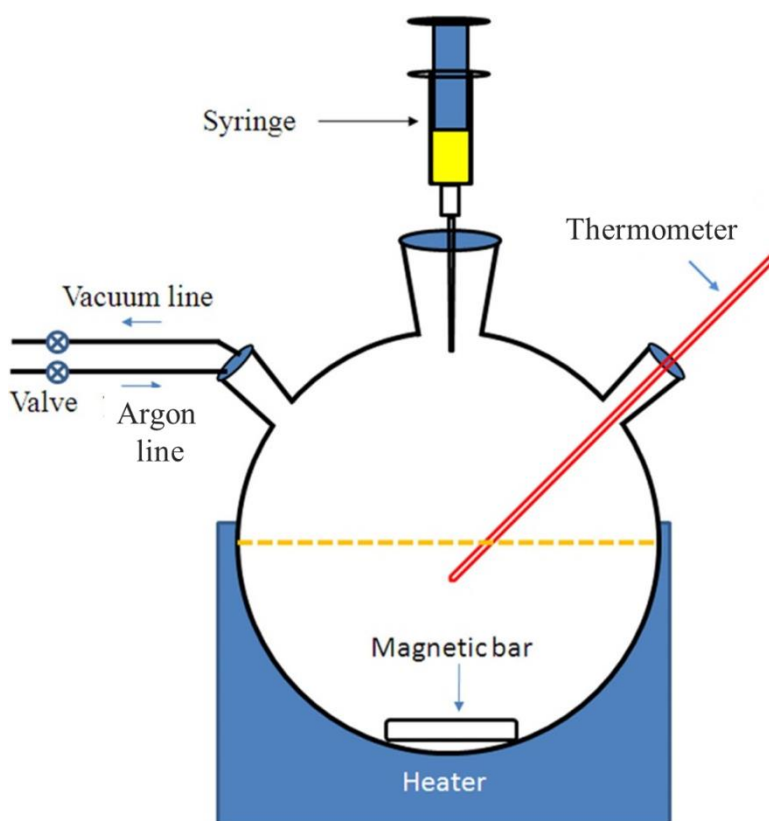
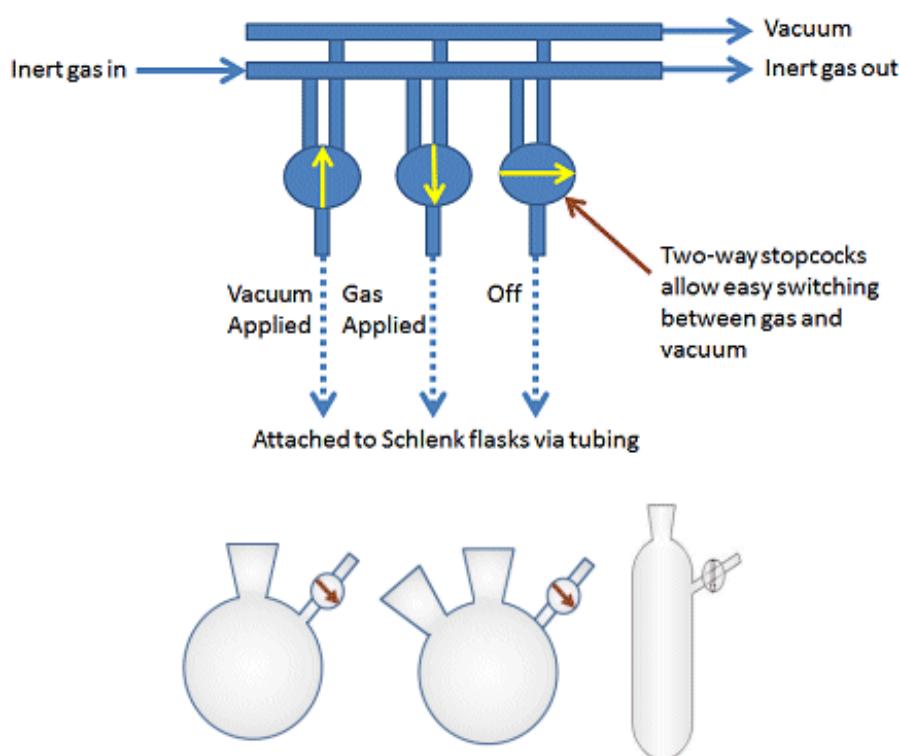


Fig. 4.2 Schematic diagram of hot-injection synthesis

Since our reaction is sensitive to moisture and oxygen, the schlenk line is chosen to be connected with the reaction system as shown in Fig. 4.3. The schlenk line is a commonly used chemistry apparatus developed by Wilhelm Schlenk. It consists of a dual manifold with several ports. One manifold is connected to a source of purified inert gas, while the other is connected to a vacuum pump. The inert-gas line is vented through an oil bubbler, while solvent vapors and gaseous reaction products are condensed in a liquid-nitrogen or dry-ice/acetone cold trap, preventing then the contamination of the vacuum pump. Special stopcocks or Teflon taps allow vacuum or inert gas to be selected without the need for placing the sample on a separate line.. Before the reaction, the air inside the Schlenk is expelled by flow of argon gas with higher density. To remove oxygen, water and other volatile impurities in the solution, a preheating process is added in our reaction process.

**Fig. 4.3 Schematic diagram of the Schlenk lines**

The Cu_xSe nanocrystals (NCs) were produced via the hot injection approach [42] by reacting CuCl₂.2H₂O and Al(NO₃)₃ 9H₂O with an excess of selenium precursor in the presence of hexadecylamine (HDA). In a typical preparation, 1.5 mmol CuCl₂.2H₂O (0.256g, 99.99%, aladdin), 0.3 mmol Al(NO₃)₃ 9H₂O (0.113g, 98%, aladdin) , 15 mmol HDA (3.622g, 90%, aladdin) and 30 mL octadecene (ODE, 90%, Aldrich) were introduced inside a three-neck flask and heated to 200 °C under argon flow until all precursors were dissolved.

Afterwards, the obtained yellowish transparent solution was cooled to different reaction temperatures and maintained under Ar flow for half an hour to remove oxygen, water and other volatile impurities. Then 12 mL ODE-Se (0.8 M) solution which was prepared by dissolving SeO₂ in ODE solution of corresponding volume at 200 °C for 6 hr under Ar flow was rapidly injected through a syringe. The excess selenium leads to the instantaneous formation of nuclei of cationic selenide, guarantees the uniformity of grain size and prevents the crystal growth during the grain nucleation. And it can also insure a complete reaction. The mixture was maintained at reaction temperature for different time. Afterwards, the solution was rapidly cooled down to room temperature in air. The generation of nanocrystalline Cu_xSe was evidenced by the color change of the mixture from an initial light orange to eventually deep green color of the solution. To remove the weakly bound HDA, 9 ml of oleic acid (OA, 90%, Aldrich) was added to the mixture during the cooling step at about 70 °C [42]. And finally the nanocrystals were isolated and purified using chloroform and isopropanol to complete the standard solvent/non-solvent precipitation/re-dispersion procedure and were dried under vacuum at 40 °C for about 12 hr.

4.2.2 Presentation of the characterization techniques

Transmission electron microscopy (TEM) images were obtained with a Philips CM200 field emission microscope. High resolution transmission electron microscopy (HRTEM) images with selected area electron diffraction (SAED) patterns and Energy Dispersive Spectrometer (EDS) data were obtained with a FEI Tecnai G2 F20 field emission microscope. A Hitachi S-4800 field emission scanning electron microscope was used to observe the morphology. X-ray diffraction (XRD) analysis was carried out on a PANalytical B.V

Empyrean 200895 X-ray diffractometer. UV–VIS absorption spectra were taken with a SHIMADZU UV-3150 spectrophotometer.

4.3 Results and discussion

4.3.1 Influence of reaction temperature on Cu_xSe nanocrystals

It has been well studied that the metal ions have a great influence on the morphology of semiconductor nanoparticles, which is for example the case of aluminum on copper selenides[43, 44]. Therefore, $\text{Al}(\text{NO}_3)_3 \cdot 9\text{H}_2\text{O}$ was introduced into the reaction system at first. Fig 4.4 shows the XRD patterns of the copper selenides nanocrystals which were synthesized at 160 °C, 180 °C and 200 °C for different time with the presence of $\text{Al}(\text{NO}_3)_3 \cdot 9\text{H}_2\text{O}$. In order to determine the best reaction temperature, reaction time was set as 60 min in order to make sure the time is long enough for complete reaction. When the reaction temperature was 160 °C, the clear diffraction peaks corresponding to hexagonal CuSe (Pdf 49-1453) can be observed and neither Se nor other secondary phase was detected. Increasing the temperature to 180 °C leads to more complete reaction with the same purity of phase. However, further temperature raising causes the phase transfer from hexagonal CuSe to hexagonal $\text{Cu}_{0.87}\text{Se}$ (Pdf 83-1814) with several diffraction peaks of impurity phases. In order to ensure a complete reaction with minimized mixed phases, 180 °C was chosen as the reaction temperature.

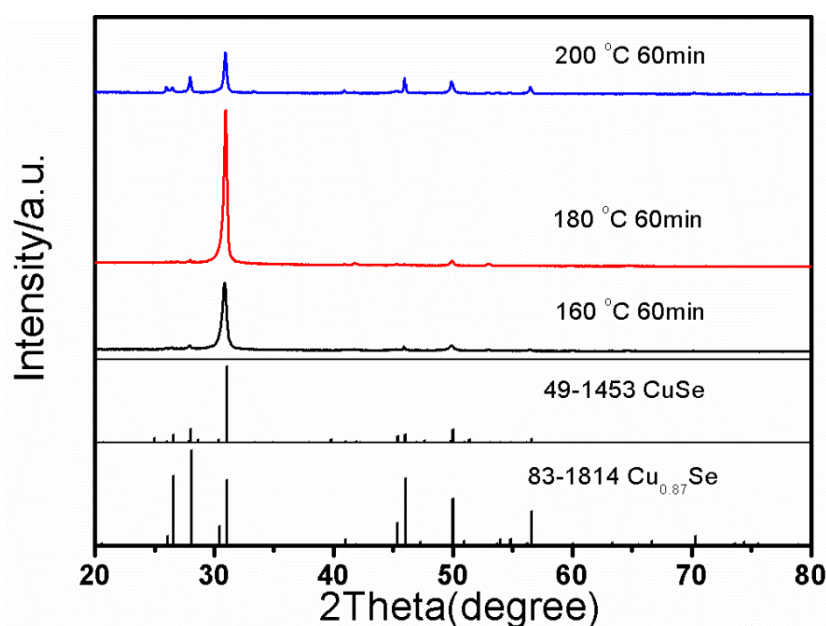


Fig. 4.4 XRD patterns of the copper selenides synthesized at different temperatures (160 °C, 180 °C and 200 °C) for 60min with the presence of $\text{Al}(\text{NO}_3)_3 \cdot 9\text{H}_2\text{O}$

4.3.2 Copper selenides nanocrystals synthesized with the presence of $\text{Al}(\text{NO}_3)_3 \cdot 9\text{H}_2\text{O}$

Fig 4.5 shows the XRD patterns of the copper selenides nanoparticles and nanoplates which were synthesized at 180 °C for different durations of reaction with the presence of $\text{Al}(\text{NO}_3)_3 \cdot 9\text{H}_2\text{O}$. Wide and relatively weak diffraction peaks can be clearly observed for nanocrystals obtained after less than 10 min synthesis. Moreover, their diffraction patterns do not accurately correspond to CuSe JCPDS card. This is due to the presence of the big amount of relatively small nanocrystals with slight deviation from the stoichiometry. Extending of the reaction time up to 60 min leads to the enhancement of (006) diffraction peak corresponding to hexagonal CuSe. The increase of diffraction intensity in several orders of magnitude and the narrowing of the diffraction peaks indicate a rapid growth of CuSe nanocrystals from smaller aggregates. It is worth mentioning that neither Se nor other secondary phase was detected, confirming the high purity of the product.

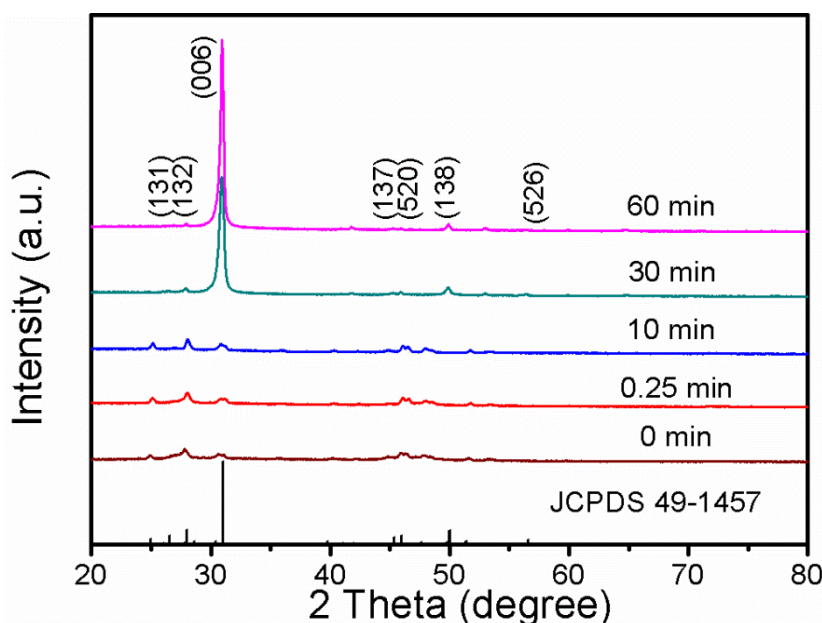


Fig. 4.5 XRD patterns of the copper selenides nanoparticles and nanoplates synthesized at 180 °C for 0 s, 15 s, 10 min, 30 min and 60 min with the presence of $\text{Al}(\text{NO}_3)_3 \cdot 9\text{H}_2\text{O}$

Fig. 4.6 shows the TEM images of the copper selenides nanoparticles and nanoplates which were synthesized at 180 °C for different reaction times with the presence of $\text{Al}(\text{NO}_3)_3 \cdot 9\text{H}_2\text{O}$. The average size of the spherical nanocrystals increased from 10 nm to about 30 nm after 10 min synthesis. These spherical nanocrystals were eventually transformed to regular-shape triangular and hexagonal nanoplates after 60 min synthesis. Fig. 4.6 shows the measured size distribution of the samples obtained with 0 min and 10 min. It confirms that 10 min synthesis was enough to obtain quasi-spherical CuSe nanocrystals with narrow size distribution.

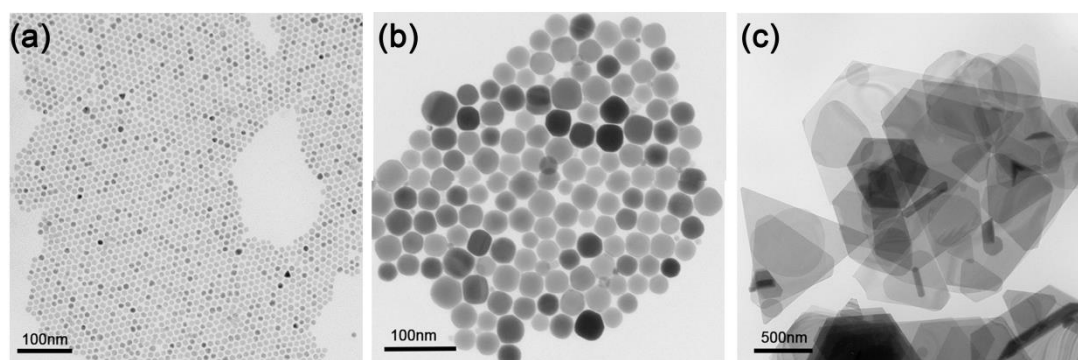


Fig. 4.6 TEM images of copper selenides nanoparticles and nanoplates obtained with different times: (a) 0 min, (b) 10 min, (c) 60 min

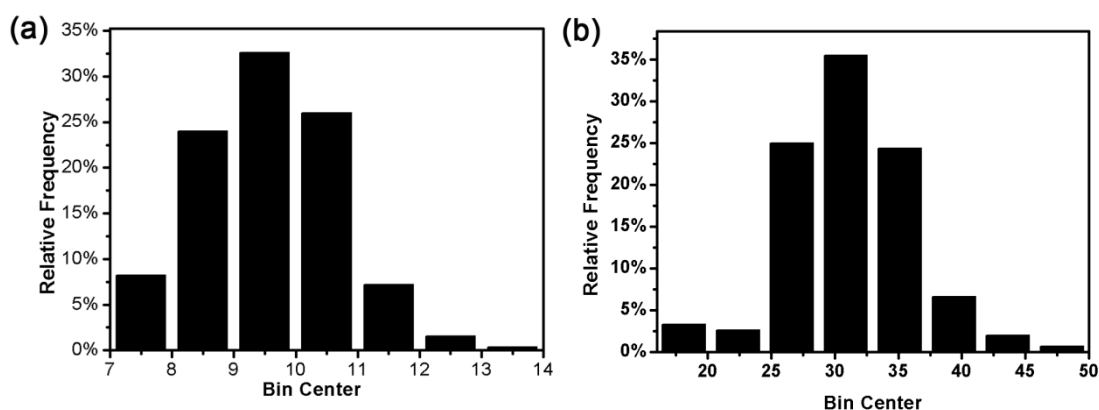


Fig. 4.7 Size distribution of the samples obtained with (a) 0 min and (b) 10 min

The HRTEM images of nanoparticles obtained with 0 min and nanoplates obtained with 60 min are shown in Fig. 4.8 (a) and (b) respectively. It shows that the typical lattice spacing of the CuSe nanoparticles and nanoplates is 3.56 Å, which is in good agreement with the standard value for (220) plane of CuSe hexagonal phase. The SAED pattern (fig 4.8 (c)) demonstrates ordered diffraction spots which can be attributed to the lattice planes of $(01\bar{1}0)$, $(10\bar{1}0)$ and $(1\bar{1}00)$ of primitive hexagonal structure of copper selenide with the zone axis along the (006) plane direction. This indicates that the nanoplates were well crystallized and have a single-crystalline nature.

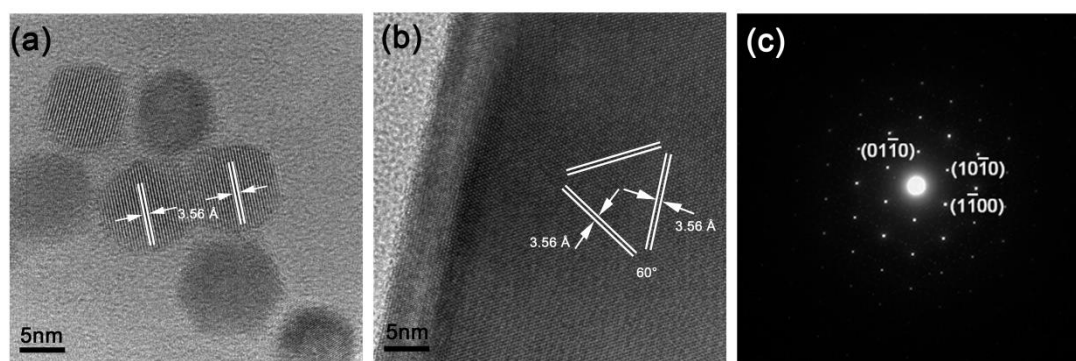


Fig. 4.8 HRTEM images of (a) nanoparticles obtained with 0 min, (b) nanoplates obtained with 60 min and (c) selected area electron diffraction diagrams of nanoplates

Fig 4.9 shows the SEM images of the copper selenides nanoplates which were synthesized at 180 °C for 60 min. Nanocrystals with regular hexagonal and triangle shapes can be seen from this image. These hexagonal plates show thickness of about 50 nm. We observed a wide range of nanoplates' size distribution varying from tens of nanometers to microns.

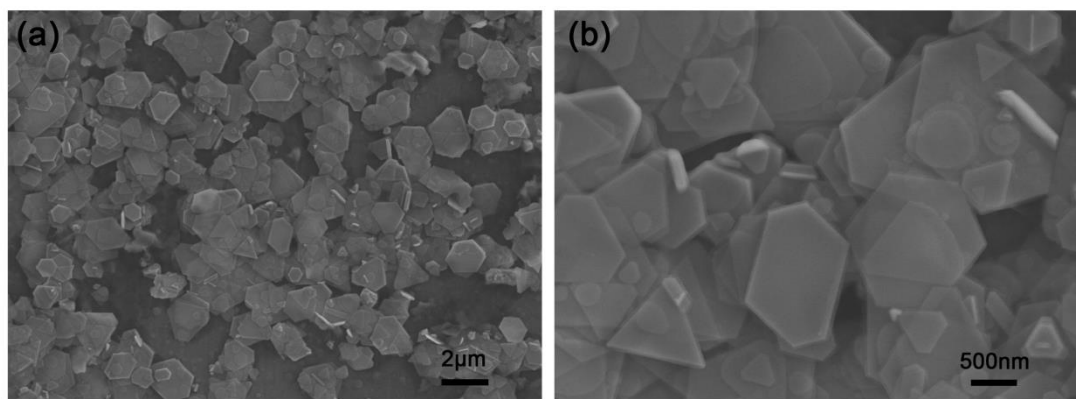


Fig. 4.9 SEM images of copper selenide hexagonal nanoplatelets obtained within 60min

Fig. 4.10 shows energy dispersive spectroscopy (EDS) of the copper selenide nanoparticles and nanoplates which were synthesized at 180 °C for different times with the presence of $\text{Al}(\text{NO}_3)_3 \cdot 9\text{H}_2\text{O}$, which indicated the absence of Al inside the nanoparticles. The presence of Al^{3+} tends to attract not only Cl^- but also negatively charged selenium ions, leading to a slower growth of CuSe nanoplates. From EDS results, it can be estimated that the Cu/Se ratio of the nanoparticles which were synthesized at 180 °C for 0 min was 50/50. The nanoparticles which were synthesized at 180 °C for 10 min show a slight deviation from the stoichiometry (47/53). A significant Se excess with a ratio of 37/63 could be observed for the copper selenide nanoplates which were synthesized at 180 °C for 60 min. However, XRD result (Fig. 4.10) shows that only CuSe hexagonal phase was formed in the nanoplates which were synthesized at 180 °C for 60 min, indicating that nanoplates containing only the CuSe hexagonal phase are formed even in case of Se-excess.

The difference between the EDS composition analysis and the XRD patterns indicates that the nanoplates are composed of certainly hexagonal CuSe and probably also amorphous selenium which cannot be detected by XRD.

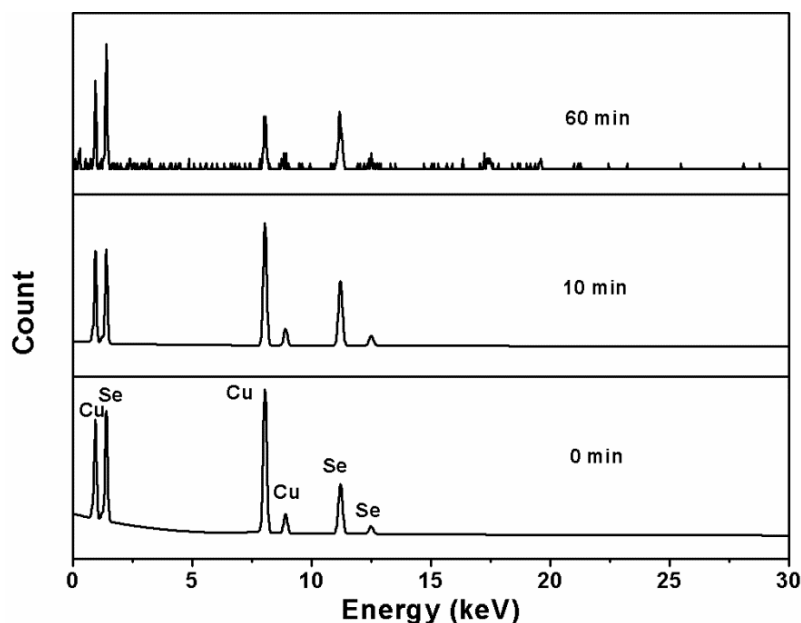


Fig. 4.10 Energy Dispersive spectroscopy(EDS) of copper selenides nanoparticles and nanoplate, synthesized at 180 °C for 0 s, 10 min and 60 min with the presence of $\text{Al}(\text{NO}_3)_3 \cdot 9\text{H}_2\text{O}$

Copper selenide is a well-known p-type semiconductor possessing a direct band gap with E_g depending on the stoichiometry and varying from 1.0 eV to 2.0 eV. [13] According to Chen et al. [8], the Cu vacancies (V_{Cu}) created a shallow acceptor level close to the valence band. This self-doping effect was responsible for p-type conductivity of CuSe. For the elucidation of the electronic properties, UV-VIS-NIR absorption spectra were recorded. Since copper selenide is a direct band semiconductor, the optical absorption data can be calculated from diffuse reflectance data using Kubelka–Munk equations: $F(R)=\alpha/\Lambda=(1-R)^2/(2R)$, where R is the reflectance, α and Λ are the absorption and scattering coefficients, respectively [45]. Fig. 4.11 shows the plots of $[F(R)h\nu]^2$ versus energy ($h\nu$) for the copper selenides nanoparticles and nanoplates which were synthesized at 180 °C for different times. E_g is approximately 1.29eV for 0 min. 1.18eV for 10 min and 1.52eV for 60 min. The red shift for nanocrystals obtained after 10 min reaction can be explained from the point of view of quantum confinement, since the size of 0 min synthesized nanocrystals was about 10 nm, the same order of magnitude as the De Broglie wavelength of a free electron. Therefore, the quantum confinement effect can be significant so as to increase the band gap width of

nanocrystals, compared to a bulk material. Increase of nanocrystal size reduces the influence of quantum confinement on the electronic structure. However, this does not explain the strong blue shift for the 60 min synthesized nanocrystals. In fact, in the above mentioned EDS pattern (Fig 4.9), one can see that 60 min synthesized nanocrystals possess an excess of Se, which can lead to the formation of Se_{Cu} type of defects. The increase of the electronegative element (Se) in a CuSe crystal cell in its turn causes significant widening of the band gap. This result provides a possibility of controlling the E_g simply by controlling the synthesized time.

The excess of Se in the CuSe crystals can explain the widening of the band gap width and is confirmed by the EDS measurements. However, if this is the case, the lattice parameter of CuSe should change and this is not supported by the XRD results. More detailed study is still needed to elucidate the nanostructure of these CuSe nanoparticles or nanoplates.

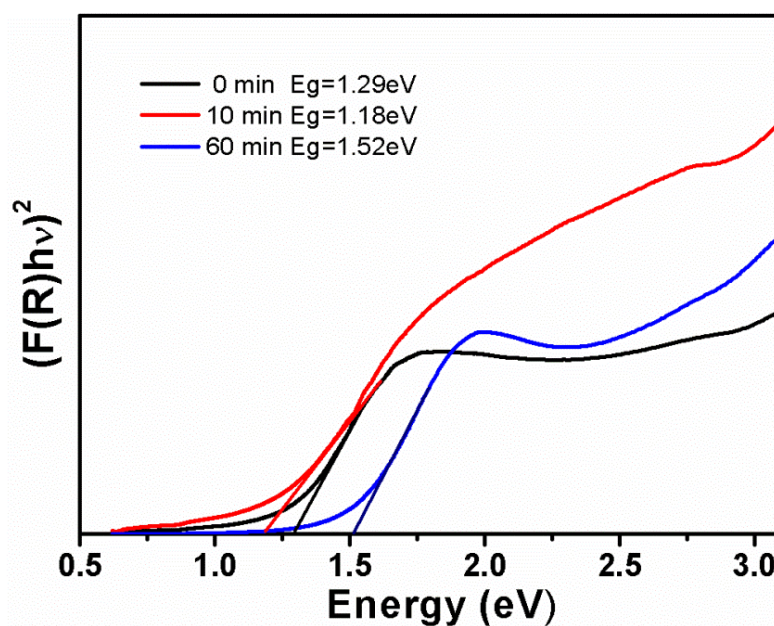


Fig. 4.11 Absorption spectra of the copper selenides nanoparticles and nanoplates, synthesized at 180 °C for 0s, 10min and 60min

In order to determine the role of Al^{3+} in CuSe nanocrystals growth, the copper selenide nanoparticles and nanoplates were synthesized in the absence of $\text{Al}(\text{NO}_3)_3 \cdot 9\text{H}_2\text{O}$. Fig 4.12 shows the XRD patterns of the copper selenide nanoparticles and nanoplates synthesized at

180 °C for different times without the presence of $\text{Al}(\text{NO}_3)_3 \cdot 9\text{H}_2\text{O}$. The 0 min synthesized sample corresponds to an unknown phase and consists of a big amount of small crystals. However, obvious (006) diffraction peak corresponding to CuSe hexagonal phase can be observed in the 10 min synthesized sample, which indicated a rapid growth of hexagonal CuSe crystals in the absence of $\text{Al}(\text{NO}_3)_3 \cdot 9\text{H}_2\text{O}$.

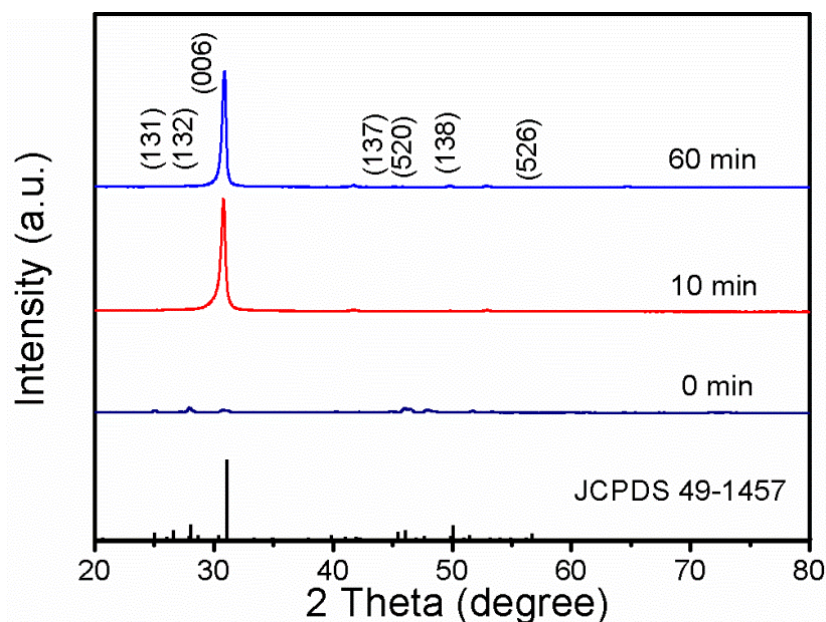


Fig. 4.12 XRD patterns of the copper selenide nanoparticles and nanoplates synthesized at 180 °C for 0s, 10min and 60min without the presence of $\text{Al}(\text{NO}_3)_3 \cdot 9\text{H}_2\text{O}$

Fig. 4.13 shows the TEM images of the copper selenide nanoparticles and nanoplates synthesized at 180 °C for different times always without the presence of $\text{Al}(\text{NO}_3)_3 \cdot 9\text{H}_2\text{O}$. The 0 min synthesized sample shows the regular spherical nanoparticles with narrow size distribution and the size is similar to that obtained with the presence of aluminum nitrate (figure 4.6 and fig. 4.8). These spherical nanoparticles were rapidly transformed to regular-shape triangular and hexagonal CuSe nanoplates only after 10 min synthesis, which confirms that the absence of Al^{3+} leads to faster growth of CuSe nanoplates.

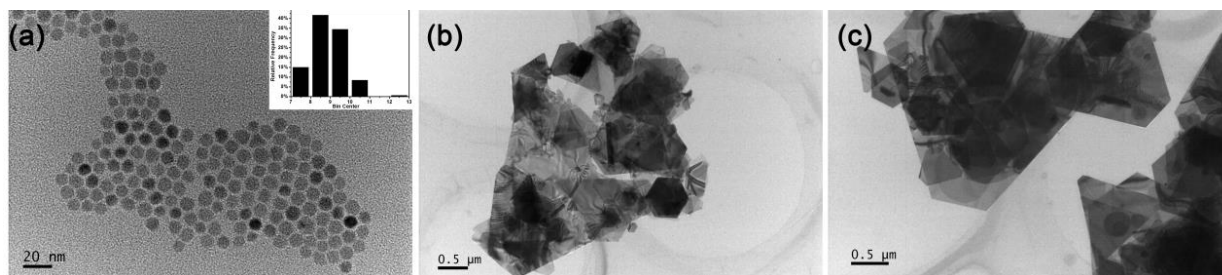


Fig. 4.13 TEM images of copper selenides nanoparticles and nanoplates obtained with different reaction time without the presence of $\text{Al}(\text{NO}_3)_3 \cdot 9\text{H}_2\text{O}$: (a) 0 min, (b) 10 min, (c) 60 min

4.3.3 Growth mechanism of CuSe single-crystalline two-dimensional nanoplatelets

It was demonstrated that spherical nanoparticles were formed initially and then these particles are progressively aggregated together to form triangular and hexagonal nanoplates. The likely mechanism of nanoplates assembly is proposed in fig. 4.14. Oriented attachment involves spontaneous self-organization including rotation and migration of adjacent particles to share a common crystallographic orientation, followed by joining of these particles at a planar interface [46, 47]. Aggregation of nanocrystals in nanoplates is energetically beneficial since it reduces the overall length of nanocrystal-ligand interface and therefore leads to the reduction of Gibbs energy by removing surface-associated states. As it can be seen from HRTEM image of the intermediate product (Fig. 4.7(a)), the nanocrystals evidently demonstrate mutual orientation and aggregation according to the oriented attachment mechanism leading to the formation of two-dimensional single crystalline nanoplates.

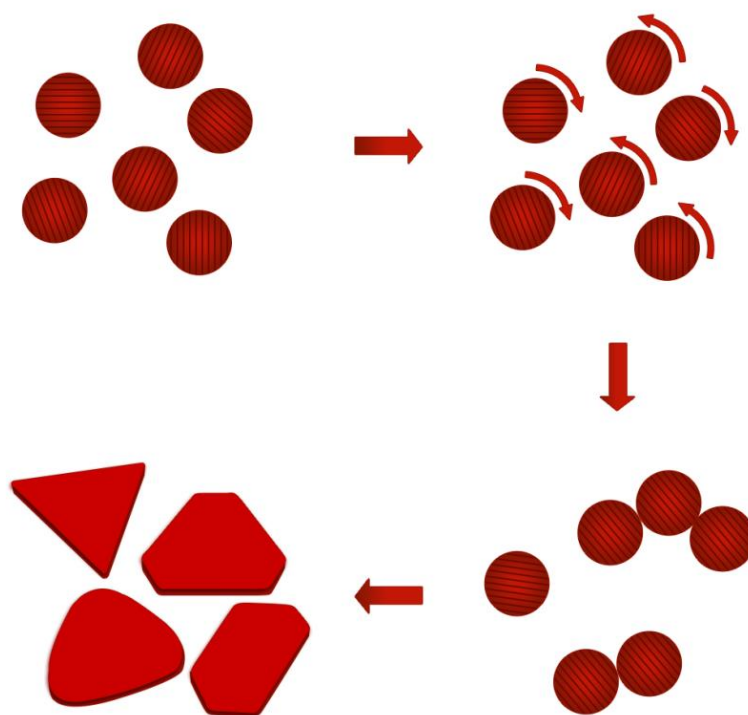


Fig. 4.14 The growth mechanism of copper selenide nanoplates via the “oriented attachment”

4.3.4 Other binary selenides synthesized by hot-injection

This approach of hot-injection is interesting not only for the preparation of copper selenides but also for other binary metal chalcogenides such as CdS, CdSe, PbS, CdSe/ZnS core-shell nanocrystals etc. Therefore, we have tried also to use this method to synthesis other binary metal chalcogenides. Tin selenide is known as a kind of semiconductor of wide interest as it may be used for optoelectronic devices, solar cells, memory switching devices and also anodes for lithium-ion batteries. Usually, tin selenides have two stoichiometric phases, SnSe and SnSe₂. Tin(II) selenide adopts a layered orthorhombic crystal structure at room temperature and has demonstrated the ability to convert waste heat into electrical energy[48]. SnSe₂ has a hexagonal phase and layered structural motif[49, 50]. The layered semiconductor materials are an important class of lithium-storage materials because lithium ions can be inserted and stored between the weakly interacting layers. Solution approach for colloidal tin selenides is as yet quite limited. So here we plan to utilize the method of hot-injection to prepare tin selenides.

The tin selenide nanocrystals were produced by reacting $\text{SnCl}_2 \cdot 2\text{H}_2\text{O}$ and an excess of selenium precursor in the presence of hexadecylamine (HDA). In a typical preparation, 6 mmol $\text{SnCl}_2 \cdot 2\text{H}_2\text{O}$ (1.354g, 99.99%, Aldrich), 60 mmol HDA (14.488g, 90%, Aldrich) and 120 mL octadecene (ODE, 90%, Aldrich) were introduced inside a three-neck flask and heated to 200 °C under argon flow until all precursors were dissolved. Afterwards, the obtained solution was cooled to 180 °C and maintained under Ar flow for half an hour to remove oxygen, water and other volatile impurities. Then 12 mL ODE-Se (0.8 M) solution was rapidly injected through a syringe. The mixture was maintained at 180 °C from 0 min up to 60 min. Afterwards, the solution was rapidly cooled down to room temperature in air. 9 ml of oleic acid (OA, 90%, Aldrich) was added to the mixture during the cooling step at about 70 °C to remove the weakly bound HDA[42]. Finally the nanocrystals were isolated and purified using cyclohexane and ethanol to complete the standard solvent/nonsolvent precipitation/redispersion procedure and were dried under vacuum at 40 °C for about 12 hr.

Fig 4.15 shows the XRD patterns of the tin selenides nanoparticles which were synthesized at 180 °C for different times. It can be seen that there is no crystal phase observed when the reaction time is less than 10 minutes. Extending of the reaction time up to 60 min leads to the appearance of diffraction peaks similar to standard peaks of orthorhombic SnSe.

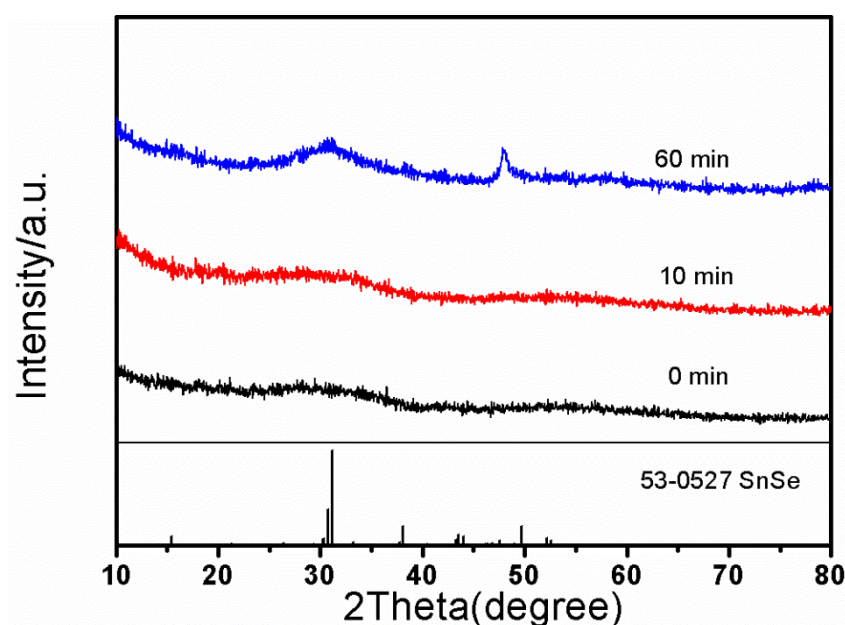


Fig. 4.15 XRD patterns of the tin(II) selenide nanoparticles synthesized at 180 °C for 0s, 10min and 60min

The color of the reaction products changes from yellow of 0min to yellow-brown of 10min. These colors correspond more to SnSe_2 rather than SnSe . Finally, the color turns into steel grey at 60min which is in excellent agreement with the color of tin selenide (SnSe) as show in Fig. 4.16. These are the very preliminary results. The optical and electronic properties of these compounds are under investigation. If the above observation is confirmed, then it would be possible to synthesize tin selenides with different valences of Sn, leading to different optical and electronic properties, just by changing some experimental conditions such as reaction temperature and time.



Fig. 4.16 Photographs of products prepared for different time: (a) 0 min, (b) 10 min and (c) 60 min

4.4 Conclusions

The copper selenide nanoparticles and high-quality single-crystalline two-dimensional hexagonal nanoplatelets have been synthesized by a hot-injection approach. The possible growth mechanism of the nanoplates is based on the “oriented attachment” nanoparticles. During the synthesis process, Al^{3+} ions in the solution have a significant impact on the growth rate of the nanoplates. It is demonstrated that CuSe band gap can be widely tuned simply by modifying the synthesized time. This gives the possibility to adjust this important parameter of this interesting semiconductor according to the targeted applications. This approach of hot-injection has been proven to be very effective for the preparation of other binary metal chalcogenides.

4.5 References

- [1] Mahdiyeh Esmaeili-Zare, Masoud Salavati-Niasari and Azam Sobhani, *Simple sonochemical synthesis and characterization of HgSe nanoparticles*. Ultrasonics sonochemistry, **19**(5) (2012) 1079-1086.
- [2] Mohammad Afzaal and Paul O'Brien, *Recent developments in II–VI and III–VI semiconductors and their applications in solar cells*. Journal of Materials Chemistry, **16**(17) (2006) 1597-1602.
- [3] A Zakutayev, DH McIntyre, G Schneider, R Kykyneshi, DA Keszler, C-H Park and J Tate, *Tunable properties of wide-band gap p-type BaCu (Ch_{1-x}Ch_x) F (Ch= S, Se, Te) thin-film solid solutions*. Thin Solid Films, **518**(19) (2010) 5494-5500.
- [4] M Salavati-Niasari, M Esmaeili-Zare and Azam Sobhani, *Synthesis and characterisation of cadmium selenide nanostructures by simple sonochemical method*. Micro & Nano Letters, **7**(8) (2012) 831-834.
- [5] Chun-Nan Zhu, Peng Jiang, Zhi-Ling Zhang, Dong-Liang Zhu, Zhi-Quan Tian and Dai-Wen Pang, *Ag₂Se quantum dots with tunable emission in the second near-infrared window*. ACS applied materials & interfaces, **5**(4) (2013) 1186-1189.
- [6] Marc-Antoine Langevin, Dany Lachance-Quirion, Anna M Ritcey and Claudine N Allen, *Size-Dependent Extinction Coefficients and Transition Energies of Near-Infrared β -Ag₂Se Colloidal Quantum Dots*. The Journal of Physical Chemistry C, **117**(10) (2013) 5424-5428.
- [7] J Ren, DB Eason, LE Churchill, Z Yu, C Boney, JW Cook, JF Schetzina and NA El-Masry, *Integrated heterostructure devices composed of II–VI materials with Hg-based contact layers*. Journal of crystal growth, **138**(1) (1994) 455-463.
- [8] Ou Chen, Xian Chen, Yongan Yang, Jared Lynch, Huimeng Wu, Jiaqi Zhuang and Y Charles Cao, *Synthesis of metal–selenide nanocrystals using selenium dioxide as the selenium precursor*. Angewandte Chemie International Edition, **47**(45) (2008) 8638-8641.

- [9] DA Cusano, *CdTe solar cells and photovoltaic heterojunctions in II–VI compounds*. Solid-State Electronics, **6**(3) (1963) 217-218.
- [10] J. Lebrun, *Realisation Et Proprietes Des Photopiles Solaires En Couches Minces De Tellurure De Cuivre Et Tellurure De Cadmium*. Revue De Physique Appliquee, **1**(3) (1966) 204-&.
- [11] Shannon C Riha, Derek C Johnson and Amy L Prieto, *Cu₂Se nanoparticles with tunable electronic properties due to a controlled solid-state phase transition driven by copper oxidation and cationic conduction*. Journal of the American Chemical Society, **133**(5) (2010) 1383-1390.
- [12] S Kashida and J Akai, *X-ray diffraction and electron microscopy studies of the room-temperature structure of Cu₂Se*. Journal of Physics C: Solid State Physics, **21**(31) (1988) 5329.
- [13] K Yamamoto and S Kashida, *X-ray study of the average structures of Cu₂Se and Cu_{1.8}S in the room temperature and the high temperature phases*. Journal of Solid State Chemistry, **93**(1) (1991) 202-211.
- [14] Hiroaki Ueda, Minoru Nohara, Koichi Kitazawa, Hidenori Takagi, Atsushi Fujimori, Takashi Mizokawa and Takehiko Yagi, *Copper pyrites CuS₂ and CuSe₂ as anion conductors*. Physical Review B, **65**(15) (2002) 155104.
- [15] Robert Donald Heyding and Ritchie MacLaren Murray, *The crystal structures of Cu_{1.8}Se, Cu₃Se₂, α - and γ -CuSe, CuSe₂, and CuSe₂II*. Canadian Journal of Chemistry, **54**(6) (1976) 841-848.
- [16] ZH Han, YP Li, HQ Zhao, SH Yu, XL Yin and YT Qian, *A simple solvothermal route to copper chalcogenides*. Materials Letters, **44**(6) (2000) 366-369.
- [17] Ansgar Schäfer, Markus Kollwitz and Reinhart Ahlrichs, *Electronic excitation energies in copper selenide clusters*. The Journal of chemical physics, **104**(18) (1996) 7113-7121.
- [18] PK Nair, MTS Nair, VM Garcia, OL Arenas, Y Pena, A Castillo, IT Ayala, O Gomezdaza, A Sanchez and J Campos, *Semiconductor thin films by chemical bath deposition*

for solar energy related applications. Solar Energy Materials and Solar Cells, **52**(3) (1998) 313-344.

[19] MA Korzhuev, *Dufour effect in superionic copper selenide*. Physics of the Solid State, **40**(2) (1998) 217-219.

[20] PP Hankare, VM Bhuse, KM Garadkar, SD Delekar and IS Mulla, *Low temperature route to grow polycrystalline cadmium selenide and mercury selenide thin films*. Materials chemistry and physics, **82**(3) (2003) 711-717.

[21] HM Pathan and CD Lokhande, *Deposition of metal chalcogenide thin films by successive ionic layer adsorption and reaction (SILAR) method*. Bulletin of Materials Science, **27**(2) (2004) 85-111.

[22] D Lippkow and H-H Strehblow, *Structural investigations of thin films of copper-selenide electrodeposited at elevated temperatures*. Electrochimica Acta, **43**(14) (1998) 2131-2140.

[23] VM Bhuse, PP Hankare, KM Garadkar and AS Khomane, *A simple, convenient, low temperature route to grow polycrystalline copper selenide thin films*. Materials chemistry and physics, **80**(1) (2003) 82-88.

[24] Xiao Xing-Xing, Xie Wen-Jie, Tang Xin-Feng and Zhang Qing-Jie, *Phase transition and high temperature thermoelectric properties of copper selenide $Cu_{2-x}Se$ ($0 \leq x \leq 0.25$)*. Chinese Physics B, **20**(8) (2011) 087201.

[25] D Patidar and NS Saxena, *Characterization of single phase copper selenide nanoparticles and their growth mechanism*. Journal of Crystal Growth, **343**(1) (2012) 68-72.

[26] Jun Xu, Weixin Zhang, Zeheng Yang, Shaixia Ding, Chunyan Zeng, Lingling Chen, Qiang Wang and Shihe Yang, *Large - Scale Synthesis of Long Crystalline $Cu_{2-x}Se$ Nanowire Bundles by Water - Evaporation - Induced Self - Assembly and Their Application in Gas Sensing*. Advanced functional materials, **19**(11) (2009) 1759-1766.

- [27] Jun Xu, Weixin Zhang, Zeheng Yang and Shihe Yang, *Lithography inside Cu (OH)₂ nanorods: a general route to controllable synthesis of the arrays of copper chalcogenide nanotubes with double walls*. Inorganic chemistry, **47**(2) (2008) 699-704.
- [28] Yi Xie, Xiuwen Zheng, Xuchuan Jiang, Jun Lu and Liying Zhu, *Sonochemical Synthesis and Mechanistic Study of Copper Selenides Cu_{2-x}Se, β -CuSe, and Cu₃Se₂*. Inorganic chemistry, **41**(2) (2002) 387-392.
- [29] M Azad Malik, Paul O'Brien and Neerish Revaprasadu, *A novel route for the preparation of CuSe and CuInSe₂ nanoparticles*. Advanced Materials, **11**(17) (1999) 1441-1444.
- [30] Xiuwen Zheng and Qitu Hu, *Facile synthesis and phase control of copper chalcogenides with different morphologies*. Applied Physics A: Materials Science & Processing, **94**(4) (2009) 805-812.
- [31] Zhengtao Deng, Masud Mansuripur and Anthony J Muscat, *Synthesis of two-dimensional single-crystal berzelianite nanosheets and nanoplates with near-infrared optical absorption*. Journal of Materials Chemistry, **19**(34) (2009) 6201-6206.
- [32] TP Vinod, Xing Jin and Jinkwon Kim, *Hexagonal nanoplatelets of CuSe synthesized through facile solution phase reaction*. Materials Research Bulletin, **46**(3) (2011) 340-344.
- [33] Yan Zhang, Chenguo Hu, Chunhua Zheng, Yi Xi and Buyong Wan, *Synthesis and Thermoelectric Property of Cu_{2-x}Se Nanowires*. The Journal of Physical Chemistry C, **114**(35) (2010) 14849-14853.
- [34] Wei - Wei Xiong and Qichun Zhang, *Surfactants as Promising Media for the Preparation of Crystalline Inorganic Materials*. Angewandte Chemie International Edition, **54**(40) (2015) 11616-11623.
- [35] Wei-Wei Xiong, Guodong Zhang and Qichun Zhang, *New strategies to prepare crystalline chalcogenides*. Inorganic Chemistry Frontiers, **1**(4) (2014) 292-301.
- [36] Wei-Wei Xiong, Eashwer Umesh Athresh, Yu Ting Ng, Junfeng Ding, Tom Wu and Qichun Zhang, *Growing crystalline chalcogenidoarsenates in surfactants: From*

zero-dimensional cluster to three-dimensional framework. Journal of the American Chemical Society, **135**(4) (2013) 1256-1259.

[37] Wei-Wei Xiong, Pei-Zhou Li, Tian-Hua Zhou, Alfred Ling Yoong Tok, Rong Xu, Yanli Zhao and Qichun Zhang, *Kinetically controlling phase transformations of crystalline mercury selenidostannates through surfactant media*. Inorganic chemistry, **52**(8) (2013) 4148-4150.

[38] Wei-Wei Xiong, Jianwei Miao, Pei-Zhou Li, Yanli Zhao, Bin Liu and Qichun Zhang, *[enH][Cu₂AgSnS₄]: a quaternary layered sulfide based on Cu–Ag–Sn–S composition*. CrystEngComm, **16**(27) (2014) 5989-5992.

[39] Soon Gu Kwon and Taeghwan Hyeon, *Formation mechanisms of uniform nanocrystals via hot-injection and heat-up methods*. Small, **7**(19) (2011) 2685-2702.

[41] Celso de Mello Donegá, Peter Liljeroth and Daniel Vanmaekelbergh, *Physicochemical Evaluation of the Hot-Injection Method, a Synthesis Route for Monodisperse Nanocrystals*. Small, **1**(12) (2005) 1152-1162.

[42] W. Li, R. Zamani, M. Ibanez, D. Cadavid, A. Shavel, J. R. Morante, J. Arbiol and A. Cabot, *Metal ions to control the morphology of semiconductor nanoparticles: copper selenide nanocubes*. Journal of The American Chemical Society, **135**(12) (2013) 4664-7.

[43] Wenhua Li, Reza Zamani, Maria Ibáñez, Doris Cadavid, Alexey Shavel, Joan Ramon Morante, Jordi Arbiol and Andreu Cabot, *Metal ions to control the morphology of semiconductor nanoparticles: copper selenide nanocubes*. Journal of the American Chemical Society, **135**(12) (2013) 4664-4667.

[44] U Schwertmann, RW Fitzpatrick, RM Taylor and DG Lewis, *The influence of aluminum on iron oxides. Part II. Preparation and properties of Alsubstituted hematites*. Clays and Clay Minerals, **27**(2) (1979) 105-112.

[45] Zhengtao Deng, Dong Chen, Bo Peng and Fangqiong Tang, *From bulk metal Bi to two-dimensional well-crystallized BiOX (X=Cl, Br) micro-and nanostructures: synthesis and characterization*. Crystal Growth and Design, **8**(8) (2008) 2995-3003.

- [46] Kyung-Sang Cho, Dmitri V Talapin, Wolfgang Gaschler and Christopher B Murray, *Designing PbSe nanowires and nanorings through oriented attachment of nanoparticles*. Journal of the American Chemical Society, **127**(19) (2005) 7140-7147.
- [47] Constanze Schliehe, Beatriz H Juarez, Marie Pelletier, Sebastian Jander, Denis Greshnykh, Mona Nagel, Andreas Meyer, Stephan Foerster, Andreas Kornowski and Christian Klinke, *Ultrathin PbS sheets by two-dimensional oriented attachment*. Science, **329**(5991) (2010) 550-553.
- [48] G Jeffrey Snyder and Eric S Toberer, *Complex thermoelectric materials*. Nature materials, **7**(2) (2008) 105-114.
- [49] William J Baumgardner, Joshua J Choi, Yee-Fun Lim and Tobias Hanrath, *SnSe nanocrystals: synthesis, structure, optical properties, and surface chemistry*. Journal of the American Chemical Society, **132**(28) (2010) 9519-9521.
- [50] Kegao Liu, Hong Liu, Jiyang Wang and Liming Feng, *Synthesis and characterization of SnSe₂ hexagonal nanoflakes*. Materials Letters, **63**(5) (2009) 512-514.

Chapter V: Monodisperse Cu_3SbSe_4 nanoparticles and related ceramics for thermoelectric applications

5.1 Introduction

During the past few decades, continuous efforts have been devoted to improving the performance of thermoelectric (TE) materials for their applications in cooling and power generation [1-6]. Copper-based multinary semiconductors with zinc blende related crystal structures have recently emerged as ones of the best performing p-type thermoelectric materials [7-11]. One example is the ternary p-type Cu_3SbSe_4 semiconductor. Its unique crystal structures increase the phonon-phonon interactions, resulting in a quite low phonon conductivity [10, 11]. Therefore, the ternary p-type Cu_3SbSe_4 semiconductor has been considered as an important thermoelectric material and has attracted much attention during the past few decades [12, 13].

It is well known that the TE performance is characterized by the dimensionless figure of merit:

$$ZT = S^2 \sigma T / \kappa \quad (5.1)$$

where S is the Seebeck coefficient, σ is the electrical conductivity, κ is the thermal conductivity and T is the absolute temperature, respectively. Therefore, higher electrical conductivity and lower thermal conductivity will significantly improve the performance of thermoelectric materials. This performance is largely dependent on the preparation method which can greatly change their microstructure [14].

To date, almost all the Cu_3SbSe_4 -based materials were fabricated by solid state reactions [9-11, 15-17]. The Cu_3SbSe_4 nanoparticles might be used as the precursor materials for preparing bulk thermoelectric materials. The quality of the precursor nanoparticles, especially the chemical purity and the size distribution, is generally the key for obtaining high quality ceramics. A good thermoelectric material should generate a large quantity of phonon scattering to reduce the lattice thermal conductivity. Li et al. [18] have been the first to report a co-precipitation synthesis of Sn and/or S doped Cu_3SbSe_4 powders with 300-500 nm diameters which were composed by plenty of agglomerated nanospheres having a diameter around 50 nm. However, as far as we know, there have been no reports on synthesis of monodisperse Cu_3SbSe_4 nanoparticles and nor on the TE performance of the Cu_3SbSe_4 -based materials prepared by using monodisperse Cu_3SbSe_4 nanoparticles.

In this chapter, we will develop, for the first time, a facile hot-injection route for large-scale synthesis of the monodisperse Cu_3SbSe_4 and nanoparticles and the Sn doped Cu_3SbSe_4 nanoparticles. It has been proven that the hot-injection approach is an efficient synthetic method not only for binary selenide nanocrystals but also for ternary selenides. The TE properties of the Cu_3SbSe_4 based bulk materials will be studied.

5.2 Experimental procedure

5.2.1 Sample preparation

Using the approach of hot-injection, the Cu_3SbSe_4 based nanoparticles were synthesized by reacting $\text{CuCl}_2 \cdot 2\text{H}_2\text{O}$, SbCl_3 , and $\text{SnCl}_2 \cdot 2\text{H}_2\text{O}$ with an excess of selenium precursor in the presence of hexadecylamine (HDA). In a typical procedure, 1.5 mmol $\text{CuCl}_2 \cdot 2\text{H}_2\text{O}$ (99.99%, aladdin), 0.5 mmol SbCl_3 (99.99%, aladdin) and $\text{SnCl}_2 \cdot 2\text{H}_2\text{O}$ (99.99%, aladdin), 15 mmol HDA (90%, aladdin) and 30 ml octadecene (ODE, 90%, Aldrich) were introduced into a three-neck flask and heated to 200 °C under the protection of argon until all precursors were dissolved and the solution became transparent and light yellow. Afterwards, the solution was cooled to 180 °C and maintained under argon for 0.5 hour to remove oxygen, water and other relatively volatile impurity organic solvents which may exist in commercial solvent. Then 12 ml ODE-Se (0.8 M) solution was injected through a syringe. The excess selenium leads to the instantaneous formation of nuclei of cationic selenide and guarantees the uniformity of grain size by preventing the growth during the grain nucleation. And it can also insure a complete reaction. The mixture was maintained at 180 °C for different time from 0 min up to 60 min and then rapidly cooled down to room temperature in air. Along with the increase of reaction time, the suspension mixtures show a color change from a light orange to an eventually deep green color which qualitatively indicated the formation of Cu_3SbSe_4 nanoparticles. To remove the weakly bound HDA, 9 ml of oleic acid (OA, 90%, Aldrich) was added to the mixture during the cooling step at about 70 °C [19]. And finally the nanoparticles were isolated and purified using chloroform and isopropanol to complete the standard solvent/nonsolvent precipitation/redispersion procedure. To characterize the TE properties of the sintered bulk materials, the Cu_3SbSe_4 based nanoparticles were dried under vacuum at 40 °C for nearly 12 hours and then hot-pressed into dense pellets under a pressure of 80MPa at 350 °C for 1 hour.

Hot pressing is generally a high-pressure process for forming bulk materials, through

solid-solid reaction, by using powders as starting materials. This is achieved by the simultaneous applications of heat and pressure. The schematic representation of a hot pressing apparatus is shown in Fig. 5.1. In this process, heat is produced within the mold when it is subjected to a high frequency electromagnetic field, generated by using an induction coil coupled to a generator. The mold is made of graphite or steel, and the pressure is applied by one or two cylinders onto the punches. The mold is positioned within the induction coil.

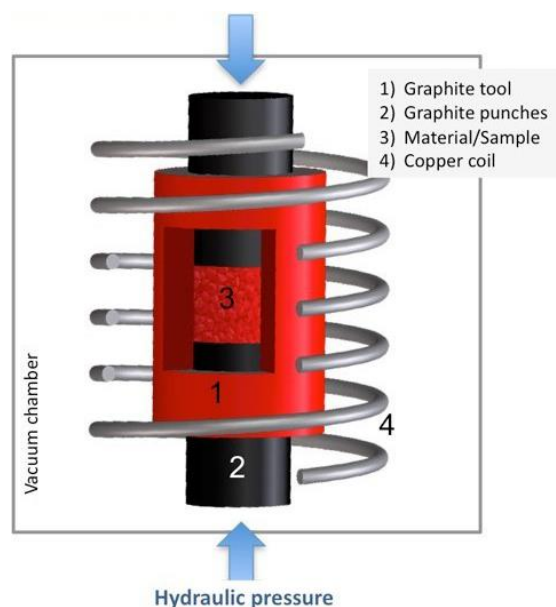


Fig. 5.1 Hot pressing process: schematic of the apparatus

The measured density of Cu_3SbSe_4 , $\text{Cu}_3\text{Sb}_{0.98}\text{Sn}_{0.02}\text{Se}_4$ and $\text{Cu}_3\text{Sb}_{0.94}\text{Sn}_{0.06}\text{Se}_4$ pellets obtained by hot-pressing are 4.84g/cm^3 , 4.92g/cm^3 and 4.47g/cm^3 respectively. The corresponding percentages of densification are 83.4%, 84.8% and 81.7%.

5.2.2 Presentation of characterization techniques

Transmission electron microscopy (TEM) images were obtained from a Philips CM200 field emission transmission electron microscope. High resolution transmission electron microscopy (HRTEM) images and selected area electron diffraction (SAED) patterns were obtained from a FEI Tecnai G2 F20 field emission transmission electron microscope. X-ray diffraction (XRD) analysis was carried out on a PANalytical B.V. Empyrean 200895 X-ray diffractometer. The electrical conductivity and the Seebeck coefficient were measured using a

four-probe method and differential voltage/temperature technique, respectively. The thermal diffusivity and the specific heat capacity were measured on a laser flash apparatus (Netzsch LFA 457). The thermal conductivity κ was calculated from the relationship $\kappa = \rho DC_p$, where D is the thermal diffusivity, C_p the specific heat capacity and ρ the density of the sample estimated by an ordinary dimensional and weight measurement procedure.

5.3 Results and discussion

Fig. 5.2 shows the XRD patterns of the Cu_3SbSe_4 nanoparticles which were synthesized at 180 °C for 0 min, 10 min, 30 min and 60 min. It is clear that the diffraction peaks are in excellent agreement with JCPDS standard card (JCPDS 85-0003) of the tetragonal-phase Cu_3SbSe_4 without a second phase, except for the 0-min powders. These powders are badly crystallized probably with huge distortion of the crystal lattice. It is obvious that the rapid injection which involves the injection of a “cold” (room temperature) solution of precursor molecules into a hot liquid [20] is an effective method for the synthesis of pure phase Cu_3SbSe_4 nanoparticles. The Scherrer formula was used to calculate the mean crystallite size according to the full width at half maximum (FWHM) of the XRD peaks. The size of the Cu_3SbSe_4 nanoparticles synthesized at 180 °C for 10 min is calculated to be about 35 nm.

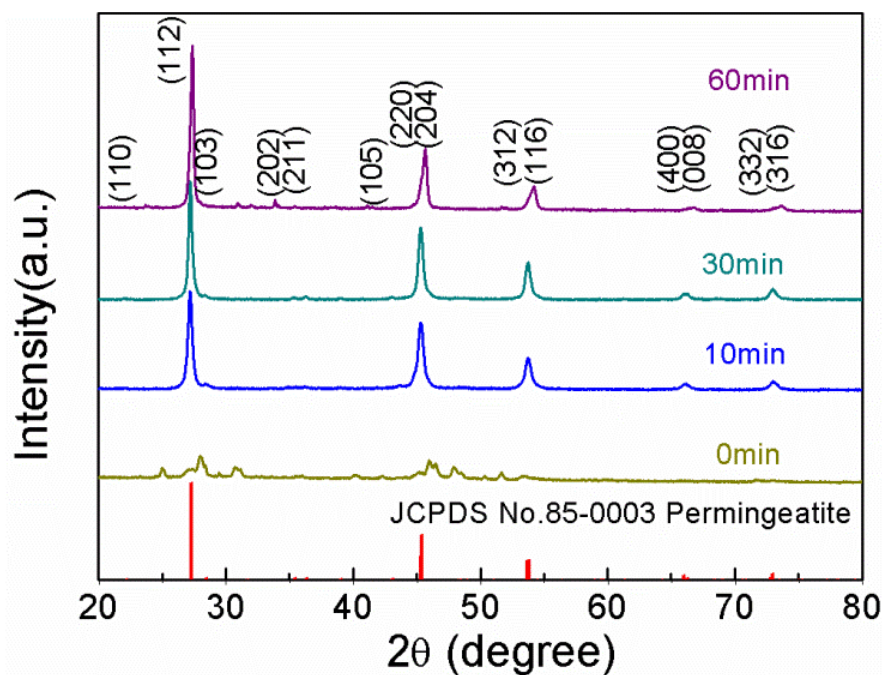


Fig. 5.2 XRD patterns of the Cu_3SbSe_4 nanoparticles which were synthesized at 180 °C for 0 min, 10 min, 30 min and 60 min

Fig. 5.3 shows the XRD patterns of the Cu_3SbSe_4 , $\text{Cu}_3\text{Sb}_{0.98}\text{Sn}_{0.02}\text{Se}_4$ and $\text{Cu}_3\text{Sb}_{0.94}\text{Sn}_{0.06}\text{Se}_4$ nanoparticles which were synthesized at 180 °C for 10 min. Similar XRD patterns can be observed, which indicated that the Sn doping has no significantly influence on the crystalline phase of the Cu_3SbSe_4 nanoparticles.

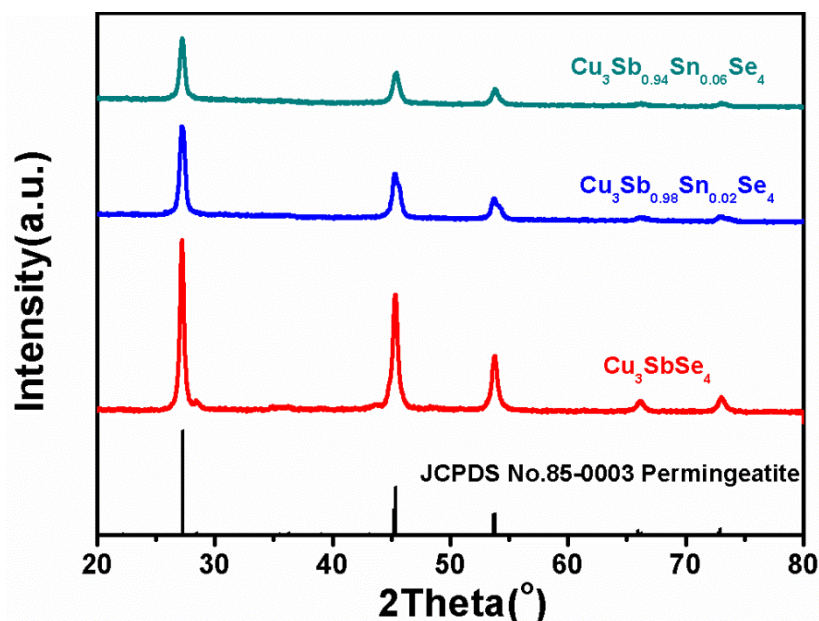


Fig. 5.3 XRD patterns of the Cu_3SbSe_4 , $\text{Cu}_3\text{Sb}_{0.98}\text{Sn}_{0.02}\text{Se}_4$ and $\text{Cu}_3\text{Sb}_{0.94}\text{Sn}_{0.06}\text{Se}_4$ nanoparticles which were synthesized at 180 °C for 10 min

Fig. 5.4 shows the TEM images of the Cu_3SbSe_4 nanoparticles which were synthesized at 180 °C for 0 min, 10 min, 30 min and 60 min. It is clear, according to the TEM image, that the Cu_3SbSe_4 nanoparticles synthesized at 180 °C for 10 min exhibited a quasi-spherical morphology with a narrow size distribution around 35 nm. This observed size is in good agreement with the size calculated with the Scherrer equation. With the increase of reaction time, the average nanoparticle size increases gradually.

Fig. 5.5(a) shows HRTEM image of a randomly selected Cu_3SbSe_4 nanoparticle which were synthesized at 180 °C for 10 min. It confirmed its highly crystallized nature with a tetragonal phase lattice fringes associated with (112) lattice planes (d -spacing of 3.24 Å). Fig. 5.5(b) indicates the SAED pattern of a randomly selected Cu_3SbSe_4 nanoparticle which were synthesized at 180 °C for 60 min. It shows a long regularly ordered diffraction spots which could be indexed to the (112), (105) and (217) planes of the tetragonal structure of the permingeatite whose lattice spacing were 3.24 Å, 2.09 Å and 1.34 Å, respectively.

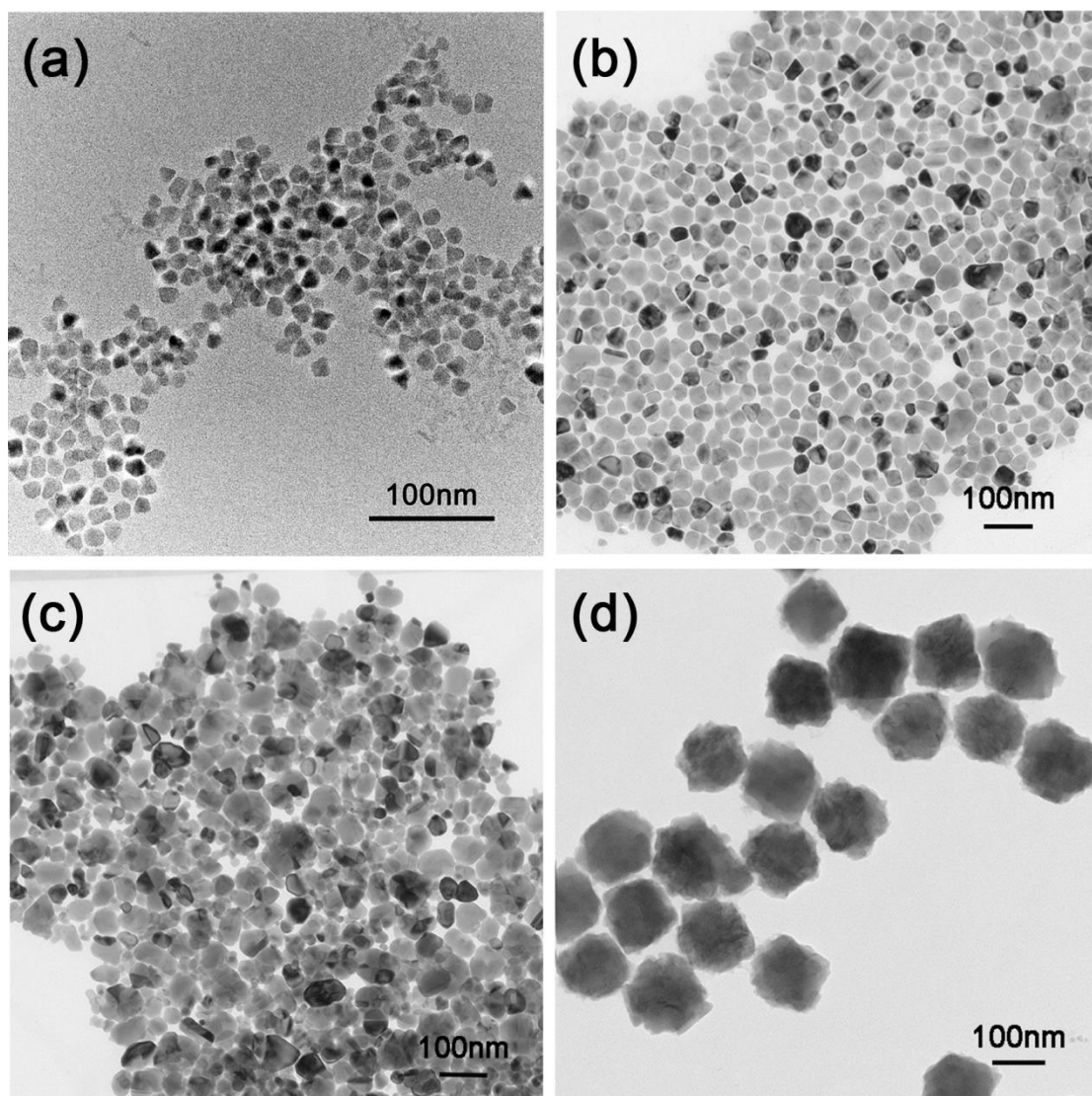


Fig. 5.4 TEM images of the Cu_3SbSe_4 nanoparticles which were synthesized at 180°C for (a) 0 min, (b) 10 min, (c) 30 min, and (d) 60 min

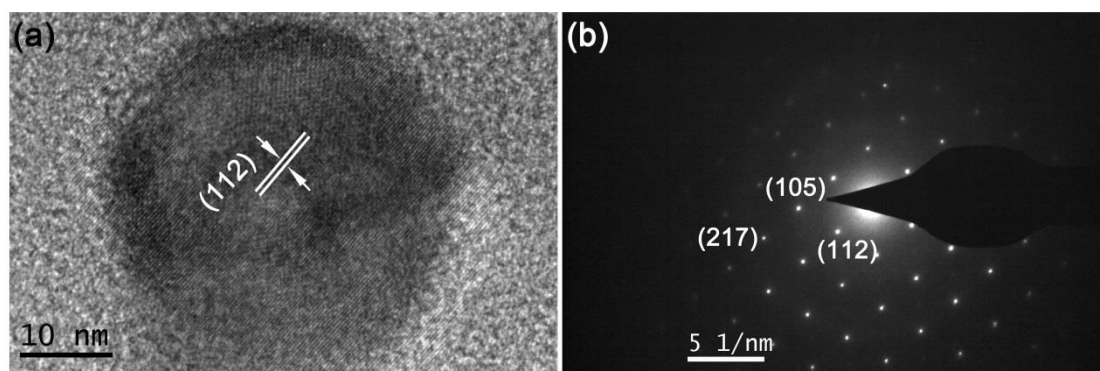


Fig. 5.5 (a) HRTEM image of the Cu_3SbSe_4 nanoparticles which were synthesized at 180 °C for 10 min, and (b) district electron diffraction diagrams of the same Cu_3SbSe_4 nanoparticles

Fig. 5.6 (a) shows the TEM image of the $\text{Cu}_3\text{Sb}_{0.98}\text{Sn}_{0.02}\text{Se}_4$ nanoparticles which were synthesized at 180 °C for 10 min. Similar to the Cu_3SbSe_4 nanoparticles, the $\text{Cu}_3\text{Sb}_{0.98}\text{Sn}_{0.02}\text{Se}_4$ nanoparticles also show a quasi-spherical morphology and a narrow size distribution around 35 nm, which is also consistent with Scherrer-calculated diameter. Therefore, Sn doping has no significant influence on the morphology and the size of the nanoparticles.

Indeed, the nanoparticle synthesis could be resolved into an initial nucleating stage and a subsequent self-growth stage whose cluster growth occurred by monomer deposition, which depletes the metastable phase of monomer and causes stable clusters to grow regardless of their size. In the second stage, an Ostwald ripening process plays a key role in the determination of the ending size. This ripening model is based on the Kelvin equation, which gives the relationship between the ratio of interfacial energy and the thermal energy. Smaller clusters are less stable than larger ones and therefore larger clusters grow at the expense of smaller ones [21].

On this basis, the bulk TE materials were prepared by hot-pressed sintering of the Cu_3SbSe_4 and $\text{Cu}_3\text{Sb}_{0.98}\text{Sn}_{0.02}\text{Se}_4$ nanoparticles which were synthesized at 180 °C for 10 min. They are selected for their narrow size distribution centered at around 35 nm. From the SEM image (Fig. 5.6(b)), it can be found, as expected, that the grain size of the samples hot-pressed at 350 °C for 1 hour shows an obvious growth from nanoscale to microscale. The average grain size is about 1 μm . High surface energy of nanoparticles and extra energy provided by hot pressing are the main driving forces of this grain growth.

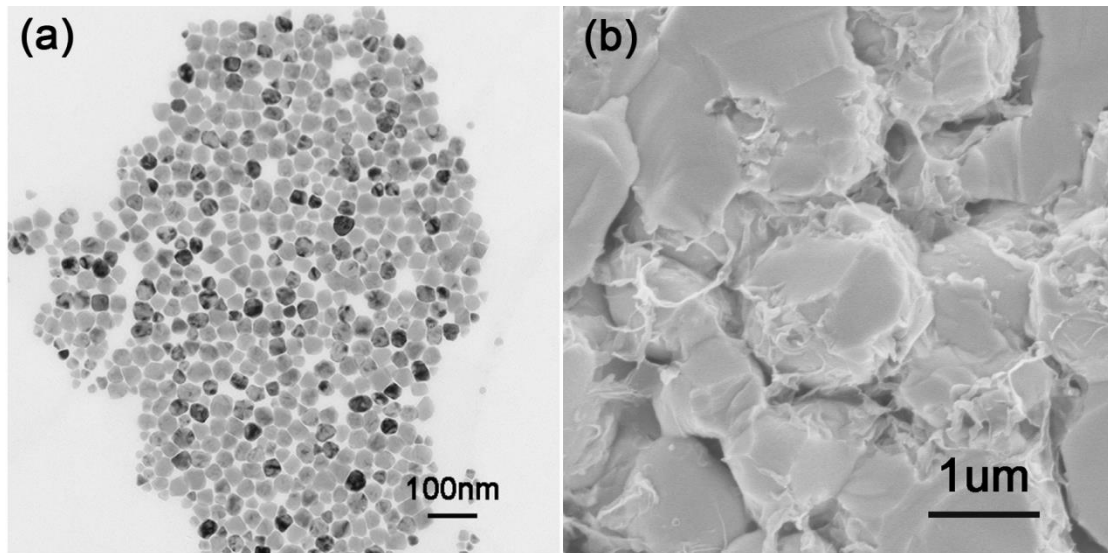


Fig. 5.6 (a) TEM image of the $\text{Cu}_3\text{Sb}_{0.98}\text{Sn}_{0.02}\text{Se}_4$ nanoparticles which were synthesized at 180°C for 10 min. (b) SEM image of bulk material obtained by hot-pressing these nanoparticles at 350°C for 1 hour

Fig. 5.7 shows the dependence of the electrical conductivity (σ) on temperature for the $\text{Cu}_3\text{Sb}_{1-x}\text{Sn}_x\text{Se}_4$ ($x = 0, 0.02$ and 0.06) bulk materials in the temperature range of 300-600 K. By adding Sn, the electrical conductivity (σ) of the $\text{Cu}_3\text{Sb}_{0.98}\text{Sn}_{0.02}\text{Se}_4$ and $\text{Cu}_3\text{Sb}_{0.94}\text{Sn}_{0.06}\text{Se}_4$ bulk materials was greatly increased in comparison with the Cu_3SbSe_4 bulk materials, which is consistent with the previous reports [22, 23]. This could be explained by the introduction of acceptor energy level in the band gap by Sn doping, which give rise to the increase of hole concentration [15]. Indeed, the acceptor centers in the Cu_3SbSe_4 were reported to be associated to the Cu and/or Sb defects [15, 24]. Due to the radius difference between Sn^{4+} (0.69 \AA) and Sb^{5+} (0.61 \AA), the substitution of Sb by Sn would produce lattice distortion and point defects such as vacancies of Cu. This is not observed by the XRD patterns (Fig. 5.3) which show constant lattice parameters, illustrated by the fixed diffraction position. It is then possible that the charge compensation is realized by the formation of Sb^{3+} (0.76 \AA) in the structure. Therefore, it is understandable that the introduction of Sn^{4+} having the average radius of Sb^{5+} and Sb^{3+} could induce macroscopically insignificant distortion of the structure.

Fig. 5.7 shows the electrical conductivity for different materials. The undoped Cu_3SbSe_4 bulk materials have a conductivity increasing slightly with temperature, indicating a

non-degenerate semiconductor-like behavior [15]. In contrast, the temperature dependence of the electrical conductivity for the $\text{Cu}_3\text{Sb}_{0.98}\text{Sn}_{0.02}\text{Se}_4$ and $\text{Cu}_3\text{Sb}_{0.94}\text{Sn}_{0.06}\text{Se}_4$ bulk materials decreased gradually with an increase of temperature, which exhibited metallic-like or degenerate semiconductor behavior [22]. The co-existence of Sb^{5+} and Sb^{3+} could promote the electron mobility inside the materials.

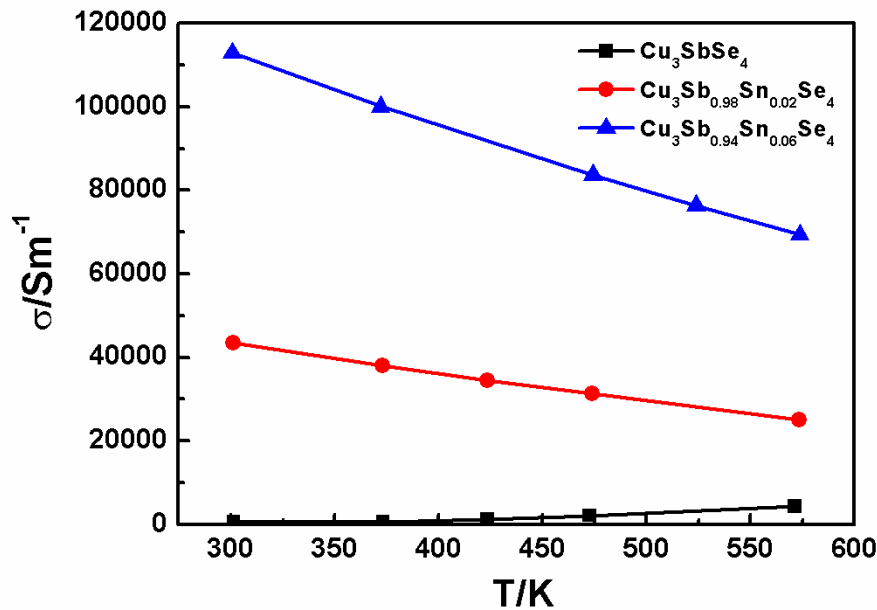


Fig. 5.7 Dependence of electrical conductivity (σ) on temperature for the Cu_3SbSe_4 , $\text{Cu}_3\text{Sb}_{0.98}\text{Sn}_{0.02}\text{Se}_4$ and $\text{Cu}_3\text{Sb}_{0.94}\text{Sn}_{0.06}\text{Se}_4$ bulk materials

Fig. 5.8 shows the dependence of the Seebeck coefficient (S) on temperature for the $\text{Cu}_3\text{Sb}_{1-x}\text{Sn}_x\text{Se}_4$ ($x = 0, 0.02$ and 0.06) bulk materials in the temperature range of 300-600 K. The positive values revealed that they were p-type materials with holes as their main charge carriers. The Seebeck coefficient of the Cu_3SbSe_4 initially decreased with the increase of temperature and then increased with further increase in temperature, leaving a minimum located at around 425 K. For $\text{Cu}_3\text{Sb}_{0.98}\text{Sn}_{0.02}\text{Se}_4$, a similar S variation with the temperature could be also observed, but the fluctuation range is much narrower. However, for the $\text{Cu}_3\text{Sb}_{0.94}\text{Sn}_{0.06}\text{Se}_4$, its Seebeck coefficient shows an approximately linear increase as temperature rises. Moreover, the introduction of Sn resulted in a decrease of the Seebeck

coefficient. Many researches have shown that the Seebeck coefficient and the electrical conductivity were not independent because they have a close relationship with carrier concentration [25-28]. Hence, a compromise between large Seebeck coefficient and electrical conductivity of the TE materials should be chosen to maximize the power factor, which reveals the ability of one thermoelectric material to produce useful electrical power. Fig. 5.9 shows the dependence of the power factor ($PF=S^2\sigma$) on temperature for the Cu_3SbSe_4 , $Cu_3Sb_{0.98}Sn_{0.02}Se_4$ and $Cu_3Sb_{0.94}Sn_{0.06}Se_4$ bulk materials. The $Cu_3Sb_{0.98}Sn_{0.02}Se_4$ reached the highest PF value ($1.31 \times 10^{-3} \text{ Wm}^{-1}\text{K}^{-2}$) at 300 K.

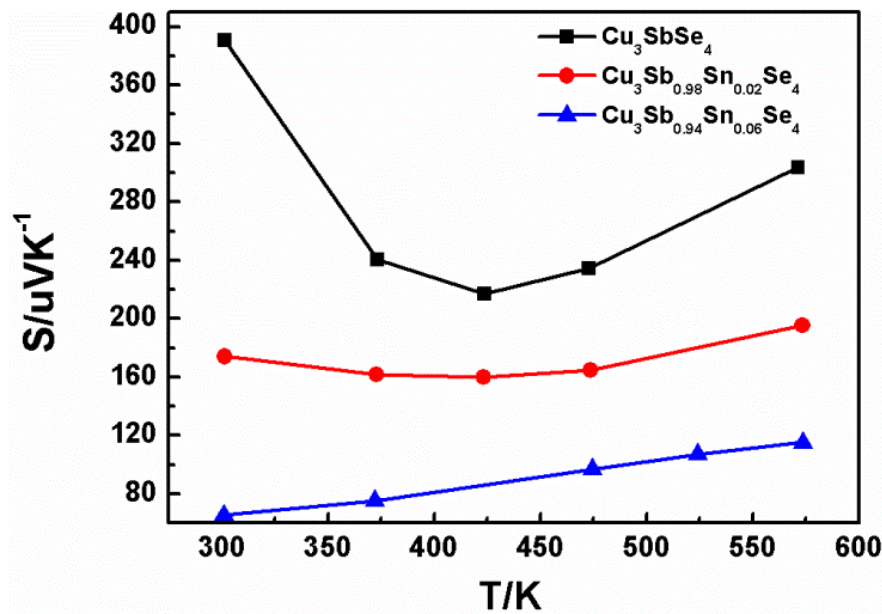


Fig. 5.8 Dependence of the Seebeck coefficient (S) on temperature for the Cu_3SbSe_4 , $Cu_3Sb_{0.98}Sn_{0.02}Se_4$ and $Cu_3Sb_{0.94}Sn_{0.06}Se_4$ bulk materials

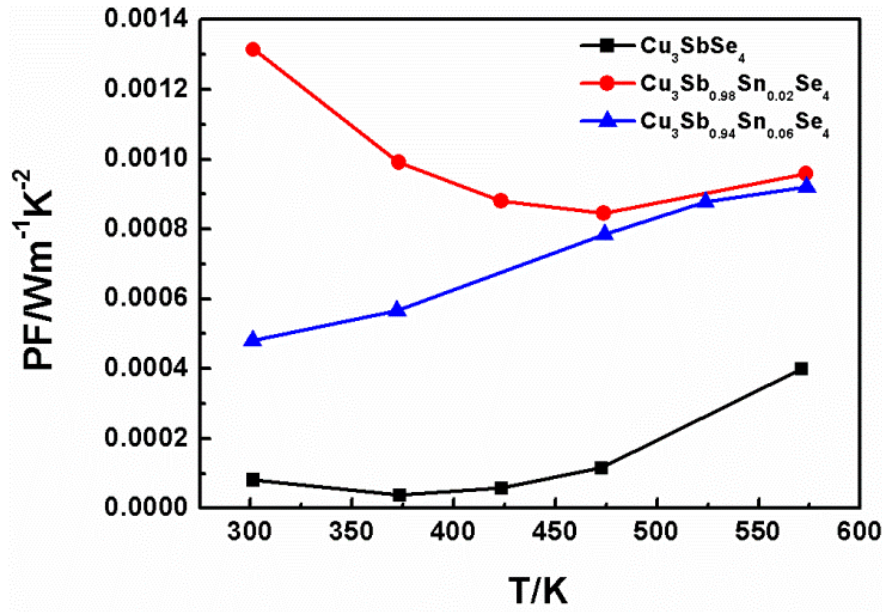


Fig. 5.9 Dependence of the power factor (PF) on temperature for the Cu_3SbSe_4 , $\text{Cu}_3\text{Sb}_{0.98}\text{Sn}_{0.02}\text{Se}_4$ and $\text{Cu}_3\text{Sb}_{0.94}\text{Sn}_{0.06}\text{Se}_4$ bulk materials

To calculate the figure of merit (ZT) of the $\text{Cu}_3\text{Sb}_{1-x}\text{Sn}_x\text{Se}_4$ ($x = 0, 0.02$ and 0.06) bulk materials, the thermal conductivities (κ) were calculated by multiplying thermal diffusivity, specific heat capacity and density. Fig. 5.10 shows the dependence of thermal conductivities (κ) on temperature for the Cu_3SbSe_4 , $\text{Cu}_3\text{Sb}_{0.98}\text{Sn}_{0.02}\text{Se}_4$ and $\text{Cu}_3\text{Sb}_{0.94}\text{Sn}_{0.06}\text{Se}_4$ bulk materials. The thermal conductivities (κ) between 300K and 570K fluctuated in the range of $0.91 \sim 1.15 \text{ Wm}^{-1}\text{K}^{-1}$ for the Cu_3SbSe_4 , $1.10 \sim 1.25 \text{ Wm}^{-1}\text{K}^{-1}$ for the $\text{Cu}_3\text{Sb}_{0.98}\text{Sn}_{0.02}\text{Se}_4$ and $1.40 \sim 1.60 \text{ Wm}^{-1}\text{K}^{-1}$ for $\text{Cu}_3\text{Sb}_{0.94}\text{Sn}_{0.06}\text{Se}_4$ respectively. The lowest κ value, as low as $0.91 \text{ Wm}^{-1}\text{K}^{-1}$, was observed for Cu_3SbSe_4 at 425K. This extremely low thermal conductivity could be attributed to the reduction of the lattice thermal conductivity by increased grain boundary scattering when the Cu_3SbSe_4 bulk materials were prepared by hot-pressing of the Cu_3SbSe_4 nanoparticles.

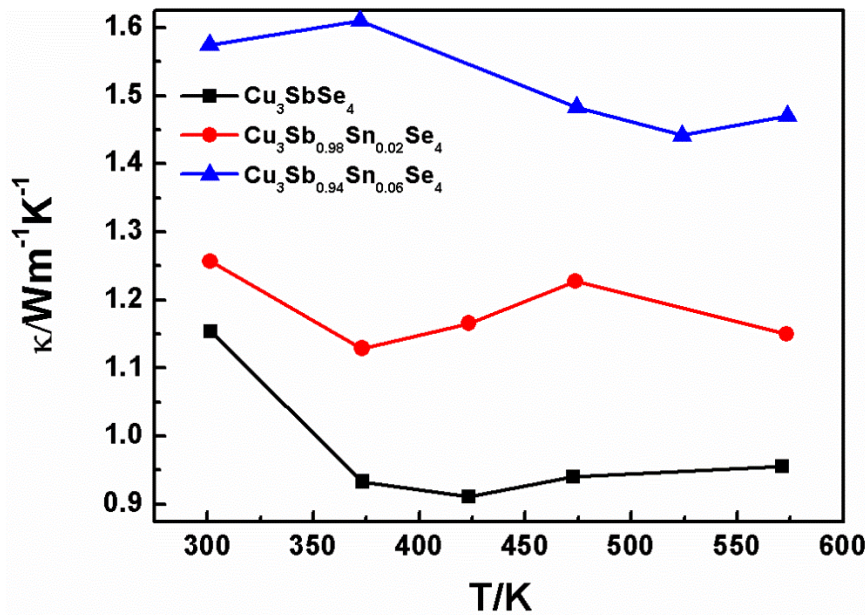


Fig. 5.10 Dependence of thermal conductivity (κ) on temperature for the Cu_3SbSe_4 , $\text{Cu}_3\text{Sb}_{0.98}\text{Sn}_{0.02}\text{Se}_4$ and $\text{Cu}_3\text{Sb}_{0.94}\text{Sn}_{0.06}\text{Se}_4$ bulk materials

Fig. 5.11 shows the dependence of the figure of merit on temperature for the $\text{Cu}_3\text{Sb}_{1-x}\text{Sn}_x\text{Se}_4$ ($x = 0, 0.02$ and 0.06) bulk materials. The ZT values increase basically with increasing temperature. It is obvious that the introduction of Sn improves significantly the ZT values. The maximum ZT value reaches 0.50 at 575 K for the $\text{Cu}_3\text{Sb}_{0.98}\text{Sn}_{0.02}\text{Se}_4$ bulk materials, which is larger than that of the sample prepared by solid state reactions [10]. Evidently, this improvement in the thermoelectric properties is mainly due to its higher power factor and lower thermal conductivity [11, 12]. While with higher Sn doping concentration, the ZT value of $\text{Cu}_3\text{Sb}_{0.94}\text{Sn}_{0.06}\text{Se}_4$ is lower than that of $\text{Cu}_3\text{Sb}_{0.98}\text{Sn}_{0.02}\text{Se}_4$. This is because that electrical conductivity σ and thermal conductivity κ are not independent. Unfortunately, the increase of one leads generally to the increase of the other. Note that further improvement in the sintering technology, such as the substitution of hot pressing by spark plasma sintering, may limit the grain growth and promote densification. This provides the possibility of improving electrical conductivity while decreasing the thermal conductivity simultaneously, which will further enhance the ZT values of the Cu_3SbSe_4 nanoparticles-based TE materials.

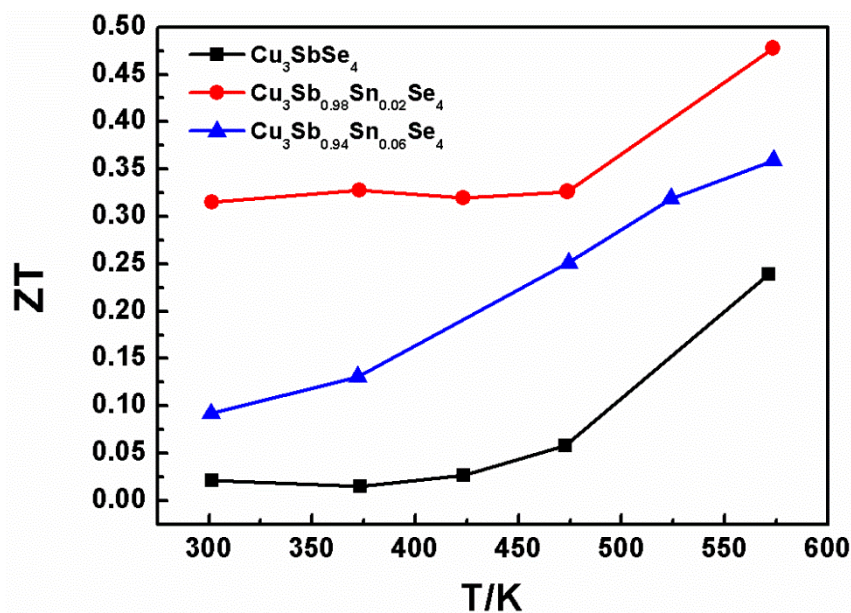


Fig. 5.11 Dependence of the dimensionless figure of merit ZT on temperature for the Cu_3SbSe_4 , $\text{Cu}_3\text{Sb}_{0.98}\text{Sn}_{0.02}\text{Se}_4$ and $\text{Cu}_3\text{Sb}_{0.94}\text{Sn}_{0.06}\text{Se}_4$ bulk materials

Inspired by the work described above, which showed an excellent capacity of the approach of hot-injection for synthesizing binary and ternary selenide nanomaterials, we have also tried to synthesize the Cu_3SbSe_4 and Sb_2Se_3 nanocrystals simultaneously.

1.5 mmol $\text{CuCl}_2 \cdot 2\text{H}_2\text{O}$ (99.99%, aladdin), 2.0 mmol SbCl_3 (99.99%, aladdin), 15 mmol HDA (90%, aladdin) and 30 ml octadecene (ODE, 90%, Aldrich) were introduced into a three-neck flask and heated to 200 °C under the protection of argon until all precursors were dissolved. Afterward, the solution was heated to 240 °C. Then 12 ml ODE-Se (0.8 M) solution was injected through a syringe, providing an sufficient selenium excess. The mixture was maintained at 240 °C for 10 min and then rapidly cooled down to room temperature in air. To remove the weakly bound HDA, 9 ml of oleic acid (OA, 90%, Aldrich) was added to the mixture during the cooling step at about 70 °C. And finally we can get the powder after the centrifuging, washing and drying process.

Fig. 5.12 shows the XRD patterns of the Cu_3SbSe_4 and Sb_2Se_3 nanoparticles which were synthesized at 240 °C for 10 min. It can be seen that the diffraction peaks are in good agreement with the JCPDS standard card (JCPDS 85-0003) of the tetragonal-phase Cu_3SbSe_4 and the card (JCPDS 15-0861) of the orthorhombic-phase Sb_2Se_3 . It confirms that one more

binary selenide, Sb_2Se_3 can also be synthesized by this approach. And the two kinds of selenides crystals can be synthesized simultaneously.

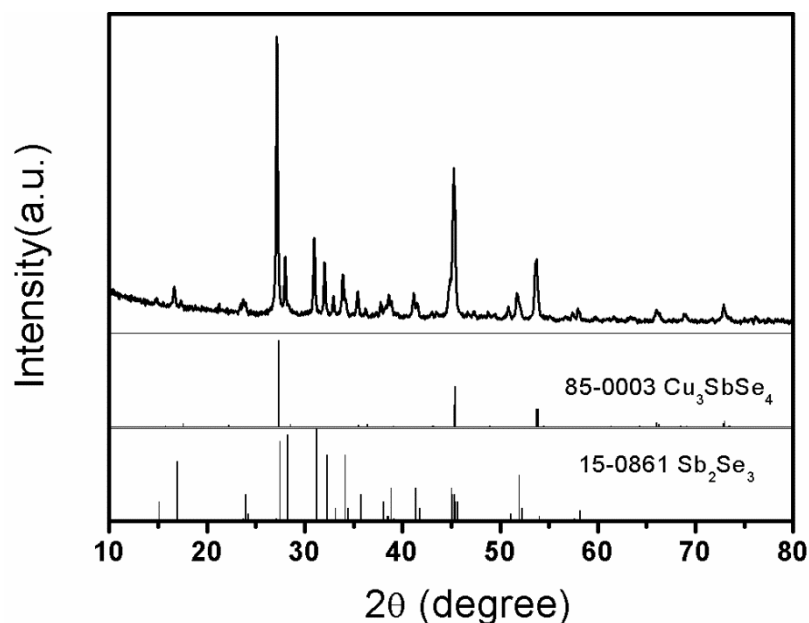


Fig. 5.12 XRD patterns of the Cu_3SbSe_4 and Sb_2Se_3 nanoparticles which were synthesized at 240 °C for 10 min

Fig. 5.13 shows the SEM images of the Cu_3SbSe_4 and Sb_2Se_3 nanocrystals which were synthesized at 240 °C for 10 min. We can see clearly the rod-like Sb_2Se_3 nanocrystal with classical morphology. The average rod length is about 1 μm and the average diameter is about 100nm. The grain size of Cu_3SbSe_4 is uniform which is about 150nm.

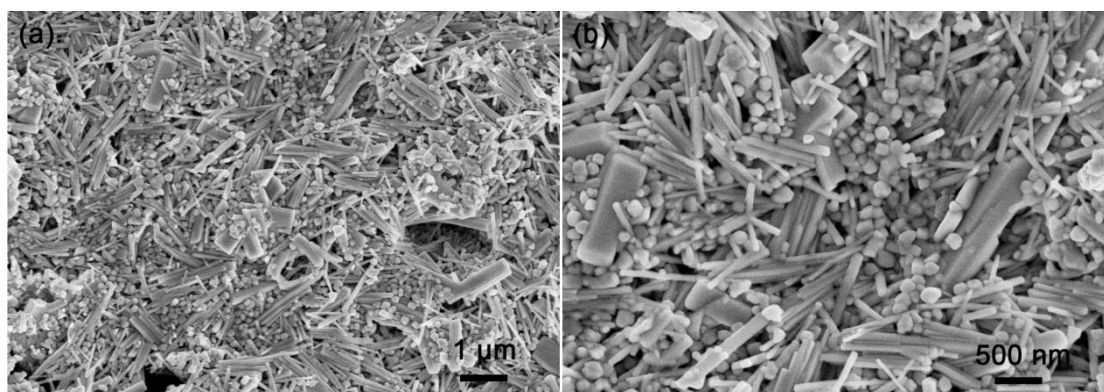


Fig. 5.13 SEM images of the Cu_3SbSe_4 and Sb_2Se_3 nanocrystals which were synthesized at 240 °C for 10 min

5.4 Conclusions

We have demonstrated a rapid-injection route to synthesize the Cu_3SbSe_4 -based nanoparticles which showed a monodisperse and quasi-spherical morphology. The mean nanoparticle size could be adjusted by controlling the reaction time. Those nanoparticles with a smaller size and controlled shape have been used as the starting powders for preparing bulk thermoelectric materials, which resulted in increased grain boundary scattering to reduce the lattice thermal conductivity. The maximum ZT value reached 0.50 at 575 K for the $\text{Cu}_3\text{Sb}_{0.98}\text{Sn}_{0.02}\text{Se}_4$ bulk materials which were prepared by hot-pressing of the precursor nanoparticles. Moreover, the Sb_2Se_3 and Cu_3SbSe_4 nanocrystals with uniform crystal morphology were prepared simultaneously using the hot-injection method.

5.5 References

- [1] Y. Pei, X. Shi, A. LaLonde, H. Wang, L. Chen and G. J. Snyder, *Convergence of electronic bands for high performance bulk thermoelectrics*. Nature, **473**(7345) (2011) 66-9.
- [2] B. Poudel, Q. Hao, Y. Ma, Y. C. Lan, A. Minnich, B. Yu, X. A. Yan, D. Z. Wang, A. Muto, D. Vashaee, X. Y. Chen, J. M. Liu, M. S. Dresselhaus, G. Chen and Z. F. Ren, *High-thermoelectric performance of nanostructured bismuth antimony telluride bulk alloys*. Science, **320**(5876) (2008) 634-638.
- [3] L. D. Hicks and M. S. Dresselhaus, *Thermoelectric figure of merit of a one-dimensional conductor*. Phys Rev B Condens Matter, **47**(24) (1993) 16631-16634.
- [5] S. H. Yang, T. J. Zhu, T. Sun, J. He, S. N. Zhang and X. B. Zhao, *Nanostructures in high-performance $(\text{GeTe})_x(\text{AgSbTe}_2)_{100-x}$ thermoelectric materials*. Nanotechnology, **19**(24) (2008) 245707.

- [6] M. F. O'Dwyer, T. E. Humphrey and H. Linke, *Concept study for a high-efficiency nanowire based thermoelectric*. Nanotechnology, **17**(11) (2006) S338-S343.
- [7] X. Y. Shi, F. Q. Huang, M. L. Liu and L. D. Chen, *Thermoelectric properties of tetrahedrally bonded wide-gap stannite compounds $\text{Cu}_2\text{ZnSn}_{1-x}\text{In}_x\text{Se}_4$* . Applied Physics Letters, **94**(12) (2009) 122103.
- [8] Xiaoya Shi, Lili Xi, Jing Fan, Wenqing Zhang and Lidong Chen, *Cu–Se Bond Network and Thermoelectric Compounds with Complex Diamondlike Structure*. Chemistry of Materials, **22**(22) (2010) 6029-6031.
- [9] E. J. Skoug, J. D. Cain and D. T. Morelli, *High thermoelectric figure of merit in the Cu_3SbSe_4 - Cu_3SbS_4 solid solution*. Applied Physics Letters, **98**(26) (2011)
- [10] E. J. Skoug, J. D. Cain and D. T. Morelli, *Improved Thermoelectric Performance in Cu-Based Ternary Chalcogenides Using S for Se Substitution*. Journal of Electronic Materials, **41**(6) (2012) 1232-1236.
- [11] T. H. Zou, X. Y. Qin, D. Li, L. L. Li, G. L. Sun, Q. Q. Wang, J. Zhang, H. X. Xin, Y. F. Liu and C. J. Song, *Enhanced thermoelectric performance of β - Zn_4Sb_3 based composites incorporated with large proportion of nanophase Cu_3SbSe_4* . Journal of Alloys and Compounds, **588**((2014) 568-572.
- [12] C. Y. Yang, F. Q. Huang, L. M. Wu and K. Xu, *New stannite-like p-type thermoelectric material Cu_3SbSe_4* . Journal of Physics D-Applied Physics, **44**(29) (2011)
- [13] D. Do, V. Ozolins, S. D. Mahanti, M. S. Lee, Y. Zhang and C. Wolverton, *Physics of bandgap formation in Cu-Sb-Se based novel thermoelectrics: the role of Sb valency and Cu d levels*. J Phys Condens Matter, **24**(41) (2012) 415502.
- [14] K. Biswas, J. He, I. D. Blum, C. I. Wu, T. P. Hogan, D. N. Seidman, V. P. Dravid and M. G. Kanatzidis, *High-performance bulk thermoelectrics with all-scale hierarchical architectures*. Nature, **489**(7416) (2012) 414-8.

- [15] X. Y. Li, D. Li, H. X. Xin, J. Zhang, C. J. Song and X. Y. Qin, *Effects of bismuth doping on the thermoelectric properties of Cu_3SbSe_4 at moderate temperatures*. Journal of Alloys and Compounds, **561**((2013) 105-108.
- [16] Min - Ling Liu, I - Wei Chen, Fu - Qiang Huang and Li - Dong Chen, *Improved Thermoelectric Properties of Cu - Doped Quaternary Chalcogenides of $\text{Cu}_2\text{CdSnSe}_4$* . Advanced Materials, **21**(37) (2009) 3808-3812.
- [17] J. Fan, H. L. Liu, X. Y. Shi, S. Q. Bai, X. Shi and L. D. Chen, *Investigation of thermoelectric properties of $\text{Cu}_2\text{Ga}_x\text{Sn}_{1-x}\text{Se}_3$ diamond-like compounds by hot pressing and spark plasma sintering*. Acta Materialia, **61**(11) (2013) 4297-4304.
- [18] Di Li, Rui Li, Xiao-Ying Qin, Jian Zhang, Chun-Jun Song, Ling Wang and Hong-Xing Xin, *Co-precipitation synthesis of Sn and/or S doped nanostructured $\text{Cu}_3\text{Sb}_{1-x}\text{Sn}_x\text{Se}_{4-y}\text{S}_y$ with a high thermoelectric performance*. CrystEngComm, **15**(36) (2013) 7166.
- [19] W. Li, R. Zamani, M. Ibanez, D. Cadavid, A. Shavel, J. R. Morante, J. Arbiol and A. Cabot, *Metal ions to control the morphology of semiconductor nanoparticles: copper selenide nanocubes*. Journal of The American Chemical Society, **135**(12) (2013) 4664-7.
- [20] C. de Mello Donega, P. Liljeroth and D. Vanmaekelbergh, *Physicochemical evaluation of the hot-injection method, a synthesis route for monodisperse nanocrystals*. Small, **1**(12) (2005) 1152-62.
- [21] G. Madras and B. J. McCoy, *Distribution kinetics theory of Ostwald ripening*. Journal of Chemical Physics, **115**(14) (2001) 6699-6706.
- [22] D. Li, R. Li, X. Y. Qin, C. J. Song, H. X. Xin, L. Wang, J. Zhang, G. L. Guo, T. H. Zou, Y. F. Liu and X. G. Zhu, *Co-precipitation synthesis of nanostructured Cu_3SbSe_4 and its Sn-doped sample with high thermoelectric performance*. Dalton Trans, **43**(4) (2014) 1888-96.
- [23] G. S. Nolas, H. Takizawa, T. Endo, H. Sellinshcgg and D. C. Johnson, *Thermoelectric properties of Sn-filled skutterudites*. Applied Physics Letters, **77**(1) (2000) 52.
- [24] Tian-Ran Wei, Heng Wang, Zachary M Gibbs, Chao-Feng Wu, G Jeffrey Snyder and Jing-Feng Li, *Thermoelectric properties of Sn-doped p-type Cu_3SbSe_4 : a compound with large*

effective mass and small band gap. Journal of Materials Chemistry A, **2**(33) (2014) 13527-13533.

[25] Pinwen Zhu, Yoshio Imai, Yukihiro Isoda, Yoshikazi Shinohara, Xiaopeng Jia, Guozhong Ren and Guangtian Zou, *Electrical transport and thermoelectric properties of PbTe prepared by HPHT*. Materials transactions, **45**(11) (2004) 3102-3105.

[26] N Mateeva, H Niculescu, J Schlenoff and LR Testardi, *Correlation of Seebeck coefficient and electric conductivity in polyaniline and polypyrrole*. Journal of Applied Physics, **83**(6) (1998) 3111-3117.

Chapter VI: General conclusions and perspectives

Solar energy has a great potential as a clean, totally renewable and economical energy source. Considering its diffuse and intermittent features, the biggest challenge is to efficiently capture, convert and store this energy. The currently used or considered technologies for harvesting and converting the solar energy include photothermal conversion, photochemical conversion, photovoltaic conversion and thermoelectric conversion which have been described and analyzed in detail in this dissertation. Aiming at this, we have developed different semiconducting ceramics by using selenide based chalcogenides with unique self-organized microstructure with strong solar light absorption as well as efficient charge generation and transport.

This work has been inspired by the recent results obtained in our laboratory with the $\text{GeSe}_2\text{-Sb}_2\text{Se}_3\text{-CuI}$ glass ceramics which have been studied initially for infrared transmission. The controlled crystallization of the precursor glass led to a semiconducting ceramic with self-organized heterojunction structure which greatly facilitates the separation photo generated charge carriers. These heterojunctions were formed by the p-type semiconductor Cu_2GeSe_3 and the n-type Sb_2Se_3 . In this study, we present an original technique for preparing ceramics directly with these two active phases, Sb_2Se_3 and Cu_2GeSe_3 , having relatively narrow bandgap. The objective is to avoid the inactive amorphous phase or other useless phases.

Using the melt-quenching approach with sealed silica tube, process used for the high purity chalcogenide glass, we demonstrated the feasibility of a novel series of semiconducting ceramic with $x\text{Cu}_2\text{GeSe}_3\text{-(1-x)Sb}_2\text{Se}_3$ heterojunction microstructure. Results of PEC measurement under a chopped light source (400 W.m^{-2}) showed a photocurrent of about $50 \mu\text{A/cm}^2$ at the bias equal to $(-0.6) \text{ V}$ which is much higher than pure phase samples. Studies of the microstructure and other properties of the $\text{Cu}_2\text{GeSe}_3\text{-Sb}_2\text{Se}_3$ ceramic revealed the importance of the micro arrangement on the the mechanism of charge photo-generation, separation and migration. The Cu_2GeSe_3 nanocrystals grew on the surface of Sb_2Se_3 rods, leading to the formation of p-n junctions. At the same time, the relatively conductive Cu_2GeSe_3 nanocrystals connected to each other along the Sb_2Se_3 rod orientation, thereby forming a conductive microdomain. The interconnected conductive microdomains eventually provided macroscopic conductive channels for the ceramic. Consequently, the photo-generated charge carriers firstly can be efficiently separated by the p-n junctions, and

then transported through the conductive channels in the ceramic. Similar structure in glass ceramics has allowed to obtain exceptionally long lifetime of charge carriers.

The influence of iodine addition on the microstructure and photoelectrical properties of the $\text{Cu}_2\text{GeSe}_3\text{-Sb}_2\text{Se}_3$ ceramics has been investigated. It has been demonstrated that the iodine addition (by substituting totally or partially Cu with CuI as starting material) leads to the broken of the conductive Cu_2GeSe_3 channels and the generation of a new crystalline phase n-type SbSeI with significantly higher conductivity than Sb_2Se_3 . The photogenerated charge transport paths go through the n-type SbSeI and the p-type Cu_2GeSe_3 . The photo-electro-chemical measurements show simultaneously n-type and p-type semiconductor behaviors with the iodine doped ceramics. More detailed study is still needed to better understand the exact structure-property relationship the charge photo-generation mechanism as well as the electronic properties such as the life time of the minority charge carrier and their diffusion length etc.

The cost/performance ratio is one of the crucial parameters which determine the application potential of almost any product. This is of course also the case for semiconducting materials. The above-studied system is directly inspired by the similar glass-forming system where germanium selenide is essential for glass forming, even the germanium content can be very low, less than 10%. We have studied the possibility to eliminate totally germanium by using Cu_3SbSe_4 instead of Cu_2GeSe_3 . Both of them have similar structure and the former has even higher electrical conductivity. The $\text{Cu}_3\text{SbSe}_4\text{-Sb}_2\text{Se}_3$ system has been studied with or without addition of iodine.

Results of PEC measurements under a chopped light source showed a photocurrent of ($50\mu\text{A}/\text{cm}^2$) at the bias equal to (-0.6) V which is on the same level of $\text{Cu}_2\text{GeSe}_3\text{-Sb}_2\text{Se}_3$ ceramics. The iodine addition also played a similar role. To the best of our knowledge, $\text{Cu}_3\text{SbSe}_4\text{-Sb}_2\text{Se}_3$ ceramics have not been reported before and they offer the possibility of developing a family of efficient photoelectric materials with low-cost and abundant raw materials.

Other selenide based photoelectric materials have also been studied. One of them is copper chalcogenides which have been considered as an important photovoltaic material. However, the reports mentioned and widely used methods are either toxic or complicated,

time-consuming or energy inefficient. In this work, we have demonstrated a new hot-injection approach to prepare CuSe nanoplates with high quality single-crystals and two dimensional nanostructure. This technique excludes the use of toxic or expensive materials, increasing the availability of two-dimensional binary chalcogenide semiconductors. The structure of the nanocrystals has been studied and the possible mechanism of the nanoplates formation has been proposed. The optical characterisation shows that the nanoplates demonstrate wide and tuneable absorption band in the visible and near infrared region. These nanoplates could be interesting for converting solar energy and for nanophotonic devices operating in the near infrared.

Considering the overall electric and electronic properties of Cu_3SbSe_4 , we have also studied the possibility to use it or its derivatives for thermos-electric applications. A new route for synthesizing nanoparticles with a narrow size distribution has been developed based on the rapid-injection technique. Those nanoparticles showed a monodisperse and quasi-spherical morphology. This type of precursor powders is essential for achieving a high densification by hot pressing. The tin-doped compounds, the $\text{Cu}_3\text{Sb}_{1-x}\text{Sn}_x\text{Se}_4$ ($x = 0, 0.02$ and 0.06) nanoparticles-based bulk materials have been specially studied and prepared by hot-pressing the nanoparticles. Their thermoelectric performances were systematically studied in relationship with the composition and the structure. Due to the reduced lattice thermal conductivity from enhanced phonon scattering at the grain interfaces of the bulk materials, the maximum ZT value of the $\text{Cu}_3\text{Sb}_{0.98}\text{Sn}_{0.02}\text{Se}_4$ bulk materials reached 0.50 at 575 K.

This work has been focused on selenide or mix-selenide compounds for energy conversion. Inorganic composite semiconducting ceramics with inter heterojunctions have been developed with interesting features. This pioneer work could be interesting and helpful for developing a totally new species of materials with highly efficient photoelectrical and photocatalytic activities. The final objective is of course to contribute to the design of totally new materials for converting efficiently the solar energy into electrical or chemical energy. We believe that this work is only the beginning of an important research topic. Future studies could be carried out in the following directions:

Firstly, new material systems with better matched n-type and p-type semiconducting phases can be developed to better harvest the solar energy. The two innovative features provided by this unique structure, with interne self-organized heterojunctions, are conductive channels

and randomly distributed absorbers along the conductive channels. The fabrication of conductive channels opens the possibility of using materials with high electrical conductivity in association with compounds having much lower electric conductivity, but strong absorption of the solar spectrum, which is for example the case of Sb_2Se_3 . Moreover, a multiple-heterojunction system, which may contain several semiconductors having complementary bandgap for better covering the entire solar spectrum, could also be fabricated along a conductive channel to increase the conversion efficiency of the whole solar spectrum.

Secondly, after necessary characterization of these semiconducting ceramics, especially in terms of electronic structure as well as optical properties, a photovoltaic device can be designed and fabricated. The main function of the device is to efficiently extract the charge carriers abundantly generated and separated by the internal heterojunctions inside the ceramics. These abundant charge carriers can also be very useful for photocatalytic application. This is already demonstrated in the previous work on similar glass ceramics. The application is also worth of future study with these innovative ceramics.

The new route for synthesizing monodisperse nanoparticles is very interesting for preparing precursor powders which can be easily sintered into dense ceramics. This may lead to new ceramics with greatly improved figure of merit for thermo-electric applications.

In summary, these new materials or new fabrication routes are interesting for energy conversion. The next step is to fabricate a device and to measure its energy conversion efficiency in order to fully demonstrate their application potential. There is of course still a long way to go.

Abstract

This work was focused on selenide semiconducting compounds for energy conversion by photovoltaic or thermoelectric effect.

A totally new family of $\text{Cu}_2\text{GeSe}_3\text{-Sb}_2\text{Se}_3$ ceramics with a unique microstructure was fabricated directly by melt-quenching method. The influence of the material composition and the iodine addition on the microstructure and photoelectrical properties was investigated. The interpenetrating heterojunction network formed by two relatively narrow bandgap semiconductors has an obvious enhancement effect on the photoelectrical properties. The $\text{Cu}_3\text{SbSe}_4\text{-Sb}_2\text{Se}_3$ system has also been studied with the objective to eliminate the germanium which is a relatively rare element. And the results indicated that Cu_3SbSe_4 can substitute the Cu_2GeSe_3 to form heterojunctions with Sb_2Se_3 , maintaining the efficient charge separation and transport.

A hot-injection based-approach has been used for the synthesis of selenide semiconducting materials for photovoltaic or thermoelectric applications. CuSe nanoparticles and CuSe nanoplates with high quality single-crystals and two dimensional nanostructure were prepared. The structure of the nanocrystals has been studied and the mechanism of the nanoplates formation has been proposed. $\text{Cu}_3\text{Sb}_{1-x}\text{Sn}_x\text{Se}_4$ nanoparticles with a narrow size distribution had also been synthesized through the hot-injection route. They have been used as precursors for the preparation of bulk materials by hot-pressing and their thermoelectric performances have been studied.

RESUME

Ce travail porte sur les composés semi-conducteurs à base de séléniures pour la conversion d'énergie par effet photovoltaïque ou thermoélectrique.

Une nouvelle famille de céramiques $\text{Cu}_2\text{GeSe}_3\text{-Sb}_2\text{Se}_3$ avec une microstructure unique a été synthétisée par un procédé de fusion-trempe. L'influence de la composition du matériau et de l'ajout de l'iode sur la microstructure et les propriétés photoélectriques a été étudiée. Le réseau d'hétérojonctions formé par deux semi-conducteurs à bande interdite relativement étroite a un effet évident sur les propriétés photoélectriques. Le système $\text{Cu}_3\text{SbSe}_4\text{-Sb}_2\text{Se}_3$ a également été étudié avec l'objectif d'éliminer le germanium qui est un élément relativement rare. Et les résultats indiquent que le Cu_3SbSe_4 peut remplacer le Cu_2GeSe_3 pour former des hétérojonctions avec Sb_2Se_3 , en maintenant une séparation et un transport de charges efficaces.

Une approche basée sur une injection à chaud a été utilisée pour la synthèse de matériaux semi-conducteurs à base de séléniures pour des applications photovoltaïque ou thermoélectrique. Des nanoparticules et nano-feuillets monocristallins bidimensionnels de CuSe de haute qualité ont été obtenus. La structure des nanocristaux de $\text{Cu}_3\text{Sb}_{1-x}\text{Sn}_x\text{Se}_4$ a été étudiée et le mécanisme de formation des nano-feuillets a été proposé. Des nanoparticules de $\text{Cu}_3\text{Sb}_{1-x}\text{Sn}_x\text{Se}_4$ avec une distribution de taille étroite ont été également synthétisées avec le procédé d'injection à chaud. Ces nanoparticules ont été utilisées comme précurseurs pour la préparation de matériaux massifs par pressage à chaud. Leur performance thermoélectrique a été étudiée.

VU:

Le Directeur de Thèse
(nom et prénom)

VU:

Le Responsable de l'École Doctorale

VU pour autorisation de soutenance
Rennes, le

Le Président de l'Université de Rennes 1

David ALIS

VU après soutenance pour autorisation de publication

Le Président de Jury,
(nom et prénom)